Development of Radiation Hard Pixel Sensors for the CMS Experiment

Dissertation

zur

Erlangung der naturwissenschaftlichen Doktorwürde
(Dr. sc. nat.)

vorgelegt der

Mathematisch-naturwissenschaftlichen Fakultät

der

Universität Zürich

von

Rolf Kaufmann

von

Knutwil LU

Begutachtet von

Prof. Dr. Claude Amsler
Dr. Roland Horisberger

Zürich 2001

Die vorliegende Arbeit wurde von der Mathematisch-naturwissenschaftlichen Fakultät der Universität Zürich auf Antrag von Prof. Dr. C. Amsler und Prof. Dr. U. Straumann als Dissertation angenommen.

SUMMARY

The most interesting events in the CMS experiment are likely to contain several b jets. These jets will be used to identify physics channels containing top quarks or the Higgs boson. Due to the long lifetime of the B mesons, b jets can be recognised (tagged) by the presence of displaced secondary vertices. In order to allow an efficient tagging of these b jets, trajectories of the reaction products have to be measured with high precision. Therefore it is desirable that the tracking extends as closely as possible towards the interaction point.

The large background of light quark jets and spiralling low momentum particles requires the innermost tracking layers of CMS to be composed of high precision pixel devices to avoid ambiguities in the track reconstruction.

This background also causes a very high radiation dose rate that the pixel detectors have to withstand. The integrated dose will be so high ($\sim 10^5$ Gy) that silicon, the sensor and chip material, changes its characteristics during the detectors lifetime. Therefore, the chip- and sensor-designs are not only constrained by the physics requirements, but also by the difficult operating conditions.

The radiation damages induce changes in the silicon resistivity, leading to a type inversion: An originally n-type sensor is more and more converted into p-type by the introduction of acceptor-like states into the band-gap, and by the removal of the original donor states from it. Towards the end of the pixel sensors lifetime in CMS, the radiation induced acceptor concentration will exceed the original donor doping by at least a factor of two.

This work describes the development of a pixel sensor which can cope with the harsh operation environment. This means to optimise the signal to noise ratio and to guarantee a reliable operation without breakdown, both in the unirradiated state and after high doses. Therefore several highly interrelated properties like pixel isolation, pixel capacitance, high voltage stability or charge sharing had to be understood in detail.

. | .

In particular, the following problems were worked out:

- Pixels with a bad or missing connection to the read-out chip are expected to charge up. They may reach a potential so high that breakdown phenomena could occur. In order to avoid such breakdowns, a new pixel isolation technique with open, atoll-like p-stop rings was developed and successfully tested. Before irradiation these open p-stops showed an inter-pixel resistance of a few $\mathrm{M}\Omega$ at full depletion, which is in agreement with the requirements. During the high dose irradiation this resistance was measured to rise up to several $\mathrm{G}\Omega$. Nevertheless, no breakdowns due to unconnected pixels were observed in beam- nor in laboratory-tests.

- The radiation induced acceptor increase requires a high bias voltage to preserve a sufficient depletion depth, which can lead to high electric fields. To protect the sensor from breakdown the potential gradients have to be kept small. For this purpose several multi guard ring structures were designed and tested. One of them even holds up to 1 kV after irradiation.

- The capacitance of a pixel to its neighbourhood is an important parameter for the noise performance of the detector. In this work the pixel capacitance of n-type pixels was reliably measured for the first time. For a design as it was proposed in the CMS Tracker Technical Design Report, its value was determined to be $(25.7 \pm 1.8)\,\mathrm{fF}$. In addition the design dependence of the pixel capacitance could also be modelled.

- Due to the high magnetic field of 4 T in the CMS experiment, the electrons created along a particles trajectory in the sensor are distributed among several pixels (Lorentz-effect). This charge sharing was investigated as a function of the depth, where the charge was created. It turned out that low electric field zones in the sensor strongly influence the charge sharing pattern.

ZUSAMMENFASSUNG

Viele der interessantesten Ereignisse im CMS Experiment werden b Jets enthalten. Diese Jets sind nützlich zur Identifizierung von Top Quarks oder dem Higgs Boson. Durch die verhältnismässig lange Lebensdauer der B Mesonen können solche b Jets an örtlich versetzten Sekundärvertices erkannt werden. Um diese Sekundärvertices zu rekonstruieren, muss man die Spuren der Reaktionsprodukte genau vermessen, was um so besser möglich ist, je näher sich die Detektoren beim Vertex befinden.

Wegen dem hohen Untergrund von leichten Quark Jets und langsamen, spiralisierenden Teilchen müssen die innersten Spur-Detektoren in CMS aus kleinen, präzisen Silizium Pixelzellen gebaut werden, um Mehrdeutigkeiten in der Spur-Rekonstruktion möglichst zu vermeiden.

Dieser Untergrund ist ebenfalls für die hohe radioaktive Dosisrate verantwortlich, der der Pixel-Detektor standhalten muss. Die integrierte Dosis wird so hoch sein (10^5 Gy), dass Silizium, das Chip- und Sensormaterial, im Verlauf der Detektor-Lebensdauer seine Eigenschaften ändert. Somit ist das Chip- und Sensor-Design nicht nur durch die teilchenphysikalischen Anforderungen eingeschränkt, sondern auch durch die schwierigen Betriebsbedingungen.

Die Strahlenschäden verursachen Veränderungen der Silizium-Resistivität, welche bis zur Typ-Umkehrung führen: Ein ursprünglicher n-typ Sensor wird durch das Einfügen von akzeptor-artigen Energieniveaus und durch das Entfernen der ursprünglichen Donor-Niveaus immer mehr in einem p-typ Sensor umgewandelt. Gegen Ende seiner Lebensdauer wird die strahleninduzierte p-Dotierung im CMS Pixel Sensor die ursprüngliche n-Dotierung um mindestens einen Faktor zwei übertreffen.

Diese Arbeit beschreibt die Entwicklung eines Pixel Sensors, der unter solch schwierigen Betriebsbedingungen noch funktionsfähig bleibt. Das heisst unter anderem das Signal zu Rauschen Verhältnis zu optimieren und einen störungsfreien Betrieb zu garantieren, beides im unbestrahlten Zustand und nach hohen Dosen. Mehrere stark verknüpfte Eigenschaften wie Pixel Isolation, Pixel Kapazität, Hochspannungsstabilität oder Ladungsteilung müssen dazu im Detail verstanden werden.

. | .

Insbesondere wurden folgenden Probleme angegangen und gelöst:

- Pixel mit einer schlechten oder ganz fehlenden Verbindung zum Auslesechip können sich aufladen. Eventuell erreichen sie ein so hohes Potential, dass sie sich stochastisch zu entladen beginnen. Um solche Durchbrüche zu verhindern, wurde eine neue Pixel-Isolations Technik mit offenen, Atoll-ähnlichen p-Stop Ringen entwickelt und erfolgreich getestet. Vor Bestrahlung ergab sich mit diesem Design ein Pixel-zu-Pixel Widerstand von einigen MΩ, was den Anforderungen entspricht. Während der Bestrahlung mit hohen Dosen stieg dieser Widerstand jedoch auf mehrere GΩ. Trotzdem wurden aber keine Durchbrüche bei fehlenden Verbindungen zum Auslesechip beobachtet, weder in Strahl- noch in Labortests.

- Die strahleninduzierte Akzeptorzunahme führt zu einer höheren Betriebsspannung, um eine genügend tiefe Verarmungszone aufrecht zu erhalten. Damit verbunden sind hohe elektrische Feldstärken. Um den Sensor vor Durchbrüchen zu schützen, müssen die Potentialgradienten möglichst klein gehalten werden. Zu diesem Zweck wurden im Rahmen dieser Arbeit mehrere Schutzring-Designs entworfen und erfolgreich getestet. Eines hielt nach Bestrahlung einer Spannung bis zu 1 kV stand.

- Die Kapazität eines Pixels zu seiner Umgebung ist ein wichtiger Parameter für das Rausch-Verhalten eines Detektors. In dieser Arbeit wurde die Kapazität von n-typ Pixelzellen zum ersten Mal gemessen. Für das im “CMS Tracker Technical Design Report” vorgeschlagene Pixel Design beträgt die totale Pixel-Kapazität (25.7 ± 1.8) fF. Zusätzlich konnte die Abhängigkeit der Kapazität von wichtigen Design Parametern etabliert werden.

- Die entlang der Flugbahn eines Teilchens im Sensor erzeugten Elektronen und Löcher werden durch das hohe Magnetfeld von 4 T auf mehrere Pixel verteilt (“Lorentz-Effekt”). Diese Ladungsteilung wurde als Funktion der Erzeugungstiefe der Signalladung untersucht. Es stellte sich heraus, dass Zonen kleiner Feldstärke im Sensor das Ladungsverhalten sehr stark beeinflussen.

CONTENTS

CHAPTER

ONE

LHC AND CMS

1.1 The LHC Accelerator

Figure 1.1: *The site of the LHC-ring near Geneva, in the background one can see the lake of Geneva and the French alps.*

In 2006 the new Large Hadron Collider (LHC) will become operational in the existing 27 km long LEP tunnel at CERN, the European particle physics laboratory in Geneva. The LEP-accelerator, which was shut down in December 2000, is currently being dismantled. The new LHC collider will allow proton-proton collisions at a centre of mass energy of 14 TeV and a luminosity of $\mathcal{L} = 10^{34}\,\mathrm{cm}^{-2}\ \mathrm{s}^{-2}$. This new accelerator will extend the centre of mass energy attained by Tevatron (the $\overline{p}p$-collider at Fermilab, Chicago, USA) by a factor of ten and the luminosity by two orders of magnitude.

Figure 1.1 gives an overview of the tunnel-site, in which the LHC collider is going to be installed. It will consist of two "colliding" synchrotrons. They will be filled with protons delivered from the SPS and its pre-accelerators at 0.45 TeV. In two superconducting magnetic channels the protons are accelerated to 7 TeV (see figure 1.2). These protons then counter-rotate for several hours and collide at the experiments, until the beams become so degraded that the machine has to emptied and refilled. The magnetic channels will be housed in the same yoke and cryostat, a unique configuration that not only saves space but also gives a 25 % cost saving over separate rings. To bend 7 TeV protons around the ring, the superconductive LHC dipoles must be able to produce fields of 8.3 Tesla. Some other parameters of LHC are summarised in table 1.1.

Table 1.1: *LHC general parameters*

Beam energy at collision	7	TeV
Beam energy at injection	450	GeV
Dipole field at 7 TeV	8.33	T
Design luminosity	1	$10^{34}\,\mathrm{cm}^{-2}\mathrm{s}^{-1}$
DC beam current	0.56	A
Bunch spacing	7.48	m
Bunch separation	24.95	ns
Number of particles per bunch	1.1	10^{11}
Total crossing angle	300	μrad
Luminosity lifetime	10	h
Energy loss per turn	7	keV
Total radiated power per beam	3.8	kW
Stored energy per beam	350	MJ
Filling time per ring	4.3	min

The main motivation for building such a machine is to investigate the mechanism responsible for electroweak symmetry breaking. In the standard model particles are only allowed to have mass if this symmetry is broken by an additional field, the so called Higgs field [1]. Its discovery is an important and long searched brick in the building of the standard model. Associated with the Higgs mechanism are massive scalar particles, called Higgs bosons, and the proof for this mechanism would come from the observation of this

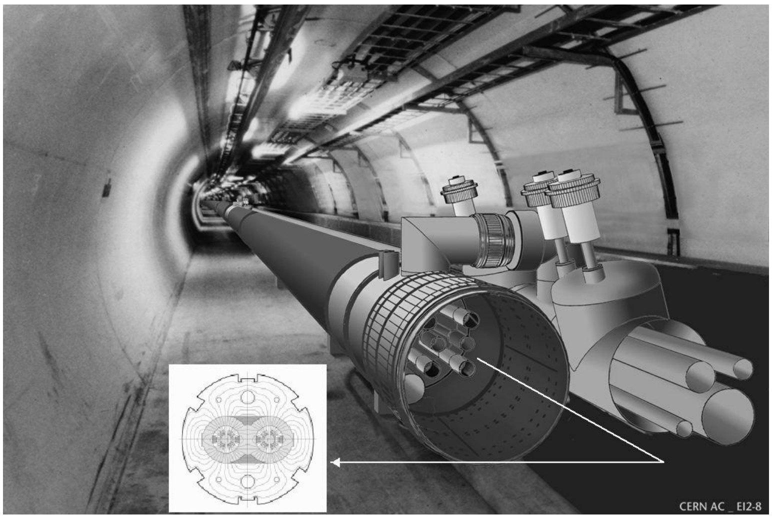

Figure 1.2: *Schematic drawing of the LHC vacuum tubes in the existing LEP tunnel.*

novel species. In its minimal version the standard model requires one Higgs field, corresponding to one neutral, scalar Higgs boson.

The present experimental mass constraints on the standard model Higgs boson are loose. Radiative corrections to weak processes lead to an upper bound of $m_H \leq 215\,\mathrm{GeV}/c^2$ with 95% confidence level [2]. In its second phase LEP reached a maximal energy of 209.2 GeV. With 95% confidence level a Higgs with a mass lower than $113.5\,\mathrm{GeV}/c^2$ was excluded. But during the last months of operation the LEP experiments reported a number of collisions compatible with the production of Higgs bosons with a mass around $115\,\mathrm{GeV}/c^2$. However, these events were also compatible with other known processes and have not been sufficiently conclusive to claim a discovery [3].

Apart from the search for the Higgs boson CMS will also contribute to other fields. One of them is CP-violation in the B System. Up to now CP-violation could only be observed in Kaon decays. However, CP-violation effects are larger in B decays. In order to measure CP-violation, differences in selected decay rates of B-mesons have to be found. Unlike in the $K^0\bar{K}^0$system the lifetimes of the two weak eigenstates in the $B^0\bar{B}^0$ system are very similar. The separation of B^0 and $\bar{B}^0$ has to be made with flavour tagging, a method which allows to draw conclusions about the flavour composition of the decaying meson by looking at specific decay products (e. g., the charge of high momentum leptons from semileptonic decays). Due to the relatively long lifetime of B^0-mesons ($\sim 1.5\,\mathrm{ps}$) and due to the high energy of LHC, the Bs travel several mm in the detector before they decay. The distance between the (primary) production vertex and the (secondary) decay vertex can be resolved with the tracking system and provides an additional information for B-identification.

Another field of interest are precision measurements with top quarks. Top quarks almost exclusively decay into Wb. The W subsequently decays into fermion- or quark-pairs ($W \rightarrow \ell\nu$ or $W \rightarrow q\bar{q}$) and the b hadronises into a jet. Electrons and muons from the W decays have high transverse momenta and are expected to be isolated (i. e., they are well separated from the other decay products of the underlying event). Such leptons are relatively easy to detect and can be used as a tag for the top event.

But apart from the interesting pp collisions also $20 - 30$ uninteresting collisions happen simultaneously per bunch crossing (so called minimum bias events), leading to several thousand particle tracks every 25 ns. It is the challenging task of the detector systems to find the interesting decay products within this busy environment (i. e., the needle in the haystack). But fortunately, the momentum of the proton is not uniformly distributed among its constituents and the minimum bias events get a boost along the beam axis. Therefore, the average transverse momentum of such background-events is very low and most of them remain inside a narrow cone around the beam pipe. This makes it possible to search for interesting reactions that include heavy particles by requiring a high transverse momentum for some of the decay products.

1.2 The CMS Experiment

The Compact Muon Solenoid (CMS) and A Toroidal LHC Apparatus (ATLAS) are the two general purpose detectors foreseen at LHC. Figure 1.3 shows an exploded view of the CMS detector. As in a Russian matrioshka the single components are placed into each other. Every layer has its special task and covers as much solid angle as possible.

The outermost layer is the muon system. It is embedded in the iron yoke which acts on the one hand as flux return for the magnet and on the other hand as muon absorber. Many decay channels of b and c quarks, as well as of the Higgs boson, involve high momentum muons. These muons provide clear signatures for interesting events and can be used for the 1^{st} level trigger.

The next device is the superconducting solenoid. Within its radius of 2.95 m it creates a uniform magnetic field of 4 T. This rather high magnetic field allows the detector to be compact, without having to compromise on the momentum measurement capabilities.

The next layer consists of two calorimeters. The hadronic calorimeter (HCAL) plays an essential role in the identification of quarks, gluons and neutrinos by measuring the energy and direction of jets and of missing transverse energy.

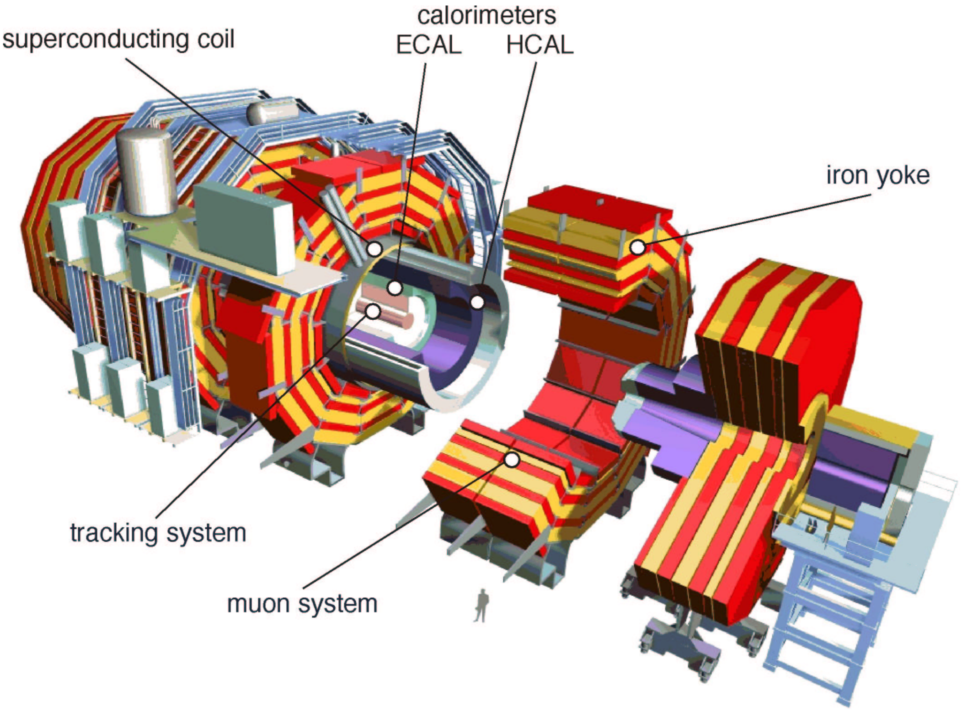

Figure 1.3: *Exploded view of the CMS detector.*

A high resolution electromagnetic calorimeter (ECAL) was one of the design objectives of CMS. In particular, it is optimised to measure the benchmark reaction $H \to \gamma\gamma$. This Higgs decay channel is the most promising one if the Higgs mass is lower than $\sim 150\,\mathrm{GeV}/c^2$. But of course the ECAL is also suited to precisely measure other photons or electrons (like e. g., from $H \to ZZ \to 4e^{\pm}$).

The central part of the CMS detector is dedicated to track reconstructions. The CMS tracker is radially subdivided into two single systems, namely the pixel detector in the innermost region and the microstrip detector in the outer part (see figure 1.4). Originally it was foreseen to build one part of the microstrip detector out of microstrip gas-chambers (MSGC) and the other part out of silicon strips. But in 1999 the decision was taken to abandon the MSGCs, in favour of a micro-strip detector based entirely on silicon. The new all-silicon strip detector uses $214\,\mathrm{m}^2$ silicon for $11.4\cdot10^6$ read-out channels in 10 layers (9 in the endcap). The read-out pitch varies between $80\,\mu\mathrm{m}$ and $210\,\mu\mathrm{m}$. More details about the silicon strip detectors can be found in [4, 5].

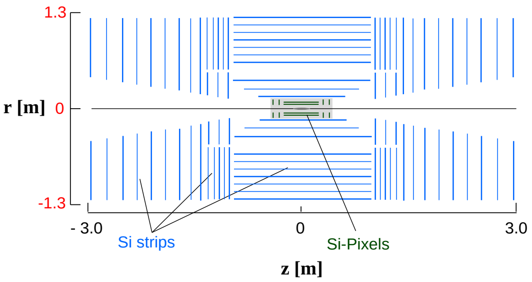

Figure 1.4: *The tracking system in CMS.*

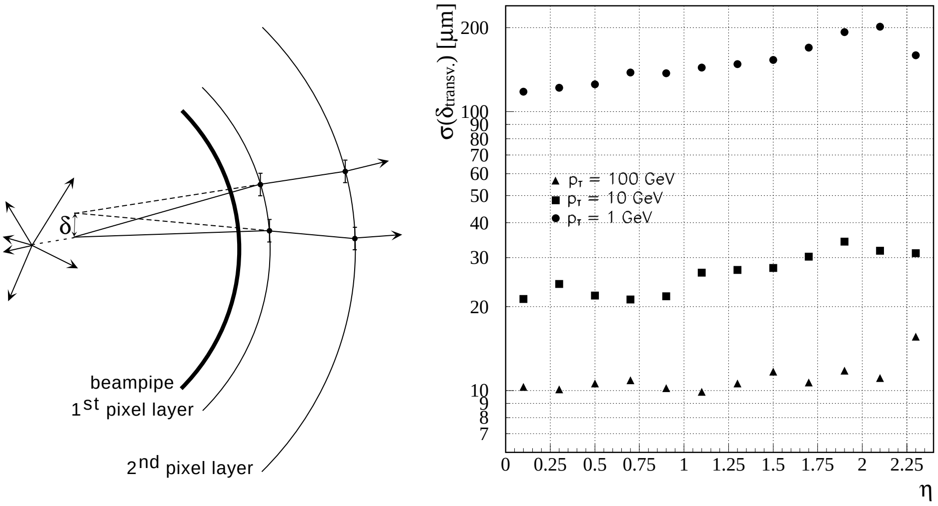

Figure 1.5: *Left: an explanation of the impact parameter δ. Right: transverse impact parameter resolution $\sigma(\delta_{trans})$ for muons with different transverse momenta versus pseudo rapidity (from [4]).*

1.3 The Pixel Vertex Detector

For the physics goals mentioned in section 1.1 a very good spatial vertex resolution is mandatory. This resolution is normally given in terms of the impact parameter δ, which is explained on the left side of figure 1.5. Due to multiple scattering at the different detector layers and due to the intrinsic detector resolutions the reconstructed tracks do not point to the real decay vertex, but to a point which is shifted from the real vertex by the impact parameter δ. To keep δ small the tracking stations should be located as close to the vertex as possible. Furthermore, the standard deviation $\sigma(\delta)$ (i. e., the impact parameter resolution) is dominated by the performance of the first tracking layers. The right side of figure 1.5 shows the simulated transverse impact parameter resolution $\sigma(\delta_{transv.})$ of the CMS tracker as a function of

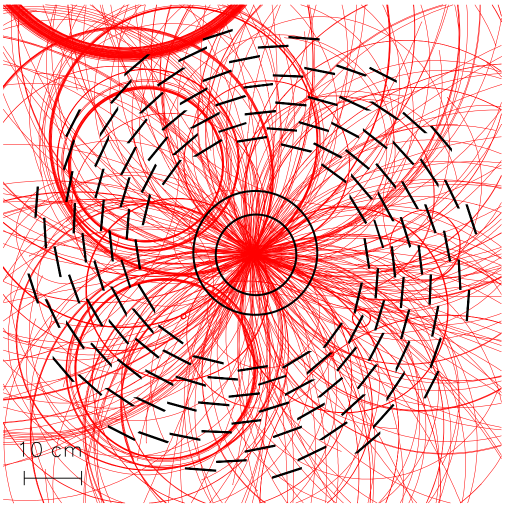

Figure 1.6: *A simulated Higgs decay $H \rightarrow ZZ \rightarrow 4\mu$ with 18 superimposed minimum bias events (from [6]).*

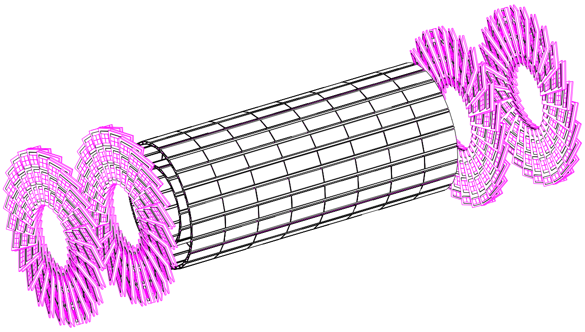

Figure 1.7: *Perspective view of the pixel system in the high luminosity configuration.*

pseudo-rapidity[1] η at the design luminosity of LHC.

Figure 1.6 shows the high track-density at the innermost tracking stations. It displays a simulated Higgs decay $H \rightarrow ZZ \rightarrow 4\mu$ with 18 superimposed minimum bias events, projected on a plane transverse to the beam direction. The high density of tracks due to the minimum bias events requires the two innermost layers of the tracking system to consist of pixels instead of microstrip detectors. The two rings in the centre of figure 1.6 denote the two pixel barrel layers in the high luminosity configuration (see below). About half of the silicon strip layers are also displayed (broken rings). At a radius of 25 cm and at design luminosity the innermost strip detector already has

---

[1] The rapidity y of a particle is defined as $y = \frac{1}{2} \ln \frac{E+P_p}{E-P_p}$, where E is the energy of the particle and P_p its momentum component parallel to the beam. Pseudo- rapidity η is the rapidity calculated neglecting the particles mass, $\eta = -\ln \tan(\theta/2)$, where θ is the polar angle with respect to the beam direction. Zero rapidity or pseudo-rapidity corresponds to particles moving at 90° from the beam-line, high values of y or η imply very forward or backward going particles.

an occupancy[2] of 0.052 [5]. For even smaller radii the occupancy of strip detectors would become so high that ambiguities in the track reconstruction could not be avoided any more. Compared to the strips the innermost pixel layer at $r = 4\,\mathrm{cm}$ has a moderate occupancy of $1.9 \cdot 10^{-4}$ [4].

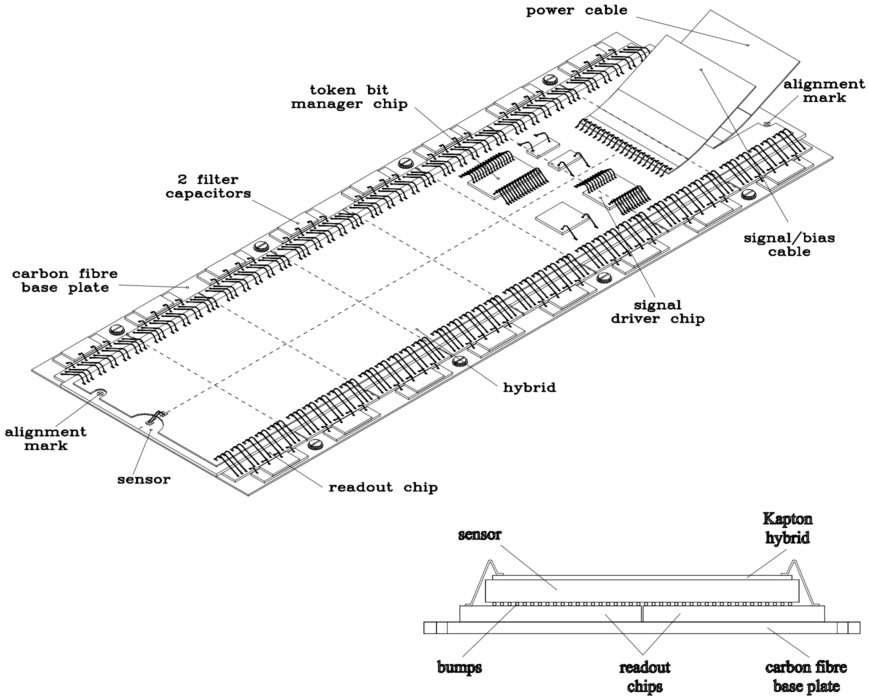

Figure 1.8: *A pixel barrel module with a* $1.6 \times 6.4\,cm^2$ *big sensor and 16 read-out chips. In the cross-sectional view the vertical scale is risen by a factor five.*

The CMS pixel system has two barrel layers and two end layers (disks) on each side of the barrel (see figure 1.7). The construction of the barrel layers is done by a European collaboration, whereas the end disks are developed by groups from the United States. The layers are composed of modular detector units, like the one in figure 1.8. These modules consist of a thin sensor plate with radiation hard readout chips. Each chip covers 52 × 53 pixels. The chips are connected through bond wires to hybrid circuits, which distribute the readout control signals and where the data signals are collected. Capton cables connected to the hybrids transmit the signals to and from a periphery situated at the outer region of the pixel system frame. The modules are attached to cooling frames, with the cooling tubes being an integral part of the mechanical structure.

The innermost barrel layer of the pixel detector is placed at a radius of $\sim 4\,\mathrm{cm}$. With a radiation hardness of up to $6 \cdot 10^{14}$ hadrons per cm^2, sensors

---

[2] Occupancy is defined as the average number of strips/pixels with hits divided by the total number of strips/pixels.

Table 1.2: *Number of channels and expected hit rates at* $\mathcal{L} = 10^{34}\,cm^{-2}\;s^{-2}$.

	Barrel			End cap	
Layer (at r or z)	4 cm	7 cm	11 cm	33 cm	47 cm
Number of chips	2340	2840	5888	1080	1080
Number of pixels	$6.35 \cdot 10^6$	$10.6 \cdot 10^6$	$16.2 \cdot 10^6$	$3.0 \cdot 10^6$	$3.0 \cdot 10^6$
Area	0.15 m^2	0.25 m^2	0.38 m^2	0.07 m^2	0.07 m^2
Pixel hit rate	24.0 kHz	10.3 kHz	6.9 kHz	lower	
Chip hit rate	12.0 MHz	8.2 MHz	7.6 MHz	lower	
Pixel occupancy	$1.9 \cdot 10^{-4}$	$3.3 \cdot 10^{-4}$	$1.7 \cdot 10^{-4}$	lower	

and read-out chips survive here during the first four years of LHC operation (assuming that during the first three years LHC will run with one third of its design luminosity). During this phase the barrel has two layers at approximately 4 cm and 7 cm. When a reasonable operation of the innermost layer is no longer provided it will be removed and a new layer is installed at 11 cm. Together with the layer at 7 cm it forms the high luminosity barrel configuration[3]. The four end disks have the same configuration for low- and high-luminosity conditions. After 6 or 7 years of operation at least the 7 cm barrel-layer and the inner end-disks will have to be replaced. Table 1.2 lists the number of channels, sensitive areas and hit rates for the different layers.

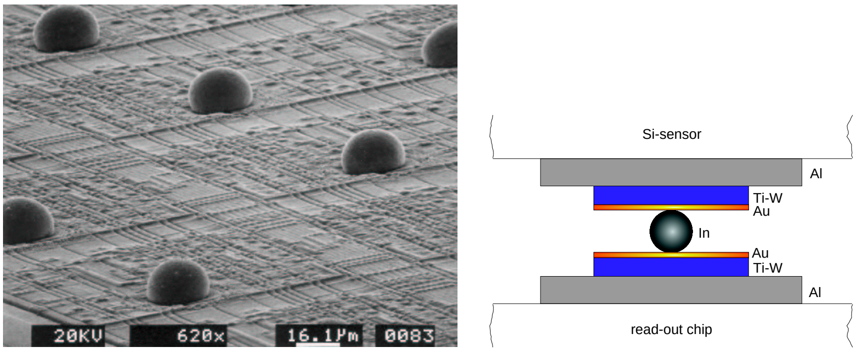

Figure 1.9: *Left: SEM scan of a read-out chip with reflowed bumps (the sensor was removed to take this picture); right: cross-section through the In-bump and the under-bump metal layers.*

The pixels deliver true space point information with high resolution. But they also lead to a series of technical challenges:

---

[3] An alternative possibility would be to use the 4 cm layer in the high luminosity configuration as well and to replace it every year. This scenario is under discussion at the moment.

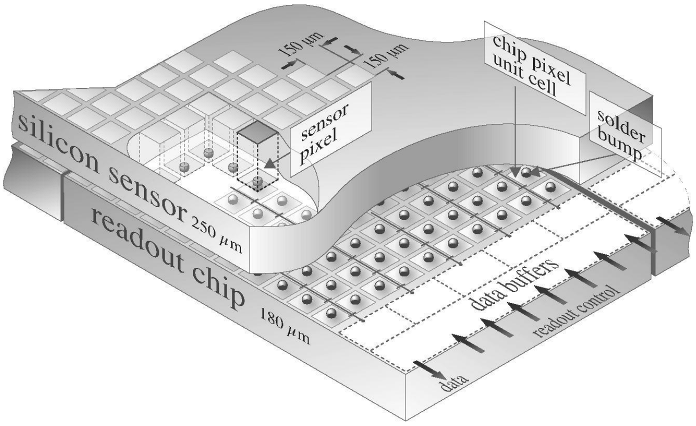

Figure 1.10: *Schematic view of a pixel detector element. Each sensor pixel is connected via a indium bump to a pixel unit cell on the read-out chip, where the signal is amplified. The hit data are stored on the edge of the chip where they wait for trigger confirmation.*

① Compared to the strips there are much more read-out channels per unit area, which requires an efficient zero suppression.

② The huge density of channels makes it impossible to connect the sensor and the read-out chip with conventional wire-bonds. Hence, new connection techniques had to be found.

③ The closer the detector is at the interaction point the higher is the dose rate that it has to withstand.

The solutions to the problems ① and ② are described in detail in the CMS Tracker Technical Design Report [4]. They are only briefly recapitulated here for reasons of completeness.

Each pixel has its own read-out circuit. Whenever a pixel is hit this circuit immediately copies the amplified analogue signal together with a pixel address and a time-stamp into a data buffer located in the periphery of the chip. There, the signals wait for the first level trigger. This makes sure that only pixel hits which are confirmed by a trigger are transmitted to the counting room.

The sensor pixels are connected to the read-out chip with the bump-bond or flip-chip technique (see figures 1.9 and 1.10). On top of each sensor- and electronics-pixel an indium pad is deposited using photo-lithography and evaporation techniques. To ensure a good ohmic contact an under-bump metallisation containing a gold- and a titanium-tungsten-layer is put on first, using the same techniques. Then, the chips are flipped, accurately aligned

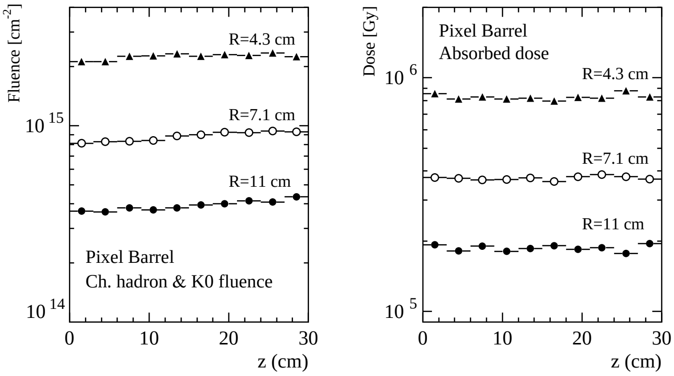

Figure 1.11: *The simulated total hadron fluence and absorbed dose of the whole pixel barrel (sensor + chip), projected to 10 years of operation ($5\cdot10^5\,pb^{-1}$, from [4]).*

and placed on the sensor. By heating this setup to about 150°C for a few seconds the indium melts and forms bumps, which connect the two devices.

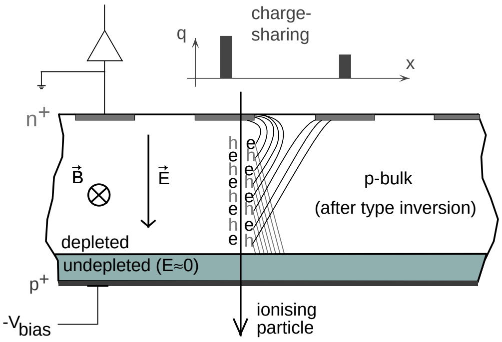

Figure 1.12: *Charge sharing due to the Lorentz effect.*

Concerning point ③ much attention has to be paid on radiation damages. How hostile the operation environment of the pixel detector will be can be seen from figure 1.11. Projected to 10 years of operation the innermost layer of the pixel barrel would pick up an integrated dose of $8\cdot10^5$ Gy. Keeping in mind that only a few Grays are already lethal for men it is surprising that such a sensitive device can operate several years under these conditions.

After detailed irradiation studies silicon was chosen out of three candidates (gallium arsenide, diamond and silicon) as sensor material [7]. In order to increase the useful operation lifetime of the silicon detectors, running with partial depletion must be anticipated. This is more suitable with n-type pixels, since after type inversion[4] the depletion region grows from the pixel side. In addition, n-type pixels with electron read-out have the advantage

---

[4] See section 2.3 for a definition of type inversion.

of more charge sharing among pixels: In $r\phi$ direction the signal charge is distributed among several pixels due to the Lorentz-effect, which is larger for electrons than for holes (see figure 1.12 and section 4.7, in z direction charge sharing is also present for inclined tracks). With sufficiently high charge sharing a centre of mass calculation can be made to improve the spatial resolution. For this reason an analogue readout was chosen. The detectors in the end disks are rotated by 20°with respect to the $r\phi$ plane in order to take advantage of the charge sharing as well, since otherwise the $\vec{\mathcal{E}}$ and $\vec{B}$ fields would be parallel.

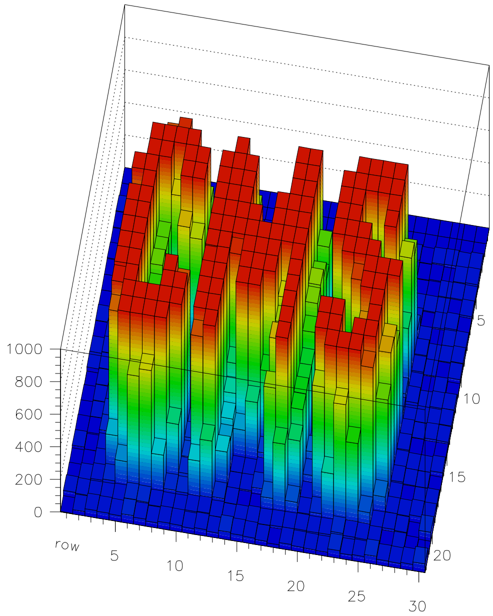

Figure 1.13: *An X-ray picture of a CMS brass-mask, taken with a prototype pixel detector.*

Since both, the $r\phi$ and z hit coordinates are important for localising vertices, a square pixel shape is preferred. The minimal pixel size is defined by the area needed for the pixel read-out circuit. The upper limit of the pixel size is given by the requirement for charge sharing among the pixels. As a compromise the CMS pixel collaboration decided to go for $150\,\mu$m × $150\,\mu$m pixels.

For the spatial resolution also the sensor thickness is important, since it influences the charge sharing pattern (see figure 1.12). For the final CMS pixel sensor standard $300\,\mu$m thick silicon wafers are ground down to $250\,\mu$m to reduce the multiple scattering of traversing particles. But for the measurements described in this thesis that step was omitted and $300\,\mu$m thick sensors were used instead.

In summer 2000 the spatial resolution was measured in a beam-test by our collaborators form the United States. They used unirradiated, $300\,\mu$m thick sensors with the pixel geometry described above and with a design as it was originally proposed in the Technical Design Report (see section 3.1 and [4]). In a magnetic field of 3 T the average resolution was $16.8\,\mu$m [8]. Older measurements, also performed at 3 T and with 300 μm thick sensors, but with a pixel size of 125 μm × 125 μm, led to a resolution of 12.8 μm [9].

The result of one of the first successful tests with a bump-bonded pixel assembly is displayed in figure 1.13. For this picture a 22 × 30 pixel prototype sensor with a bump bonded read-out chip was covered with a small 500 μm thick brass plate where the letters CMS were milled out. The picture was taken by illuminating the setup with 14 keV X-rays from a rubidium-source and using a random trigger.

CHAPTER

TWO

SILICON DETECTORS

In section 2.1 the texture of a silicon sensor is briefly explained. Section 2.2 contains a simulation of the production process and section 2.3 deals with irradiation effects.

2.1 Basic Principles

Semiconductor physics is treated in many textbooks (e. g., [10, 11, 12, 13]). The theories of signal charge generation and of deep level traps are explained in [14]. In this section only the basic functionality and layout of semiconductor position sensors are recapitulated. A description of the charge transport in high electric and magnetic fields is added in appendix B.

2.1.1 The pn-Junction as a Sensor

The basic operation principle of semiconductor detectors is based on the generation of mobile charges and their collection on signal electrodes. A penetrating charged particle or photon lifts valence electrons into the conduction band (creation of electron hole pairs). These charge carriers are then separated and collected with the help of an electric field.

This is normally accomplished with a reversely biased pn junction. It consists of a n-type and a p-type piece of silicon, which are brought together to form a junction. Because of the difference in the concentrations of electrons and holes between the two materials there is a drift of holes towards the n-region and a similar drift of electrons towards the p-region. As a consequence the drifting electrons fill up holes in the p-region while the drifting holes capture electrons on the n-side. Reminding that the n- and p-sides are initially neutral, this recombination also causes a charge build-up on either side of the junction. Since the p-region is injected with extra electrons, it becomes negative while the n-region becomes positive. This creates a potential difference (the "built-in" junction voltage V_i) leading to an electric field gradient across the junction. Due to this field a zone around the interface becomes free of mobile charges ("depletion zone").

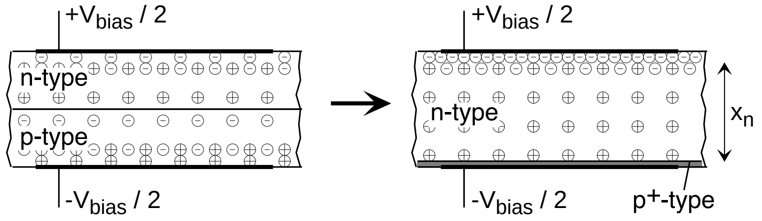

Figure 2.1: *A biased pn junction with two equally doped regions (left) and a one sided abrupt p$^+$-n junction (right).*

The width of this intrinsic depletion region is very narrow (in the order of $10\,\mu$m, which leads to $V_i \approx 0.5\,$V) and normally not sufficient for sensor operation (except e. g., in solar cells). Therefore, the width of the depletion region is artificially enlarged by applying a reverse bias voltage V_{bias} over the junction. This is displayed on the left side of figure 2.1. On the right side of figure 2.1 basically the same setup is drawn again, but this time with a very wide n-type region (called bulk silicon) and a extremely narrow p-type layer. This p-layer (labelled with p$^+$) is now doped several orders of magnitude higher than the n-type region. In appendix C it is shown that the voltage drop in the highly doped region can be neglected and that the width x_n of the depletion layer in the n-type region is given by (see equation (C.13))

$$x_n = \sqrt{\frac{2\varepsilon_{si}\varepsilon_o(V_{bias} + V_i)}{qN_D}} = \sqrt{2\varepsilon_{si}\varepsilon_o\mu_n\rho(V_{bias} + V_i)} \quad , \tag{2.1}$$

where N_D is the n-type doping concentration, q the elementary charge and $\varepsilon_{si}\varepsilon_o$ the permittivity of silicon ($1.05 \cdot 10^{-10}\,\mathrm{A\,s\,(V\,m)^{-1}}$). ρ (μ_n) denotes the resistivity (mobility) of the n-type doped silicon, respectively.

In the right side equation the depletion width is expressed in terms of the resistivity ρ, which is defined as

$$\rho = \frac{1}{q(\mu_n N_D + \mu_p N_A)} \approx \frac{1}{q\mu_n N_D} \quad , \tag{2.2}$$

where $N_{A,D}$ are the p-type (n-type) doping concentrations and μ_n (μ_p) the corresponding mobilities, respectively. The approximation on the right side holds for n-type sensors. Typical resistivities for sensors in particle physics are a few k$\Omega\,$cm.

To obtain a good ohmic contact to the outside world one normally also implants a shallow, but highly doped n$^+$ layer into the n-type bulk, opposite to the p$^+$ implant. This layer does not create a pn-junction. It has the only purpose to ensure a low-resistive contact to a metal layer on top of the implants, which is accessible with a bond wire or a bump bond.

To make such a detector position sensitive one has to divide either the narrow p$^+$ layer or the n$^+$ contact implant into small strips or pixels and connect each one to a read-out circuit. In figure 2.2 one can see how this is accomplished in the CMS pixel detector.

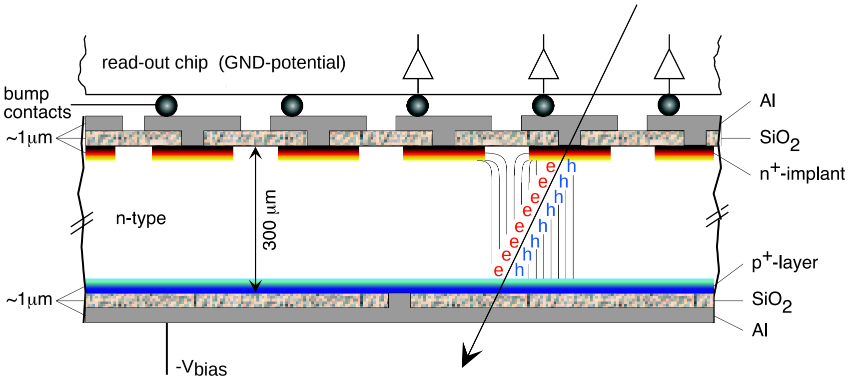

Figure 2.2: *Schematic cross section of the CMS pixel sensor, the implants are isolated against the overlying metal lines by a thin SiO$_2$ layer, with openings where a contact is required. A charged particle track creating e-h pairs is also shown (lengths are not to scale!).*

The ohmic contact layer is segmented into pixels. Each n$^+$ pixel implant is connected to a read-out channel. The junction sits on the backside, at the p$^+$ implant. The implants, oxide- and metal layers are about 1 μm thick, whereas the the whole sensor typically has a thickness in the order of 300 μm.

These so called n$^+$-in-n pixels would all be electrically connected by the n-type silicon in between, if one would leave them like in figure 2.2 (there is no isolating pn junction between them). Even after full depletion there is still a conductive surface regime at the silicon - silicon dioxide interface which allows a charge to flow. To isolate the pixels one or two narrow p$^+$ implants are laid around each n$^+$ implant (not shown in figure 2.2). These p-stop rings completely restrain a charge flow between the pixels if the bulk volume around them is fully depleted. For this thesis a novel design of such p-stop rings was tried. Small openings should provide a high resistive path between the pixels, which would allow a controlled and slow charge flow from pixels with an insufficient connection to the read-out chip. The design of these open p-stop rings is described in section 3.1 and their performance in 4.1.

The choice to segment the n$^+$ implant and not the p$^+$ one is mainly driven by radiation damage considerations (see section 2.3). Due to radiation damages the n-type bulk silicon will change to a p-type behaviour during its lifetime. In this case the junction sits between the pixel implants and the bulk, and the depletion zone grows from the pixel side. If, for some reason, full depletion cannot be reached any more (e. g., because the full depletion voltage exceeds the break-down voltage) there is still a usable depletion volume around the pixels.

2.1.2 Signal Acquisition

During the last years detailed measurements and simulations of the charge collections process were made within the CMS pixel collaboration [7] to study the signal formation in irradiated silicon. It was found that, in a partially depleted sensor, a small fraction of the signal charge carriers approaches the read-out nodes well behind the fast signal. These charges originate from the undepleted region, where a small rest field still allows them to drift to the read-out nodes. The signal formation is also influenced by trapped charges, which induce a mirror charge on the read-out electrodes. In addition, it was found that the charge collection efficiency is also strongly design dependent. Especially the width of the n^+ implants is of crucial importance. In this thesis the investigations on this subject went on (see section 4.2).

After the signal charge carriers (electrons in case of the CMS pixel detector) reach the pixel they have to be collected and amplified. This is usually done with a charge sensitive amplifier. The charges are integrated on a capacitor which acts as a feedback in an inverting amplifier stage (see figure 2.3).

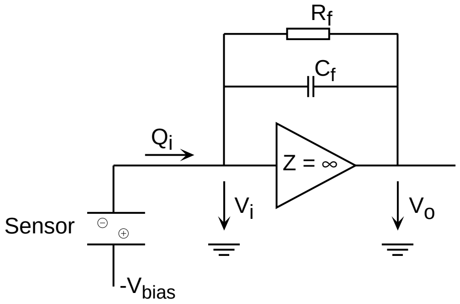

Figure 2.3: *Block diagram of a charge sensitive amplifier with capacitive and resistive feedback.*

If we neglect for the moment the resistor R_f the schematic in figure 2.3 shows a simple integrator. If the voltage gain of the amplifier is $A = -V_o/V_i$, the voltage difference across C_f is given by $V_f = (A+1)V_i$. The charge deposited on C_f is $Q_f = C_f V_f = C_f(A+1)V_i$. Since the input impedance of the amplifier is assumed to be infinite, the input charge is equal to the charge on C_f ($Q_f = Q_i$). With these relations the effective input capacitance C_i becomes

$$C_i \equiv \frac{Q_i}{V_i} = C_f(A+1) \quad , \tag{2.3}$$

which leads to the charge gain

$$A_Q \equiv \frac{V_o}{Q_i} = \frac{AV_i}{C_i V_i} = \frac{A}{C_i} = \frac{A}{A+1}\frac{1}{C_f} \approx \frac{1}{C_f} \quad . \tag{2.4}$$

Equation (2.4) holds for high voltage gains A. After each charge integration such a system has to be "reset" (i. e., discharge the capacitor C_f). This is done with the resistor R_f. V_o then decreases exponentially with a time constant $\tau_{RC} = R_f C_f$. C_f and R_f have to be chosen in a way that on the one hand all charges can be collected and that the signal is not cut off by the resistive feedback (lower boundary) and on the other hand no pile up[1] effects occur (upper boundary).

2.2 The Processing of Silicon Devices

This section deals with the production of silicon wafers and sensors. In the first part the production methods of silicon wafers are given, whereas the second part explains the sensor production by means of a process simulation.

Most semiconductor sensors are fabricated by processes that have originally been developed for CMOS electronics[2]. The main advantages lie in the small patterning capabilities and the ability to produce thousands of identical structures in one run, which leads to a much improved performance-to-cost ratio compared to other production techniques.

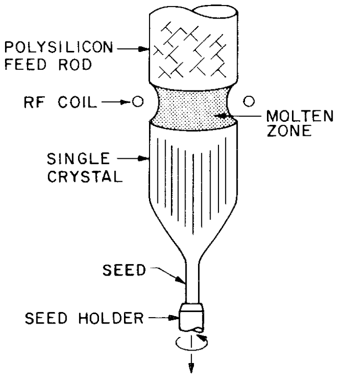

Figure 2.4: *The principle of the float zone process (from [13]).*

Sensors, like the one in figure 2.2, are processed by a successive deposition and patterning of thin solid films on a $\sim 300\,\mu$m thick crystalline silicon plate (called wafer). Such wafers are produced out of pure quartz-sand (SiO_2).

---

[1] Pile up can occur with high pulse frequencies, when the capacitor is not yet completely discharged at the arrival of a new signal pulse.

[2] CMOS: Complementary Metal On Semiconductor, a standard processing technique for integrated micro-electronics.

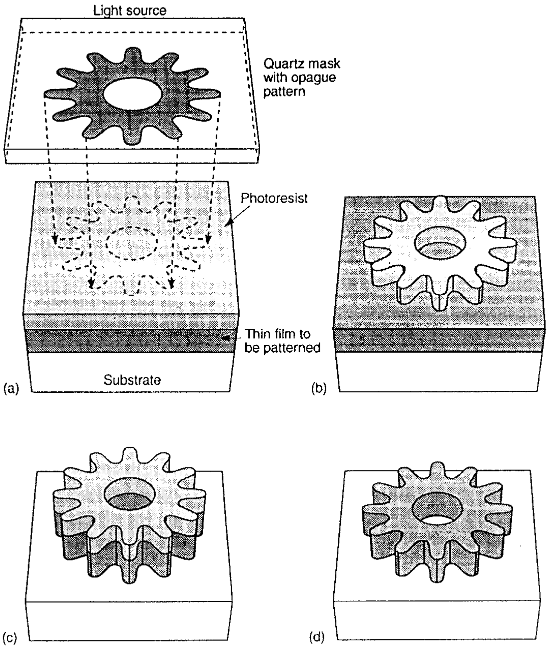

Figure 2.5: *Process steps in planar lithography: (a) Projection of pattern onto photo-resist, (b) photo-resist development, (c) etching of film beneath photo-resist, (d) photo-resist removal, leaving patterned film behind (from [15]).*

Brought in contact with carbon and heated, SiO_2 changes to polycrystalline silicon ($SiC + SiO_2 \rightarrow Si + SiO + CO$). The poly-silicon is then chemically purified and molten in a furnace. To grow a silicon single crystal a seed with the correct crystal orientation is dipped into the melt and slowly pulled out. From this seed the single crystal starts to grow and a long rod can be pulled (Czochralski technique). Such rods can already be doped by adding a certain amount of dopant to the melt (e. g., phosphorus for n-type silicon or boron for p-type rods).

Czochralski silicon is normally used for electronic circuits. For sensors the concentration of impurities in Czochralski silicon is still too high. Therefore, the float zone process is used (see figure 2.4). A high purity polycrystalline rod with a seed crystal is held in a vertical position. A small zone of the crystal is kept molten by a radio-frequency heater, which is moved from the seed upwards. A single crystal freezes out below the heater and grows as an extension of the seed crystal. The final single crystal rod is then cut into slices. After cleaning and polishing these slices can be used as wafers. For sensor productions, rods with diameters of 100 mm (4 in) or 152 mm (6 in) are normally used.

The patterns for the doping layers and the thin SiO_2 and metal films are created with photo-lithography (see figure 2.5). It begins with a computer generated mask with the planar geometry of the corresponding layer defined by transparent and opaque regions. A thin film of photo-resist is then deposited on the wafer, covering the film to be patterned. After exposing the photo-resist to a light source and after a chemical development step, the mask image is transferred onto the photo-resist and the film. The remaining photo-resist, in turn, acts as a resistant mask when the underlying material is processed with chemical treatment, ion implantation, or other process steps.

For a better understanding of the specifications of the vendors of our test sensors I have performed a process simulation with the ISE-DIOS program [16]. The aim was to reproduce the specifications of the sensor-manufacturer CSEM[3]. The single steps of this process simulation are given in the following as an example of a production process. More details and variations of production processes can be found in [13, 17].

- Starting with the bare wafer, a 7000 Å thick oxide layer is deposited on both sides, e. g., $SiH_4 + 2O_2 \rightarrow SiO_2 + 2H_2$ (450°C, LT-CVD[4]).
- For the implantations, openings have to be etched into this oxide layer, using photo-lithography and plasma etching.
- A second, 800 Å thin screening oxide is then thermally grown (by heating the device in a oxygen atmosphere) to protect the silicon surface during the ion implantation.
- To make the implants ions are accelerated and shot into the wafer. The regions which should not be implanted are protected with a thick layer of photo-resist. For the n^+ implantation $7 \cdot 10^{14}$ phosphorus ions per cm^2 with a kinetic energy of 140 keV are used, whereas the p^+ implantation is done with $1 \cdot 10^{15}$ boron ions per cm^2 of an energy of 60 keV. The vertical distribution of the phosphorus and boron ions is shown in the following figures (calculated with TRIM [18]). The first 800 Å correspond to the SiO_2 layer:

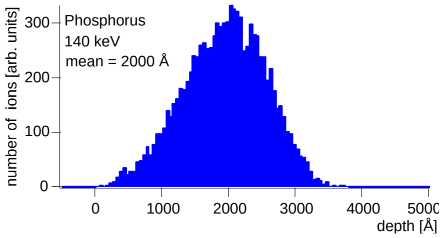

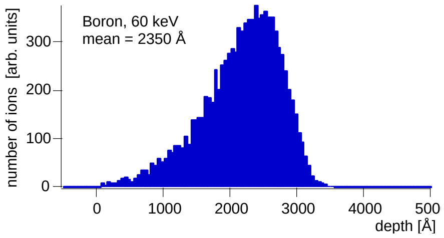

- The wafer is then heated to 930°C for 5 h in a gas mixture of O_2 and N_2. On the one hand this heating causes the ions to diffuse into the bulk and to heal crystal defects caused by the ion bombardment, and on the other hand the silicon surface oxidises, resulting in a new

---

[3] Centre Suisse d'Electronique et de Microtechnique in Neuchâtel, Switzerland.

[4] CVD: Chemical Vapour Deposition, a technique where several compounds in their gas-phase are thermally broken into their components. Some of these components nucleate on the substrate forming a film. LT-CVD: low temperature CVD, LP-CVD: low pressure CVD.

SiO_2 layer. The thickness of this layer was simulated to be 2200 Å. After this heating step, the dopings reach about 1.5 μm in the bulk. The simulated profiles after this diffusion step look as follows:

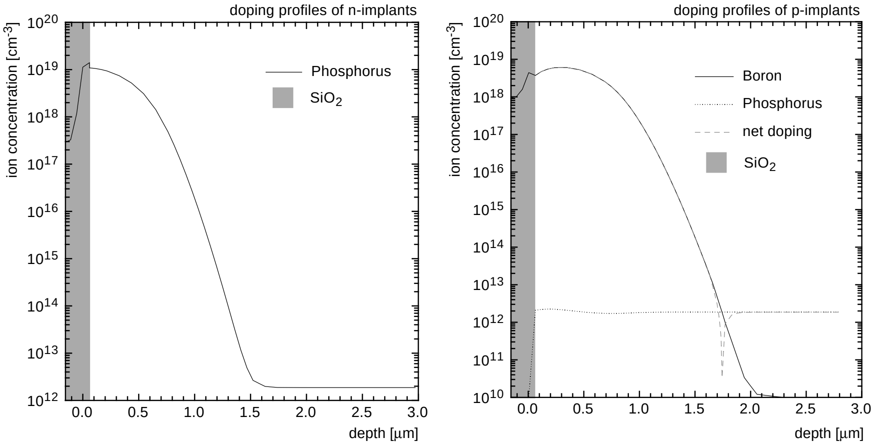

- On top of the thermal oxide a 1250 Å thick silicon nitride (Si_3N_4) layer is deposited to protect the underlying structures and decouple possible pin-holes[5]. Such a layer is also deposited with CVD processes, like $3SiCl_2H_2 + 4NH_3 \rightarrow Si_3N_4 + 6HCl + 6H_2$.
- After opening contact holes in the nitride and the oxide layer by chemical etching, 1 μm of an aluminium-silicon alloy is sputtered on the wafer, followed by its patterning via plasma etching.
- The last step consists of growing a 9000 Å thick SiO_2 passivation layer on top and etch out openings to provide contacts to the metal layer.

Figure 2.6 shows a zoomed in cross section through one of the devices simulated with the process described above. For length comparison reasons the final implantation depth after diffusion (1.5 μm) is marked with an arrow.

2.3 Radiation Damage Effects

Radiation damage in silicon devices was already studied 30 years ago in the context of aerospace applications (see e. g., [19]). At that time the interest was mostly focused on MOS-transistors and the doses were limited to $\sim$ 1 Gy. But as we have seen in chapter 1 the integrated doses for the inner detector layers in CMS will be in the order of 10^5 Gy. To investigate the detector behaviour after such high doses several R & D projects were initiated in the last years (e. g., [20]).

The damages can be categorised into two classes: bulk defects and surface defects. The bulk damages are caused by non-ionising energy losses leading

---

[5] An unwanted hole in the SiO_2 layer.

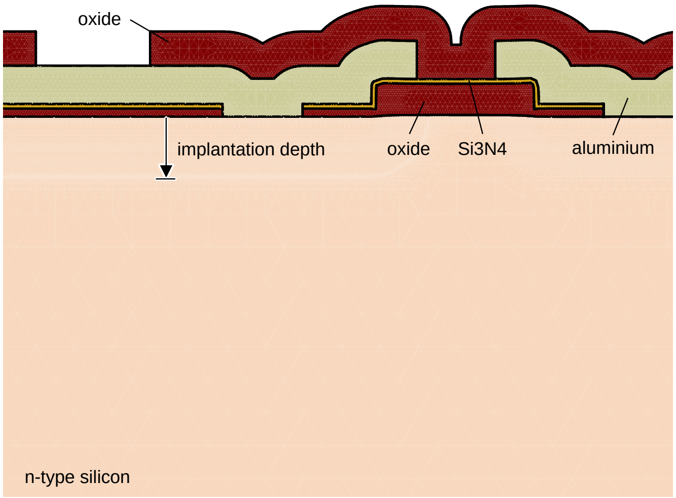

Figure 2.6: *Detail of a sensor surface simulated with the process described in the text (using the program ISE-DIOS [16]), the arrow denotes the implantation depth and its length corresponds to 1.5 µm.*

to crystal defects. The surface effects are based on changes at the Si-SiO_2 interface. The consequences for the detector performance mainly depend on the sensor design and the processes used during its production.

2.3.1 Bulk Defects

According to the current understanding bulk radiation damages are produced in a two step process: first, silicon atoms are displaced from the lattice due to collisions with the traversing particles. These processes are described in the first part of this section. The lattice defects then slowly diffuse through the bulk and start to form complexes (beneficial/reverse annealing), which is the subject of the second part of the section.

Very rarely a traversing high energetic particle makes a head-on collision with one of the silicon atoms. This atom is kicked out of its initial lattice site and moves several hundred angstroms through the silicon bulk (primary knock-on atom - *PKA*). During this passage it looses its energy by ionisation and by collisions with other atoms, displacing them and producing so called vacancy-interstitial-pairs (VI-pairs or Frenkel defects). In figure 2.7 such a *PKA* is simulated with 50 keV recoil energy. Some of these VI-pairs recombine immediately, but others are left over which start to diffuse through the bulk.

Experimentally, it was found that the displacement damage scales with the amount of energy imparted in the original displacing collision with the *PKA*.

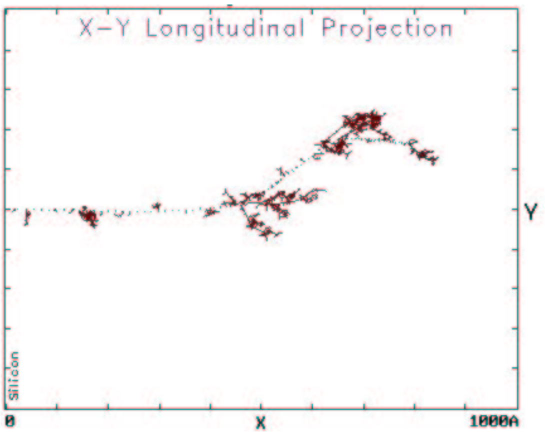

Figure 2.7: *Damage cascade of a 50 keV PKA, the cascade starts on the left side. Dots mark the PKAs path and the clusters denote Si atoms which are kicked out of the lattice by the PKA (simulated with TRIM [18]).*

This fact is known as the *NIEL* hypothesis[6]. This energy depends on the energy and type (mass, charge, …) of the incident particles - besides the silicon atom mass. Therefore, a *NIEL* factor can be given for each particle type and energy. Due to historic reasons the *NIEL* factor is normally expressed relative to the *NIEL* of 1 MeV neutrons (the *NIEL* of a 1 MeV neutron in silicon equals $1.983\,\mathrm{keV\,cm^2\,g^{-1}}$ [21]). Detailed calculations showed that for particle energies higher than $\sim 100\,\mathrm{MeV}$ the *NIEL* factors of protons, pions and neutrons are very similar [22]. More details about *NIEL* calculations can be found in [23] and [24] and references therein.

Macroscopically, the leakage current and the doping concentration are the most important parameters affected by radiation defects. Experimentally, one finds that the increase of the leakage current ΔI linearly depends on the applied fluence[7] Φ [25]

$$\Delta I_{vol} \equiv \frac{\Delta I}{\mathrm{V}} = \alpha \cdot \Phi \quad , \tag{2.5}$$

where V is volume of the silicon device.

Figure 2.8 shows this linear dependence for diodes irradiated with $300\,\mathrm{MeV}/c$ pions. During the last years many such measurements were performed with various types of particles. It was found that α slightly depends on the irradiation time and on the annealing[8] scenario (time, temperature, environmental conditions). The RD48 (ROSE) collaboration at CERN proposes a 80 min annealing at +60°C instead of 10 days at room temperature, which corresponds to 5 yearly maintenance periods for the LHC detectors. With this annealing scenario and for fluences normalised to the *NIEL* of 1 MeV neu-

---

[6] *NIEL* - Non ionising energy loss.

[7] Fluence: time integrated flux.

[8] A brief introduction to annealing is given on page 26.

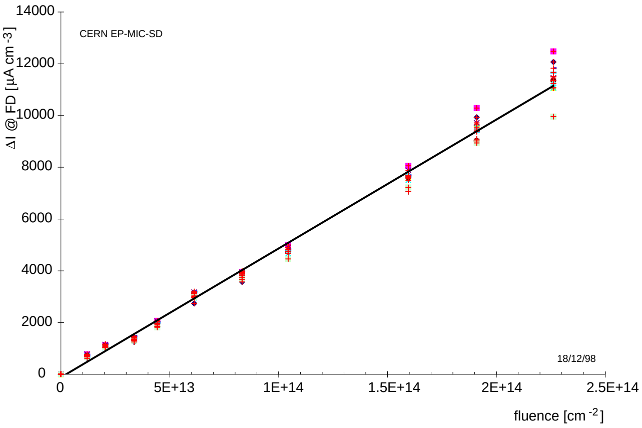

***Figure 2.8:** Leakage current increase after irradiation with 300 MeV/c pions and 4 min annealing at 80° C [26].*

trons one finds for the damage constant [24]:

$$\alpha = (4.0 \pm 0.2) \cdot 10^{-17}\,\mathrm{A\,cm}^{-1} \quad . \tag{2.6}$$

The radiation damages also influence the effective doping concentration $N_{\mathit{eff}} = |N_D - N_A|$, where N_D (N_A) denotes the donor (acceptor) concentration, respectively. These changes are important since they influence the achievable depletion width x_n for a given bias voltage. After irradiation, N_D has to be replaced by N_{eff} in equation (2.1):

$$x_n = \sqrt{\frac{2\varepsilon_{si}\varepsilon_0 (V_{bias} + V_i)}{qN_{\mathit{eff}}}} \quad . \tag{2.7}$$

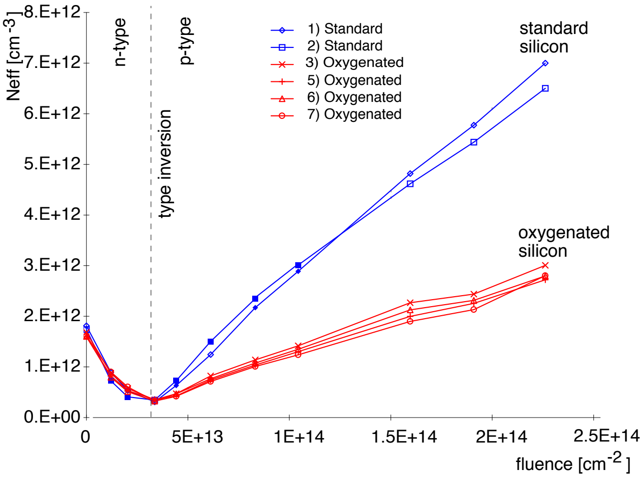

***Figure 2.9:** Effective doping concentration of n-type diodes vs. pion fluence (300 MeV/c) after 4 min. annealing at 80° C. Measurements on standard and oxygenated silicon are displayed [26].*

The pion-fluence dependence of the effective doping concentration N_{eff} of a n-type sensors is displayed in figure 2.9 (obtained with CV-measurements on test-diodes, see section 3.3). At low fluences N_{eff} decreases to a minimal value (called type inversion point, see below), but linearly increases again towards higher fluences. This behaviour can be described by [25]

$$N_{eff} = |N_D e^{-c_D \Phi} - N_A e^{-c_A \Phi} - \beta \phi| \quad , \tag{2.8}$$

where the first term describes the donor removal, the second the acceptor removal and the linear term with the parameter β denotes the radiation induced introduction of electrically active traps (if the energy level of a trap lies in the band-gap, it is said to be electrically active, see [27]). From spectroscopic measurements one knows that most of the electrically active traps are acceptor-like[9]. Therefore, an initial n-type device is more and more compensated until it reaches an almost intrinsic state and then starts to behave p-type like. In addition, This effect is accelerated by the radiation induced donor removal, which is due to electrically not active complexes which absorb donor atoms. The second term in equation (2.8) can be neglected for n-type devices since the initial acceptor concentration is negligible.

Figure 2.9 shows another peculiarity concerning the irradiation behaviour: Devices with high oxygen concentrations behave better after irradiation than standard silicon sensors do. Oxygen is one of the impurities that are always present in silicon. But normally, its concentration is tried to be kept as low as possible (smaller than $10^{15}\,\mathrm{cm}^{-3}$). It was found that a high oxygen concentration ($\sim 10^{17}\,\mathrm{cm}^{-3}$) reduces the radiation induced acceptor introduction rate β (see equation (2.8)). Many measurements with oxygen enriched devices (so called oxygenated silicon) from different vendors were carried out during the last years [20]. All of them showed that oxygenated devices always have a β factor at least as low as the best standard materials. Up to now the reasons for this amazing behaviour is not fully understood. There are some hints that oxygen supports the formation of defect complexes that are not electrically active[10] [28].

After the creation of initial defects due to a *PKA* the remaining vacancies and interstitials diffuse away from their creation place and form complexes containing different defects and/or impurity atoms, like $\mathrm{V} + \mathrm{V} \rightarrow \mathrm{V}_2$, $\mathrm{I} + \mathrm{V}_2 \rightarrow \mathrm{V}$, $\mathrm{V} + \mathrm{O} \rightarrow \mathrm{VO}$ or $\mathrm{V} + \mathrm{VO} \rightarrow \mathrm{V}_2\mathrm{O}$, where V denotes a vacancy in the crystal, I an interstitial silicon atom and O an oxygen atom (see [28] for more details). Some of these reactions bring two electrically active defects together to form an inactive complex (beneficial annealing). But also the reverse, two inactive defects clustering to an active one, is possible (reverse annealing).

---

[9] Acceptor like traps are negative when filled and neutral when empty, donor like traps are neutral when filled with an electron and positive when empty.

[10] With a low oxygen concentration many acceptor-like $\mathrm{V}_2\mathrm{O}$ complexes are formed, which are believed to be the main source for the radiation induced acceptor increase. If the oxygen concentration is very high, it is more likely that the vacancies V find an oxygen atom to form a VO complex than to undergo the a reaction $\mathrm{V} + \mathrm{VO} \rightarrow \mathrm{V}_2\mathrm{O}$.

Unfortunately, a satisfactory theory which relates these defect complexes to macroscopic parameters does not exist yet. Instead, one relies on pure empirical models for macroscopic predictions.

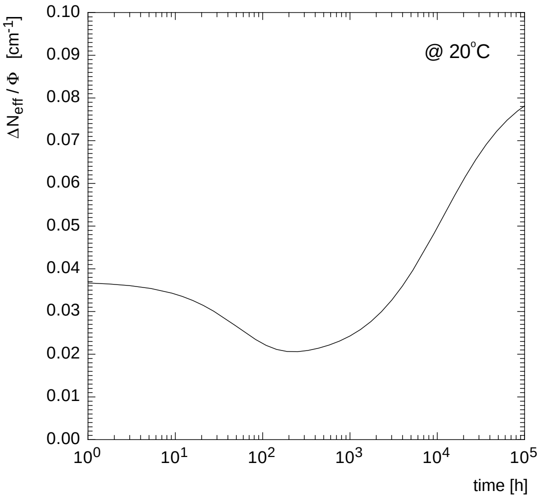

Figure 2.10: *Change of N_{eff} with time due to annealing for a n-type silicon sensor at 20° C, which was irradiated with an equivalent fluence of $3 \cdot 10^{14}\,cm^{-2}$. Calculated with a model described in [20].*

An example of a typical annealing behaviour at room temperature is displayed in figure 2.10. It was calculated with the so called Hamburg model, whose parameters were found by making fits to experimental data [20, 24]. The fluence was $\Phi = 3 \cdot 10^{14}\,\mathrm{cm}^{-2}$ (normalised to the *NIEL* of 1 MeV neutrons). During the first 200 hours the beneficial short term annealing is dominating (regime with negative slope in figure 2.10). Afterwards, in the reverse annealing regime, the effective doping concentration steeply rises and the sensor becomes more and more p-type. For higher temperatures the reverse annealing processes are extremely accelerated. An example can be found in figure 4.63 in section 4.6.

2.3.2 Surface Defects

So far, the assumption was made that the whole sensor volume changes its properties in a uniform manner. However this is not true at the silicon-silicon dioxide interface.

Radiation induced changes in the SiO_2 layers also influence the underlying silicon. When an ionising particle traverses the SiO_2 layer, it creates electron-hole pairs. Many of these pairs recombine immediately, especially when no electric field is applied. If an electric field is present (e. g., in a sensor under bias) the separation probability increases. Due to their high mobility in SiO_2 the electrons are quickly swept out of the oxide layer ($\mu_e \approx 20\,\mathrm{cm}^2\,(V\,s)^{-1}$). The holes, which have a much smaller mobility in SiO_2 ($\mu_h \approx 2 \cdot 10^{-5}\,\mathrm{cm}^2\,(V\,s)^{-1}$), are left behind and slowly move to the Si-SiO_2 interface, where they are permanently trapped. Therefore, a permanent layer of positive charge is present in the oxide, very close to the silicon-silicon dioxide interface. It saturates when all traps are filled, which typically happens at a surface charge of $\sim 3 \cdot 10^{12}\, q\, \text{cm}^{-2}$.

This positive oxide layer induces a negatively charged layer in the silicon bulk, at the interface with the oxide. It consists of freely movable electrons and is known as electron accumulation layer. It influences parameters like the flat band voltage V_{FB}, the maximal electric field strengths between the implants or the inter-pixel resistance R (see sections 4.2 and 4.3).

During irradiation, interface defects (or interface traps) are also created. They can be due to dangling bonds between the Si atoms and the SiO_2 molecules or due to displaced silicon atoms close to the interface. These traps act like the deep level defects in the bulk, leading to additional leakage currents, called surface currents. Partly, they are already present before irradiation due to a mismatch of the lattice constants between silicon and silicon dioxide.

As far as the effective doping concentration is concerned, the situation at the surface is rather different than in the bulk. Measurements of irradiated MOS-capacitors in this work (section 4.3) clearly show that a shallow silicon layer at the surface does not undergo type inversion but remains n-type, even after a fluence of $6 \cdot 10^{14}\, \text{cm}^{-2}$. Up to now it is not clear which processes are responsible for this abnormal behaviour. It is thought that the defect formation processes close to the surface differ from the processes deeper in the bulk [14]. Investigations concerning this subject are still going on.

CHAPTER

THREE

DESIGNS

The radiation induced changes of the sensor properties described in the last chapter can partly be cushioned by using an adequate sensor design. Since the influence of design variations on the sensor properties is difficult to describe analytically it is inevitable to draw different designs and determine the best one empirically.

3.1 Design Variations

The mask files for all design variations described in this section are self made using the KICBox [29] and Cadence [30] software packages. Afterwards these mask files were submitted to two different vendors which produced the sensors (section 3.2). The inspection of the wafers from the two vendors is described in section 3.3.

3.1.1 P-Stop Designs

For n-in-n pixel sensors the pixels are made of n^+ silicon in an n-type substrate, and have thus to be isolated from each other. This is usually done with one or several narrow p^+-rings around each pixel, called p-stop ring.

In order to avoid the excessive charging of an unbonded pixel the isolation between the pixels should not be perfect. There are two different approaches. The ATLAS pixel collaboration avoids the p-stop rings and uses a p-spray implant instead. It consists of a lightly doped p-layer which is “sprayed” over the whole wafer without any masking step. The n^+ implants are not affected because the boron concentration in the p-spray layer is far too small to compensate for the phosphorus concentration. However, the n-substrate in-between the pixels can be compensated, leading to a shallow p-layer at the surface, forming a weak p-n junction with the substrate [31].

We have chosen a different approach. Here a narrow resistive path between the pixels prevents the pixels from charging up. This is accomplished by small openings in the p-rings which lead to an atoll-like structure (see figure 3.1). The resistivity of the path between two pixels is controlled through its length (e. g., by laying several such open rings around one pixel) and through its width.

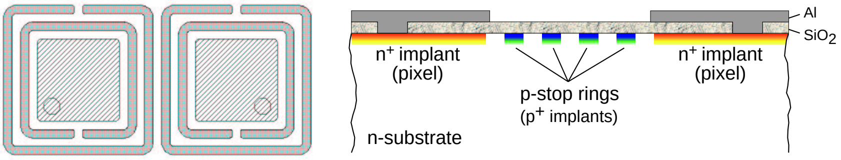

Figure 3.1: *Atoll-like open p-stop rings around two pixels. Left: top view; right: horizontal cross section.*

The idea of open p-stop rings is very new and was never tried before. Since there is no experience concerning the pixel isolation with atoll-like p-stop rings several p-stop designs had to be investigated. Since the different parameters in a design are highly correlated, changing one parameter always means that others have to be changed as well. This implies that they cannot all be optimised. I investigated the influence of the gap width between the p-stop rings and the overall length of the resistive path between the pixels (e. g., by measuring the difference in resistance between one and two p-stops around each pixel). Figures 3.2 to 3.4 give an overview of the different designs that have been tested.

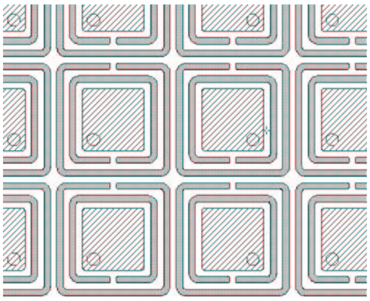

Figure 3.2: *The design originally proposed in the Technical Design Report [4]: a 78 μm wide pixel with two 8 μm wide, 8 μm spaced p-stop rings. Three variations of this design with p-stop gaps between 8 μm and 14 μm were also implemented.*

Most of these pixel-designs have been implemented in two different types of test-sensors. On one hand there are bump-bondable 22×30 pixel structures, which contain three different gaps between the p-implants. In addition, the same design variations have been implemented on small 5×5 pixel structures which are already hard-wired with metal lines for dedicated measurement purposes. These devices are equipped with wire bond pads which can also

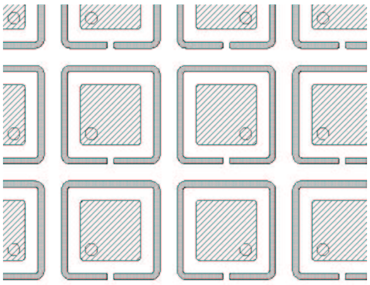

Figure 3.3: *One p-stop ring instead of two, the gap between the rings is 22 μm.*

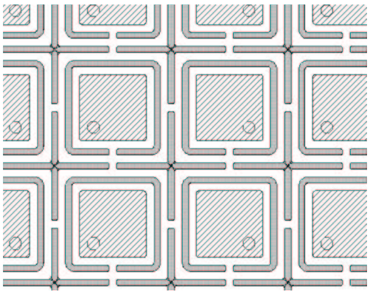

Figure 3.4: *A single atoll ring with an additional cross ("1.5 p-stop rings") with gap variations between the p-implants.*

be accessed with probe needles. Two examples of such devices are shown in figures 3.5 and 3.6. One (figure 3.5) was used to measure the pixel isolation. If one of the pixels marked with an apple is held at a potential $V \neq 0$ and all others are at ground one can measure the current between them and calculate an inter-pixel resistivity (see section 4.1). The device in figure 3.6 served for the investigation of p-stop potentials. The four small metal pads in the centre are connected to the four p-stop rings between two pixels. They can be accessed with probe needles. Due to the small width of the p-stop rings (8 μm) the contact opening between the silicon and the metal layer had to be smaller than allowed by the design rules. Therefore, two of these contacts failed and only the other two could be accessed. Since the measurements after irradiation required high voltage operation all devices were equipped with guard rings. Therefore they could similarly be used for guard ring tests.

3.1.2 Multi-Chip-Sensors

In the final CMS Pixel Detector 16 read-out chips are bump bonded to one sensor (see section 1.2). The bump bond technique is a very new bonding method which is still under development - especially with bump sizes as small as 15 μm. Placing several chips well aligned onto one sensor is a demanding task which still needs to be practised.

In order to test the multi-chip setup with real signals several multi-chip sensors for 2, 4 and 8 chips were designed. Between the chips some part of

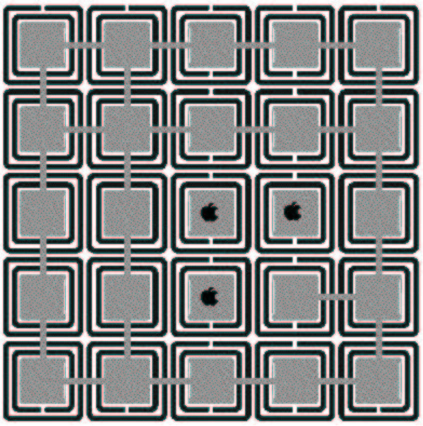

Figure 3.5: *Device for pixel isolation measurements. The pixels marked with an apple are accessible with probe needles.*

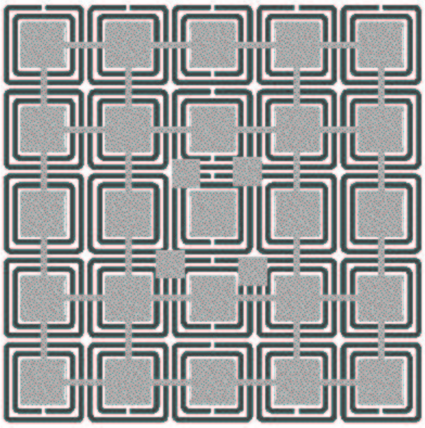

Figure 3.6: *Device for the investigation of p-stop potentials.*

the sensor cannot be covered by active chip area, since the chip size is slightly larger than its active area. This requires pixels situated between chips to be either rectangular instead of square, or that some intermediate pixels are routed to neighbouring pixels connected to a chip. Figure 3.7 shows a detail of a multi-chip sensor with the latter solution.

Figure 3.7: *Detail of a multi-chip sensor showing the region between two chips.*

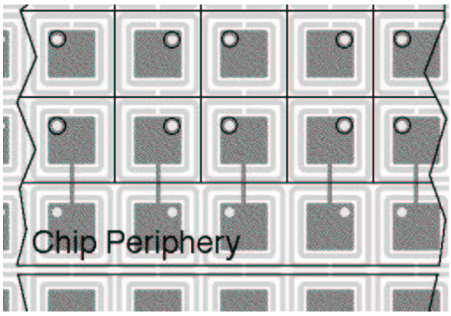

3.1.3 Guard Rings

The increase of the effective doping N_{eff} during irradiation (described in section 2.3) requires the bias voltage to be increased to 1000 V or more to maintain full depletion. Such high voltages can lead to extremely high field strengths. To prevent breakdown, guard-rings have to be introduced to decrease the electric potential in a controlled way. With a n-type substrate this is normally accomplished with several floating p$^+$ implants (see figure 3.8). By applying a reverse bias voltage to the backside p$^+$ implant (the area on top right in figure 3.8) a depletion zone builds up. When the lateral extension of the depletion zone reaches the first floating guard ring (figure 3.9), this ring charges up to a potential (if we neglect the built-in voltage of the p-n junction)

$$V_{guard\text{-}ring_1} \simeq V_{bias} - \frac{qN_D d^2}{2\varepsilon_{si}\varepsilon_0} \quad , \tag{3.1}$$

where V_{bias} is the bias voltage, N_D the donor concentration and d the distance between the two p$^+$ implants. This mechanism is called punch-through[1]. With several such structures in series a very high bias voltage can be degraded in a controlled way.

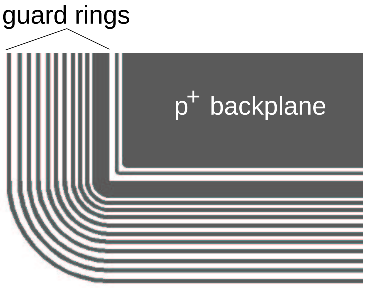

Figure 3.8: *Example of a guard ring structure for a pixel detector. The p$^+$backside implant is indicated on top right. All the rings are covered by a metal layer. Dimensions are given in the text.*

Figure 3.9: *The punch-through mechanism. The reverse bias is applied between the left p$^+$implant and the pixel-side of the sensor (not shown).*

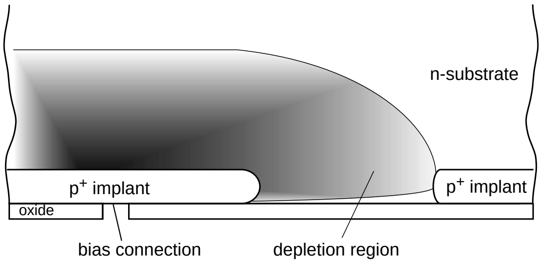

Guard rings are especially important close to the scribe line[2] of the sensor. Due to the cutting process the lattice (and hence also the energy band structure) is completely destroyed along the cut edge. Therefore, the front-side and the backside of the sensor are electrically connected through the

---

[1] This effect is also well known in MOSFET transistors. It is one of the limiting factors in scaling down device dimensions. As the channel length is reduced the depletion layer widths of the source and the drain junction of the transistor become comparable to the channel length. Punch through takes place when the two depletion layers merge, which causes the gate to lose control of the current.

[2] A synonym for cut edge.

cut-edge. Guard rings close to the cut edges help to avoid high electric field strengths by controlling the potential gradient on one or both sides of the sensor.

The implementation of the guard rings in the CMS pixel sensor is outlined in figure 3.10. Using the bump bond technique to connect the read out chip to the sensor implies that the grounded chip typically sits 15 μm above the sensor surface. Already a moderate potential difference can lead to a discharge over such a short distance. Therefore, it is mandatory to have the whole pixel (front-) side of the sensor at the chip potential - including the scribe line. The potential drop $V_{bias} \rightarrow GND$ has to occur on p-side (backside) of the sensor, which requires all the guard rings to be on the p-side.

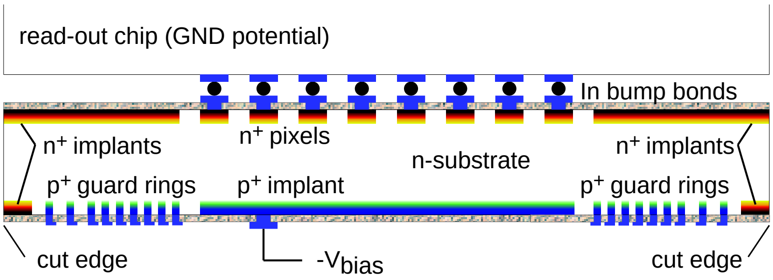

Figure 3.10: *Illustration of the guard ring concept. The whole potential drop happens on the (p$^+$) backside of the sensor (lengths are not to scale).*

In practice, the exact height of the potential barrier over each of these punch through structures strongly depends on the distance (equation (3.1)), on the surface quality (e. g., oxide charges), on the device leakage current and on many other parameters (see e. g., [32]). Therefore, analytical predictions concerning breakdown are very difficult and not very reliable. Furthermore, the guard ring behaviour is also influenced by radiation damages. To find a guard ring design which meets the specifications of the CMS pixel detector several guard designs have been drawn, irradiated and measured. The results of these measurements can be found in section 4.4.

One example of a guard ring was already shown in figure 3.8. This guard ring structure was used for all 22 × 30 pixel devices. The distance between the p$^+$ guard rings varies between 15 μm for the innermost rings and 30 μm for the outermost ones. All the guard rings have a width of 15 μm, except the innermost one which is 70 μm wide. In addition, there is an aluminium layer on each ring (called field plate), which is not shown in figure 3.8 for clarity reasons. It laterally extends the p$^+$ implants by 4 μm on both sides (figure 3.11).

To save space a simpler guard design was used for the 5 × 5 pixel test-

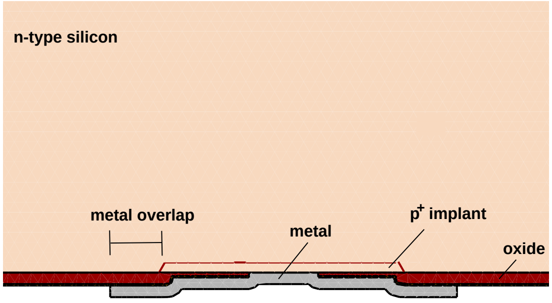

Figure 3.11: *Overlapping metal field plates on top of the guard rings.*

structures (figure 3.12). It consists of six guard rings only. They are equidistantly aligned with a distance of 30 μm. The ring width is 20 μm. They are also covered by a metal field plate which laterally extends 5 μm over the the p$^+$ implants on both sides.

Figure 3.12: *Guard rings for the* 5 × 5 *pixel structures.*

Since the energy band structure is completely destroyed at the scribe line it is important that the lateral extension of the depletion zone (and hence the electric field lines) never reaches this area. Else, a huge generation current would start to flow towards the electrodes. Simulations indicate (see figure 3.13) that the field lines in the bulk indeed reach out over the guard ring area. Therefore the distance from the outermost guard-ring to the scribe line is a crucial parameter.

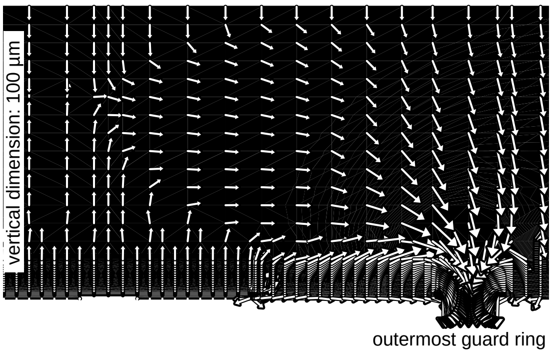

Figure 3.13: *Simulated lateral extension of horizontal electric field lines beyond the guard ring area [16].*

To test the influence of the distance between the outermost guard and the scribe line three different designs have been drawn. In the large distance case the distance between the guard rings and the scribe line amounts to $622\,\mu$m, in the intermediate case it is $372\,\mu$m and in the small one $256\,\mu$m. The empty area from the last guard ring to the the cut edge was filled with a n^+ implant in all cases. A similar n^+ layer was used on the n-side from the cut edge to the the sensitive pixel area.

Besides all this conventional guard rings, a more unusual design was also implemented. Instead of several closed p-rings a "brickwall" of "p^+ bricks" is laid around the diodes (see figure 3.14). The single "p^+ bricks" can choose their potential individually, which is probably an advantage compared to a conventional guard ring design, where an entire guard ring is held at the same potential. Especially the corners of a device can cause problems with conventional designs since the bending of the guard rings can lead to increased electric field strengths. Because of the quite high lateral diffusion during the processing ($\sim 1\,\mu$m) the p-n junctions are smoothed and a wave-like pattern of p^+- and n^- dopings is formed, which also helps to keep the maximal electric field strength small (see e. g., [11]). This "brickwall"-idea was implemented in two different versions, one with 14 layers of "p^+ bricks" and one with 28.

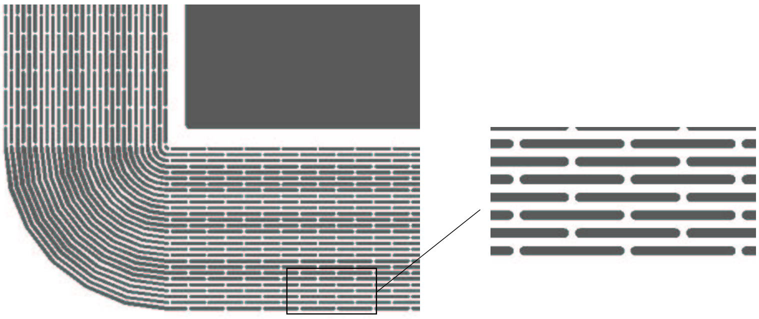

***Figure 3.14:** A "brickwall" like guard ring design with 28 layers of "p^+ bricks".*

3.1.4 Pixel Capacitance

The total capacitance of one pixel is the sum of the capacitive coupling to its neighbours and the plate-capacitance to the backplane. The capacitance to the backplane can easily be calculated, but not the capacitance to the neighbour pixels.

The total pixel capacitance is estimated to lie between 10 fF and 100 fF, which is too small to be measured directly. Therefore, the basic idea for my pixel capacitance measurement was to connect many pixels in parallel and measure this capacitance. For this measurement a special 22 × 30 pixel metal-on-silicon structure was designed - the so called parallel router chip in figure 3.15. Every fourth pixel is connected to a common pad (marked with a cloverleave in figure 3.15). All the others (the neighbours) are also connected and routed to another pad. Such a structure was bump bonded to a 22 × 30 pixel sensor. In this way 140 pixel-capacitances were connected in parallel. This required a capacitance measurement resolution of a few tenth of a pF.

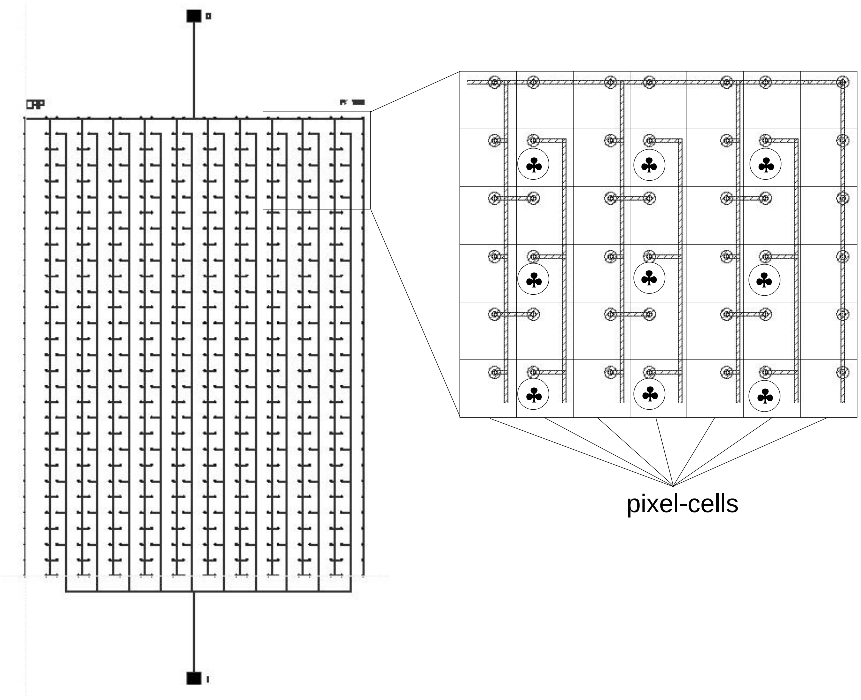

Figure 3.15: *Parallel router chip for the pixel capacitance measurement, in the magnified part the pixels are indicated for clarity reasons.*

The stray-capacitance[3] of the parallel router chip was measured separately with a second setup and subtracted. Therefore, another pixel structure was used which only contained the metal layer of the sensor, but no implants. All the metal pads were connected (figure 3.16). This structure was placed on the parallel router chip described above. Thin capton pads on the corners provided a spacing between the parallel router chip and the dummy pixel sensor which was comparable to the diameter of the indium bumps. The capacitance of this setup corresponds to the stray capacitance of the measurement with a bumped pixel sensor.

---

[3] The parasitic capacitance between the metal lines of the parallel router chip, between the connecting cables, etc.

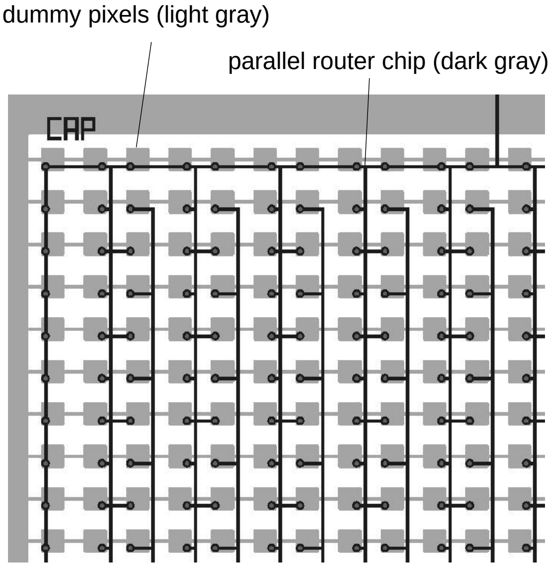

Figure 3.16: *A special structure to measure the stray capacitance. Capton pads between the light and the dark gray shaded metal structures provide an adequate spacing corresponding to an indium bump diameter.*

3.1.5 MOS Capacitors and Gated Diodes

MOS capacitors and gated diodes are suitable tools to measure the oxide charge and the effective doping density. Two different designs have been implemented. A larger one in order to decrease lateral effects (see figure 3.17 left, a schematic cross section of the same device is shown in figure 3.24) and a smaller one with several gate rings, which was provided by the ROSE RD48 collaboration at CERN (figure 3.17 right). Since this structure was included in several submissions of different groups (mainly from CMS and ATLAS) it allowed a one to one comparison between different vendors. Details about this structure can be found in [33].

In table 3.1 the different design variations are summarised. A photograph of the produced devices on the wafer is displayed in figure 3.18.

3.2 Submissions

The designs described in section 3.1 were submitted to two different vendors: CSEM[4] and SINTEF[5]. The submissions were done in April 1999 (with CSEM) and October 1999 (with SINTEF). Both vendors used four inch, n-type wafers as starting material. The processing was double sided.

The CSEM submission was a joint project of the University of Zurich, PSI and the protein crystallography group at the new Swiss Synchrotron Light Source SLS. It used the CSEM MAXIS technology. A detailed description

---

[4] Centre Suisse d'Electronique et de Microtechnique SA, Neuchâtel, Switzerland.

[5] SINTEF Electronics and Cybernetics, Microsystems, Oslo, Norway.

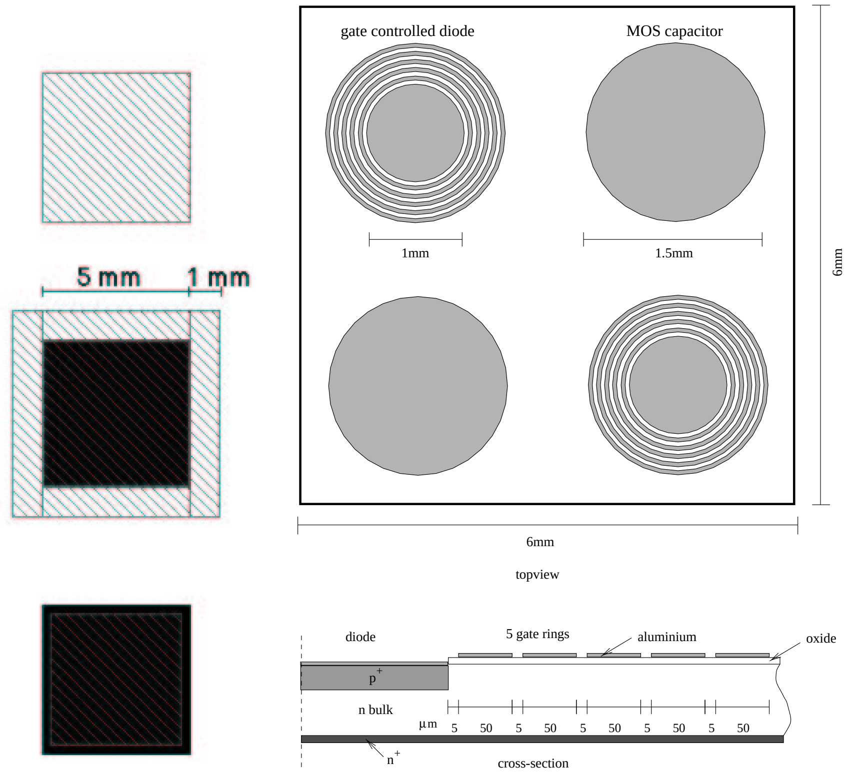

Figure 3.17: *MOS capacitors and gated diodes.*

of the production steps in this technology is given in section 2.2, additional information can be found in [17]. The whole batch consisted of eight high resistivity ($\sim 10\,\mathrm{k\Omega\,cm}$) and 16 low resistivity wafers ($\sim 2\,\mathrm{k\Omega\,cm}$). The high resistivity detectors were only used for the Synchrotron Source applications, since they would like to avoid high bias voltages. All wafers had $\langle 111\rangle$ crystal orientation and a nominal thickness of $300\,\mu\mathrm{m}$. Originally it was planned to have some low resistivity wafers with an increased oxygen concentration (see section 2.3). But due to technical problems at CSEM no oxygenation could be performed and all wafers were delivered with a standard, low oxygen concentration. One of the low resistivity wafers is shown in figure 3.18.

CSEM also performed the under bump metallisation (UBM). This special metallisation is necessary to guarantee a good electrical contact between the indium-bump and the process-given Al-pads of the sensor, which very easily oxidise. This UBM consisted of two sputtered layers, namely a Ti-W alloy and a Au-layer on top (see figure 1.9). The gold protects the contact from oxidation. Unfortunately gold diffuses very easily into silicon and has therefore to be separated by an intermediate Ti-W layer.

The wafers that have been processed by SINTEF contained designs from the University of Zurich, Purdue University (West Lafayette, Indiana, USA) and

Table 3.1: *Summary of the different design variations, n: n-implant width, p: gap between p-stops rings. The numbers in the first column denote the location on the wafer shown in figure 3.18.*

1	22×30 pixel; 2 open p-stops; $\mathrm{n} = 78\,\mu\mathrm{m}$; $\mathrm{p} = 8, 10, 12\,\mu\mathrm{m}$
2	22×30 pixel; 2 open p-stops; $\mathrm{n} = 68\,\mu\mathrm{m}$; $\mathrm{p} = 10, 12, 14\,\mu\mathrm{m}$
3	22×30 pixel; 2 open open p-stops; $\mathrm{n} = 68, 78, 88\,\mu\mathrm{m}$; $\mathrm{p} = 8\,\mu\mathrm{m}$
4	22×30 pixel; 1 open p-stop; $\mathrm{n} = 68, 78, 88\,\mu\mathrm{m}$; $\mathrm{p} = 8\,\mu\mathrm{m}$
5	22×30 pixel; 1 open p-stop + cross; $\mathrm{n} = 78, 86, 94\,\mu\mathrm{m}$; $\mathrm{p} = 8, 10, 12\,\mu\mathrm{m}$
6	same as 1, but with angular corners
7	22×30 pixel; 2 open p-stops; $\mathrm{n} = 78\,\mu\mathrm{m}$; $\mathrm{p} = 8\,\mu\mathrm{m}$
8	5×5 pixel devices with design variations similar to 1 - 7
9	parallel router chip for capacitance measurements
10	diodes with different guard rings
11	multichip sensors for 2, 4, and 8 chips
12	MOS capacitors + gated diodes for material- and process-quality tests
13	52×53 pixel sensor (final size)
14	metal on silicon fan-out to use silicon strip read-out chips
15	similar to 1 - 7
16	general purpose $2 \times 2\,\mathrm{mm}^2$ diodes

Fermilab (Chicago, USA). They consisted of $\langle 100 \rangle$ silicon and were $270\,\mu$m thick (nominal). The resistivity value given by SINTEF was 1-2 $\mathrm{k}\Omega\,\mathrm{cm}$. In total 17 wafers were produced, three out of them oxygenated (with an oxygen concentration of $2 - 3 \cdot 10^{17}\,\mathrm{cm}^{-3}$, in standard silicon wafers the oxygen concentration is lower than $1 \cdot 10^{15}\,\mathrm{cm}^{-3}$). One oxygenated wafer and one with standard oxygen concentration were available for the tests described in this thesis.

3.3 Test of Wafer Properties

For every masking step during the processing a new alignment of the mask had to be made. An alignment error (e. g., of a metal to substrate contact) can lead to the failure of a whole detector in the worst case. Furthermore, the deposition of oxygen, silicon-nitride, aluminium, etc. normally requires several heating and cooling cycles. The different thermal expansion coefficients of these materials can lead to mechanical stress on the surface which results in an increased curvature of the wafer or in small cracks on the surface. All such defects can be optically detected (section 3.3.1). The leakage current and depletion behaviour of the detectors before irradiation are determined by intrinsic properties of the starting material, such as defect concentration and doping density. These properties can be experimentally checked by I-V and C-V measurements of diodes (sections 3.3.2 and 3.3.3). Section 3.3.4 contains sheet resistivity and doping density measurements of the implants.

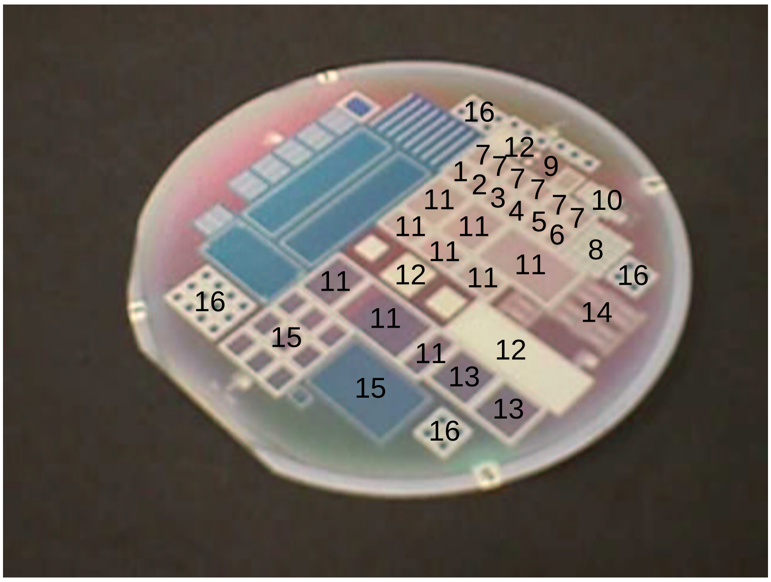

Figure 3.18: *A picture of a wafer with the sensor prototypes (delivered by CSEM). The numbers correspond to the devices in table 3.1. The structures without numbers were for projects not related to CMS.*

3.3.1 Optical Inspection

First, the wafers were optically inspected under a microscope. The surfaces looked clean and very few hints of mechanical stress could be found. The UBM layer (the Ti-W/Au metallisation for the bump bonding) was misaligned by $\sim 2\,\mu$m on most wafers. But it turned out that this misalignment is negligible since the the bump pads are all of dimensions $\geq 15\,\mu$m. The curvature was measured with the help of a microscope and a x-y table. The microscope had a focal-length measurement facility. With this tool the change in the focal lengths for several points on the wafer could be determined. On two perpendicular axes through the wafer 13 points have been chosen with the x-y table (figure 3.19).

The measured changes of the focal lengths along the axes have been fitted with a polynomial of degree three. This is plotted for wafer 10 in figure 3.20. This was one of the worst cases of surface bending that was found in the whole CSEM batch. Amazingly, no visible signs of stress could be found on this particular wafer in spite of the quite high curvature.

Average surface bendings are plotted in figure 3.21. Here, it is noteworthy that the forces which caused the surface bending did not pull into the same direction on the whole wafer. This indicates that the stress conditions have not been the same everywhere.

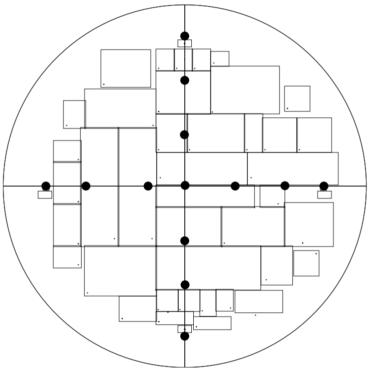

Figure 3.19: *For 13 points on the two axes the change in focal length has been measured to get the wafer curvature.*

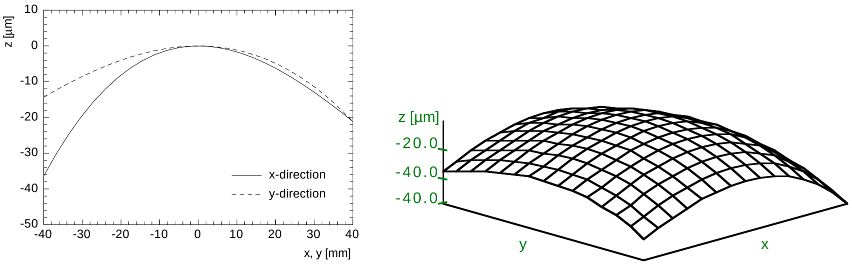

Figure 3.20: *The curvature of wafer 10. Left: fits in x- and y-direction with a polynomial of degree three, right: a surface plot of the same functions. Notice the enlarged scale of the z-axis.*

3.3.2 I-V Measurements

Impurities in the silicon bulk of the detectors can increase the bulk leakage current drastically. Electrons have first to be excited from the valence band to the conduction band. Since the thermal energy at room temperature ($3kT/2 \approx 0.04\,\mathrm{eV}$) is much lower than the activation energy for an electron hole pair (3.6 eV), the probability of direct excitation is extremely low. The excitation normally occurs in two or more steps through intermediate states in the band gap, which are created by impurities and defects in the crystal lattice. Such excitation and recombination statistics are described in detail by the Shockley-Read-Hall (SRH) theory [34].

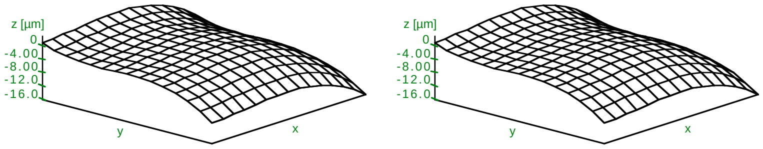

Figure 3.21: *Curvatures of two other wafers.*

To check the silicon quality one normally measures the leakage current of a reversely biased diode as a function of the bias voltage (I-V measurement). A sudden rise of the current at a certain bias voltage is a sign for breakdown (see section 4.4), which is caused either by a local accumulation of defects somewhere in the bulk or by mask misalignments. If breakdowns occur only in certain parts of a wafer they were most probably due to the first cause.

For each wafer, I-V measurements on three different, reversely biased diodes were performed. The results for the CSEM wafers 1-10 are shown in figure 3.22. Only two out of these 30 diodes in total had a breakdown below 500 V (not from the same wafer). Three showed a sudden increase to a higher plateau value between 50 and 100 V. All three originate from the same wafer (this wafer was excluded from the pixel prototype tests). One diode had an increased leakage current already from the beginning. To summarise, from the leakage current point of view most of the wafers generally showed a satisfying performance.

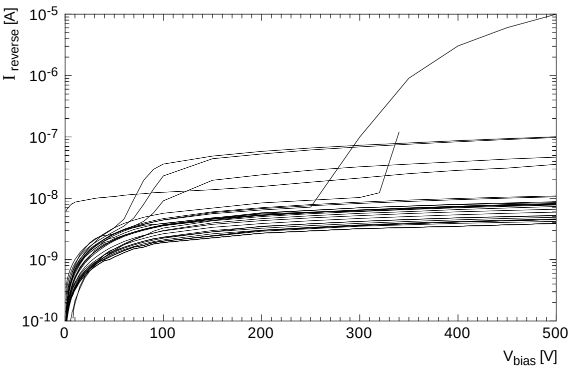

Figure 3.22: *Leakage currents of three different $2 \times 2\,mm^2$ diodes on CSEM wafers 1-10.*

3.3.3 C-V Measurements

C-V measurements on diodes can be used to investigate the bulk doping concentration and hence the resistivity of the wafers. Assuming an abrupt p^+-n junction, the depletion depth x_n can be written as (see appendix C)

$$x_n = \sqrt{\frac{2\varepsilon_{si}\varepsilon_o}{qN_D}\left(V_{bias} + V_i\right)} \quad , \tag{3.2}$$

where V_i is the built-in voltage of the junction, V_{bias} the reverse bias voltage, N_D the donor concentration and q the elementary charge. The depletion region capacitance C is obtained as

$$C = \frac{\varepsilon_{si}\varepsilon_o A}{x_n} = A\sqrt{\frac{q\varepsilon_{si}\varepsilon_o N_D}{2(V_{bias} + V_i)}} \quad , \tag{3.3}$$

where A is the area of the p-n junction. From equation (3.3) we obtain

$$\frac{1}{C^2} = \frac{2(V_{bias} + V_i)}{\varepsilon_{si}\varepsilon_0 q N_D A^2} \quad . \tag{3.4}$$

Thus, a plot of $1/C^2$ versus V_{bias} gives a straight, rising line as long as the depletion region is still growing, and a flat line after the depletion region extends over the whole thickness of the device. From such a measurement the full depletion voltage can easily be found. Figure 3.23 gives a nice example of such a graph for a $5 \times 5\,\mathrm{mm}^2$ diode from the oxygenated SINTEF wafer. For this wafer the full depletion voltage was determined to be 171 V.

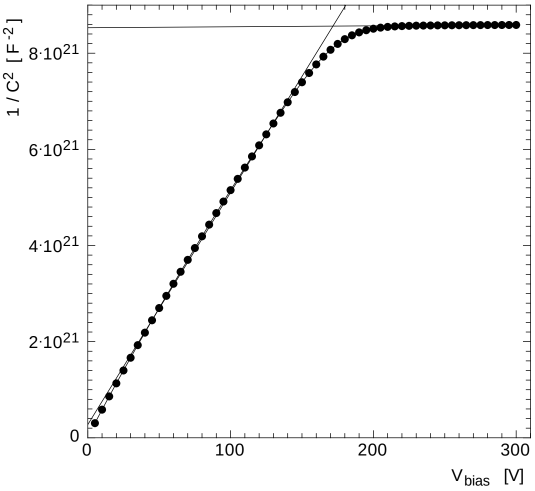

Figure 3.23: *Example of a $5 \times 5\,mm^2$ diode C-V-measurement to determine the full depletion voltage (oxygenated wafer from SINTEF).*

To avoid lateral effects at the edge of the diode, gated diodes (like the ones shown in figures 3.17 and 3.24) were used instead of standard ones. They provide perpendicular electrical field lines even at the edge of the p^+ implant. The capacitance is determined by superimposing a small AC signal (~0.1 V, ~10 kHz) on the bias voltage and the diode-contact, and measuring the phase shift and amplitude difference between the voltage and the current (see figure 3.24).

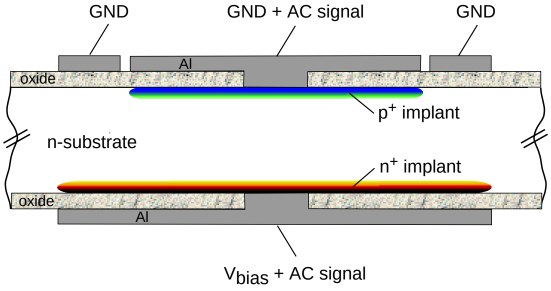

Figure 3.24: *Side view of a gated diode with a design shown in figure 3.17 (lengths are not to scale).*

The systematic C-V analysis for all wafers resulted in full depletion voltages V_{FD} between 140 V and 150 V for the CSEM wafers, and 171 V (183 V) for the oxygenated (non-oxygenated) SINTEF devices. For the CSEM wafer a full depletion voltage of 140 V was assumed for the following calculations. From (3.2) the donor concentration of the bulk N_D can be obtained:

$$N_D = \frac{2\varepsilon_{si}\varepsilon_o(V_{FD} + V_i)}{qd^2_{\text{wafer}}} \quad . \tag{3.5}$$

The wafer thicknesses d_{wafer} were measured with a Mitutoyo precision distance meter. The thicknesses of the CSEM wafers varied between 311 μm and 329 μm (mean = (320 ± 6.5) μm, nominal 300 μm). For the SINTEF wafers the values were 272 μm (281 μm) for the oxygenated (non oxygenated) wafer, respectively. Here the nominal thickness was 270 μm. The mechanical measurement also included the thicknesses of the passivation and the metallisation layers on both sides. But these areas do not contribute to the depletable volume of the sensor. Hence, for the depletion thickness calculations an estimated total passive layer thickness of 5 μm was subtracted from the measured distances.

The wafer resistivity ρ (or conductivity σ) can be obtained from

$$\rho \equiv \frac{1}{\sigma} \equiv \frac{1}{q\left(\mu_n n_0 + \mu_p p_0\right)} \approx \frac{1}{q\mu_n N_D} \quad , \tag{3.6}$$

where n_0 and p_0 are the the electron and hole concentrations, μ_n and μ_p the corresponding carrier mobilities and N_D the Donor concentration. The right approximation in equation (3.6) only holds if the minority carrier concentration (here p_0) is negligible compared to the majority concentration (here n_0). The results for d_{wafer}, V_{FD}, N_D and ρ are summarised in table 3.2. The uncertainties of the V_{FD} and d_{wafer} measurements were estimated to be about 5 %. This leads to an error of ~6 % for N_D and ρ.

Table 3.2: *Doping concentrations and resistivities of the wafers.*

	V_{FD}	d_{wafer}	N_D	ρ
CSEM	140 V	315 μm	$1.9 \cdot 10^{12}$ cm^{-3}	2.5 kΩ cm
SINTEF ox	171 V	267 μm	$3.2 \cdot 10^{12}$ cm^{-3}	1.5 kΩ cm
SINTEF non-ox	183 V	276 μm	$3.2 \cdot 10^{12}$ cm^{-3}	1.5 kΩ cm

3.3.4 Van der Pauw Measurements

With the van der Pauw method the specific resistivity of a flat sample or implant of arbitrary shape can be measured [35]. Compared to the four-point method it has the advantage that the sample can be of arbitrary shape. The only conditions that have to be fulfilled are:

① The contacts are at the circumference of the sample,

② The contacts are sufficiently small,

③ The sample is homogeneous in thickness and

④ The surface of the sample is singly connected, i. e., the sample does not have isolated holes.

If one takes a sample of arbitrary shape (e. g., like the one in figure 3.25) with successive contacts A, B, C and D - so that the conditions above are fulfilled - one can define a resistance $R_{AB,CD}$ as the potential difference $V_D - V_C$ between the contacts D and C divided by the fixed current that is sent through the contacts A and B. Similarly one can also define the resistance $R_{BC,DA}$. In [35] it is shown that then the following relation holds:

$$\exp\left(\frac{-\pi R_{AB,CD}\, d}{\rho}\right) + \exp\left(\frac{-\pi R_{BC,DA}\, d}{\rho}\right) = 1 \quad , \tag{3.7}$$

where ρ is the specific resistivity of the material and d the thickness of the sample. Equation (3.7) can be solved numerically or with the help of a graph given in [35].

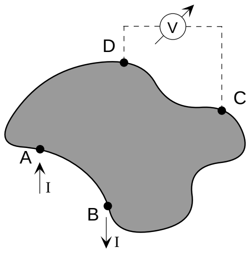

Figure 3.25: *A sample of arbitrary shape with four small contacts that can be used to measure the resistivity.*

For the CSEM wafers several van der Pauw measurements have been performed to obtain the sheet resistance $\rho_s \equiv \rho/d$ of the n^+- and p^+-implants. The applied currents varied between 0.1 mA and 10 mA. The sheet resistances were consistent for all currents and were measured to be 240 Ω/square for the p^+ implants and 20 Ω/square for the n^+ ones. The nominal values given from CSEM were 250 Ω/square (25 Ω/square) for the p^+- (n^+-) implants, respectively.

From section 2.2 it is known that the implant depth d is about 1.5 μm. Assuming an abrupt junction the average doping density in the implants can be calculated with

$$N_{implant} = \frac{1}{q\mu\rho_s d} \quad , \tag{3.8}$$

which leads to $3.6 \cdot 10^{17}\,\text{cm}^{-3}$ for the p^+- and $1.6 \cdot 10^{18}\,\text{cm}^{-3}$ for the n^+-implants (nominal $3.4 \cdot 10^{17}\,\text{cm}^{-3}$ and $1.2 \cdot 10^{18}\,\text{cm}^{-3}$).

CHAPTER

FOUR

MEASUREMENTS AND SIMULATIONS

This chapter explains the methods and results of my measurements and simulations. Section 4.1 deals with the pixel isolation and the potential of unconnected pixels. In section 4.2 the influence of different design parameters on the electric field distribution in the sensor is simulated. Section 4.3 describes the investigation of the Si-SiO_2 interface with the help of MOS-measurements. Section 4.4 dwells on the high voltage stability by looking at the break-down behaviour of different guard ring designs. The subject of section 4.5 is the inter-pixel capacitance. Section 4.6 treats the performance of bump bonded prototype sensors in a beam-test and in laboratory measurements and section 4.7 describes the measurement of the Lorentz-angle in irradiated silicon. Finally, in chapter 5 conclusions for the CMS pixel detector are drawn from all these measurements.

4.1 Pixel Isolation

The connection between sensor and read-out chip is done with the bump bond or flip chip technique. But unlike the industrial flip chip techniques, where the bumps have a diameter of $100\,\mu$m and more, the bump process used here should work with spheres smaller than $20\,\mu$m. Based on past experiences one has to assume that a small fraction of the bumps will only make a poor connection between sensor and chip[1]. A badly connected pixel not only causes a dead read-out channel, it also fails to hold the pixel at the fixed chip potential (which is close to ground). Such a pixel stays at an intermediate negative potential between V_{bias} and the chip potential. Due to charge collection the pixel can even become more negative. If the pixels

---

[1] The yield of the bump bonding process is believed to be better than 99.9 %, leading to 40'000 badly connected pixels out of 40 millions.

are completely isolated - and if the sensor is fully depleted - the badly connected pixel can charge up to a potential high enough that either a local avalanche due to impact ionisation or a local discharge through the narrow gap to the read-out chip can occur. Such phenomena were observed during tests of irradiated prototype pixel sensors with closed p-stop rings [7].

This problem might be solved by breaking the pixel isolation in a controlled way. Small openings in the p-stop rings provide a resistive path between the pixels that allows an outflow of the accumulated charge without influencing the fast signals.

Section 4.1.1 covers investigations of resistive channels. Measurements on unirradiated pixel devices are described in section 4.1.2. Section 4.1.3 contains a simulation of the bulk contribution to the inter-pixel current and section 4.1.4 deals with the pixel isolation after irradiation.

4.1.1 Measurements with Accumulation Channel Resistors

In order to approach the more complex labyrinth of the open p-stop rings measurements with accumulation channel resistors[2] were made first (see figure 4.1 for an example). The following points were of particular interest (always as a function of the bias voltage V_{bias}):

- The channel-current for a fixed potential-difference between the pixels (and with this the channel resistance),
- The potential of a floating pixel and
- The potential of the surrounding p^+ area.

Figure 4.1: *One of the accumulation channels used for the measurements in this section. The dark gray area is p^+, the light gray areas are n^+pixel implants. The white channel consists of n-material.*

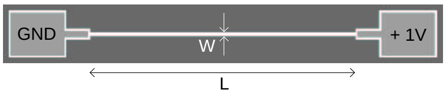

Figure 4.1 also shows the measurement principle. A potential difference of 1 V between the two pixels causes a current to flow through the channel. This current is measured as a function of the bias voltage and of the width W and the length L of the channel. All channel measurements were done with the HP 4145 B multi source meter. The channel structures have

---

[2] Resistive channels whose resistance is defined by the concentration of the electron accumulation layer.

also been processed by CSEM, but on a different batch and on high resistive silicon [36]. The full depletion voltage was 25 V which lead to a wafer resistivity of 12 kΩ cm. Figure 4.2 shows the current through a $W = 20\,\mu$m wide channel as a function of bias voltage. Three different channel lengths are plotted: $L = 200\,\mu$m, $500\,\mu$m and $800\,\mu$m. To check the geometry dependence the current was normalised as $I_{norm} = I \cdot L/W$. At voltages higher than the full depletion voltage the normalised currents are all the same, i. e., they are scaling with the channel length. Below full depletion the current does not only flow through the channel but also through the field-free part of the bulk. Therefore it is much less dependent on the channel length. Due to the normalisation with L/W the longest channel gets the highest current. The shape of the current curve before full depletion is determined by the depth of the undepleted region, which shrinks with the square-root of the increasing bias voltage[3]. Further investigations on this behaviour are made in section 4.1.3.

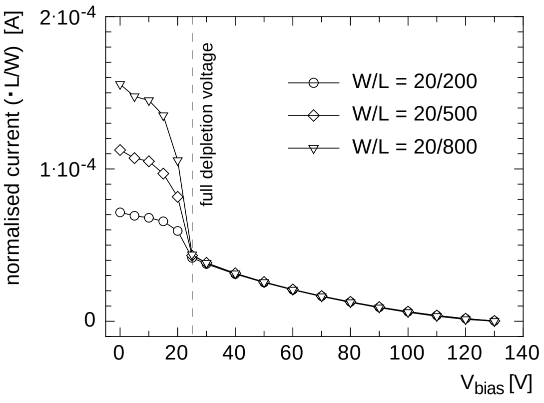

Figure 4.2: *Normalised channel current vs. V_{bias} for $200\,\mu$m, $500\,\mu$m and $800\,\mu$m long channels. The channel width was $W = 20\,\mu$m.*

It is remarkable that the current does not stay constant beyond full depletion. With the increasing bias voltage the current decreases linearly. There are surface effects that still allow the current to flow beyond full depletion. The charge accumulation layer described in section 2.3 is responsible for this behaviour. This phenomenon is only weakly dependent on the bias voltage (small slope of the current curve) and can be suppressed with high over-depletion only. Further investigations into this subject are made in sections 4.1.3 and 4.3.

The corresponding normalised resistance $R = 1\,V\,/\,I_{norm}$ is plotted in figure 4.3 for the $L = 500\,\mu$m channel. In addition the normalised resistances of a $W = 12\,\mu$m wide channel is also displayed in figure 4.3. It is striking that for voltages higher than the full depletion voltage the $12\,\mu$m channels have a higher normalised resistance than the $20\,\mu$m ones. This indicates that the channel resistance does not scale with $1/W$. Lateral depletion zones between the n-type channel and the surrounding p^+ area cut into the channel,

---

[3] See e. g., equation (C.13).

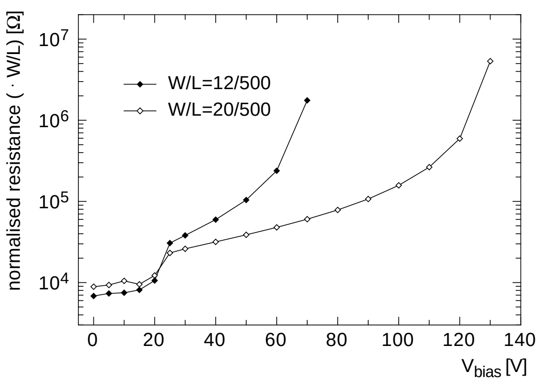

Figure 4.3: *Normalised resistance vs. V_{bias} for 20 μm and 12 μm wide channels.*

which influences narrow channels more than wide ones. Such effects are well known in MOSFET transistors and are called channel narrowing or pinch-off[4] effects.

To check the influence of this current-characteristic on a badly connected pixel I performed some measurements on floating pixels and p^+ areas of the channel-structures. These measurements were also done with devices like the one in figure 4.1, only that one of the pixels (marked with $+1\,V$ in figure 4.1) was kept floating. The potential of the p^+ implant was measured with the help of a small spy-pad, which is not shown in figure 4.1.

The left plot in figure 4.4 shows the potential of a floating pixel as a function of the bias voltage for a 20 μm wide (W) and 500 μm long (L) channel. The other pad was held at ground. The surrounding p-stop area was also floating. The floating pad stays at a very low potential for bias voltages up to about four times the full depletion voltage. Like the channel-current behaviour in figure 4.2 this effect is due to a conductive surface channel, which is only cut off at massive over-depletion. Beyond this voltage the floating pad potential rises linearly with V_{bias}.

---

[4] Pinch off is a term used in MOS-transistor physics to describe the blocking of the current through the source-drain channel by lateral depletion regions due to a reverse gate voltage (from [37]).

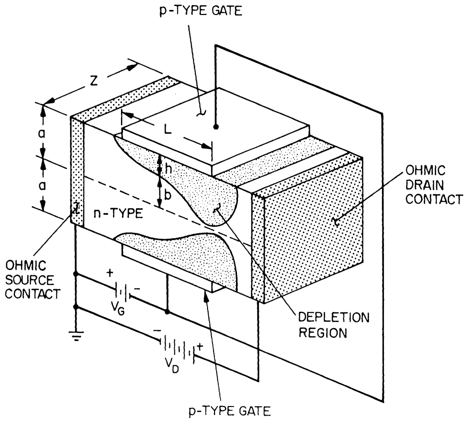

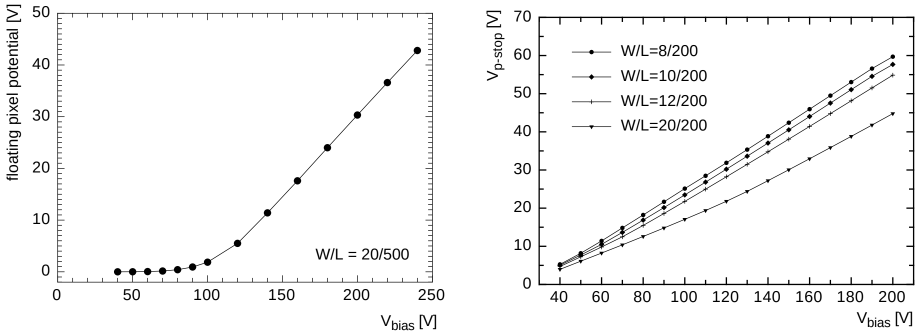

Figure 4.4: *Left: potential of the floating pixel, the other pixel was kept at ground; right: potential of the surrounding* p^+ *implant (measured with the device in figure 4.1).*

The potential of the surrounding p^+ implants (p-stop area) is displayed in the right graph of figure 4.4. Both pads were held on ground-potential. After full depletion it grows linearly with the bias voltage. As expected from figure 4.3 the slope is smaller for wider channels (pinch-off).

These measurements already show that the resistance of an accumulation channel is not only geometrically defined by its width and length, but that it also depends on the bias voltage due to pinch-off effects.

4.1.2 Measurements on Unirradiated Pixels

Unless modified by the sharp angles the resistance of the labyrinth-path in the atoll-like p-stop rings should be comparable to the channel-resistance measurements described above. However, the numerous bendings and 180° turns of that "channels" may alter their resistive behaviour.

The resistance between one pixel and all its neighbours (inter-pixel resistances) was measured with the 5×5 pixel structures shown in figure 3.5. The central pixel was at a fixed potential V_m (e. g., plus or minus 0.2 V) and all the other 24 pixels were held at ground. The bias voltage -V_{bias} was applied at the p^+ implant on the backside (therefore, the depletion zone grows from the backside). The n^+ implants at the scribe-lines were held at ground as well (on both sides of the structure). A sketch of the measurement setup is displayed in figure 4.5.

A first measurement was made to check whether the current through the central pixel really leaves the device through the surrounding pixels. The currents through the central pixel and the surrounding ones is plotted in figure 4.6 as a function of bias voltage for pixels with one open p-stop ring. The central pixel was at a potential of of -0.2 V. The vertical symmetry around $I = 0$ A of the two curves proves that the current which enters the

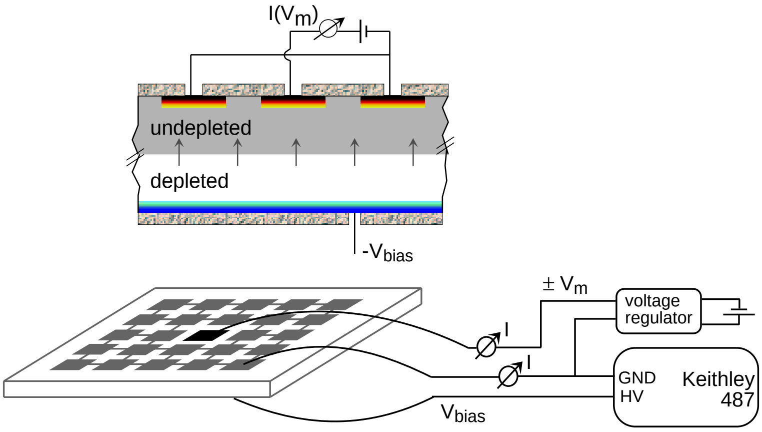

Figure 4.5: *Setup for the pixel isolation measurement, top: cross section through an unirradiated device, bottom: schematic and measurement equipment (the guard-ring area and the* n^+*implants at the scribe line are not shown).*

device through the middle pixel leaves it through the neighbouring pixels (or vice versa), and not through the backplane or the scribe-line contacts.

Figure 4.6: *The current through the central pixel and its neighbours as a function of* V_{bias}*. The small steps between 40 and 50 V are due to a range-change of the current meter.*

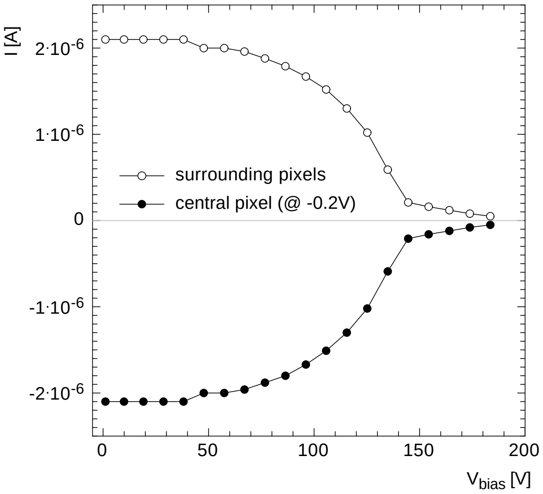

From the shape of the current curves in figure 4.6 one sees again the influence of the shrinking undepleted zone below the full depletion voltage (the decrease of the current with the square root of V_{bias} below 140 V) and the surface current which extends into the over-depletion regime and decreases only linearly with V_{bias} (similar to figure 4.2). The proof that the non-linear regime of the current is due to the bulk contributions is given in section 4.1.3. The causes for the surface current regime are explained in section 4.3.

The corresponding backplane-current through the p$^+$ implant (i. e., the total leakage current) is shown in figure 4.7. Despite of the same order of magnitude it is not influenced by the inter-pixel current. The backplane-current is rising with V_{bias} whereas the inter-pixel current is falling. This is another confirmation that the current through the central pixel is a suitable tool to measure the inter-pixel resistance.

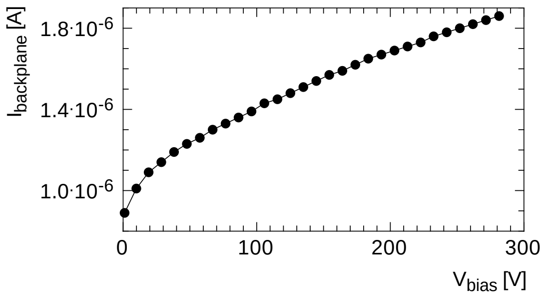

Figure 4.7: *The backplane current measurement which corresponds to the inter-pixel-current measurement in figure 4.6.*

Measuring the current through the central pixel really establishes a method which allows to reckon the resistance from one pixel to all its neighbours. But this method only works because the leakage current from the backplane to the pixels is small. Most of the leakage current in figure 4.7 flows between the backplane and the n$^+$ implants around the scribe-line. For an unirradiated sensor the leakage current per pixel is only about 15 pA at 300 V. But after proton- or pion-irradiations with 10^5 Gy the leakage current per pixel is roughly 10 nA. For 5 × 5 pixels this amounts to 0.25 μA, which is not negligible any more compared to the surface currents that flow between the pixels.

Therefore, a modification of the method was necessary. The leakage current mainly depends on V_{bias}. It is not influenced by the mid-pixel voltage V_m if V_m is smaller than the bias voltage. But the inter-pixel currents between the pixels highly depend on the potential of the central pixel. The inter-pixel current measurement was now made twice, once with a positive mid-pixel potential $+V_m$ and once with a negative one $-V_m$. The leakage current contributions cancel in the difference ΔI, which yields to an inter-pixel current measurement over a potential difference of $2V_m$. This current then translates into an inter-pixel resistance as

$$R = \frac{2V_m}{\Delta I} = \frac{2V_m}{I(-V_m) - I(+V_m)} \quad . \tag{4.1}$$

One open question still remains to be answered: is the resistance calculated from the current through the central pixel with equation (4.1) independent of its potential V_m? In this case the current difference $\Delta I = I(-V_m) - I(+V_m)$ should linearly increase with the central pixel potential V_m. Figure 4.8 shows the current difference ΔI versus V_m for different values of V_{bias}. The linearity

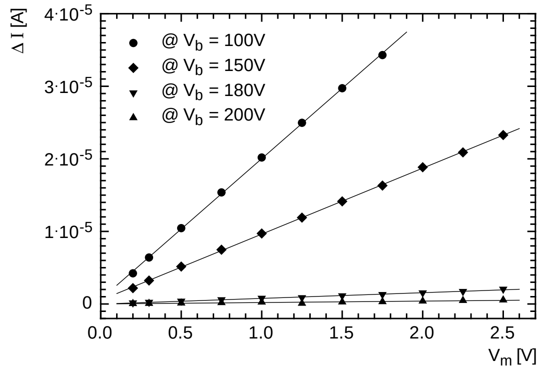

Figure 4.8: *Linearity test of the inter-pixel current difference ΔI versus the mid-pixel potential V_m.*

condition is perfectly fulfilled which proofs that R is really independent of V_m in the range from $V_m = 0\,\text{V}$ to $V_m = \pm 2.5\,\text{V}$.

4.1.2.1 Comparison of Different p-Stop Designs and Materials

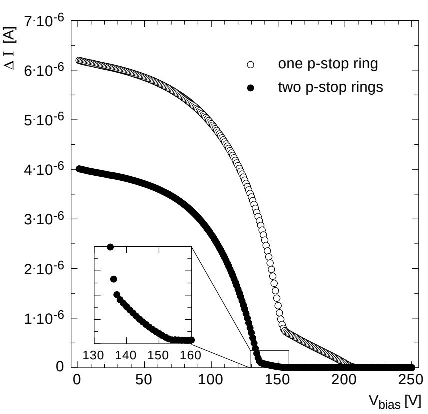

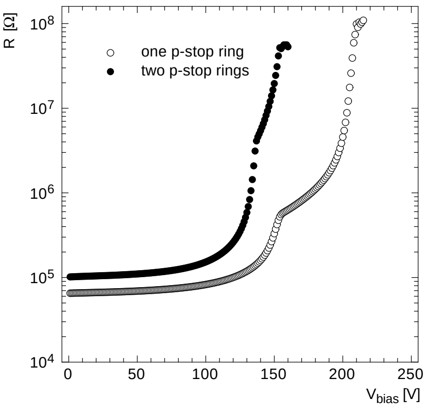

Figure 4.9: *The inter-pixel current $\Delta I(V_m = \pm 0.2\ V)$ of devices with one and two open p-stop rings.*

Figure 4.10: *The resistances obtained from the currents in figure 4.9.*

In a first step let us now compare p-stop designs with one and two open p-stop rings (see figures 3.2 and 3.3). Figures 4.9 and 4.10 show the currents ΔI and the resistances R of two CSEM devices as a function of the bias voltage. One observes first that the resistance of the device with two rings rises faster than the device with only one p-stop ring. The second observation is that the surface-current beyond full depletion decreases more slowly in the device with one p-stop ring. This behaviour is caused by the negative potential of the p-stop rings. The quite high voltage difference between the grounded n^+ implants and the p-stop rings causes pinch-off effects (see figure 4.11 and footnote 4). Small depletion zones around the p-stops hinder the current to flow through the p-stop labyrinth between the pixels. The surface current is cut off at a smaller bias voltage in the devices with two p-rings per pixel due to the smaller distance between the p-stop rings. The width of the gap between the p-stop rings was 22 μm for the device with one p-stop ring and 8 μm for the one with two rings.

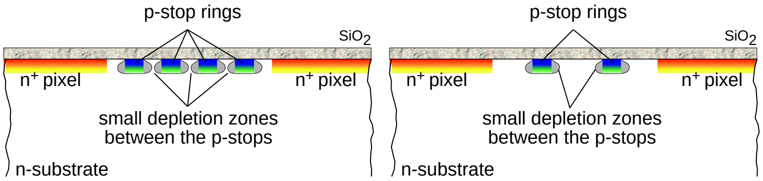

Figure 4.11: *Left: pinching-off of the conductive labyrinth between pixels with two p-stops due to small lateral depletion zones between the p-stops. Right: a similar situation for pixels with only one p-stop ring per pixel.*

Similar resistance plots are shown for two different SINTEF devices in figures 4.12 and 4.13. Both of them had only one p-stop ring. One consisted of oxygen-enriched silicon (ox), the other one had a normal oxygen concentration (non-ox). To facilitate the comparison between SINTEF and CSEM the current and the resistance of the CSEM device with one p-ring from figures 4.9 and 4.10 are also plotted. For the SINTEF devices no surface current regime seems to exist. Neither the oxygen-enriched nor the non-oxygenated structure show any signs of significantly contributing surface currents. This is due to differences in the production process between SINTEF and CSEM. As discussed in section 4.3 the SINTEF oxides contain much less trapped charges (Q_{ox}), which are responsible for the electron surface accumulation layer. Obviously, the oxide charge concentration Q_{ox} (and hence the concentration in the surface accumulation layer) is too low to establish surface currents in the SINTEF case. For the oxygenated device in figure 4.13 the maximum resistance is reached at a lower bias voltage than for the non-oxygenated one. Oxygenation therefore appears to lower the surface conductivity. But this difference turned out to be negligible after low doses of irradiation as it is explained in section 4.1.4.

To clarify whether the inter-pixel resistance is mainly dominated by the distance between the p-stop rings some measurements with varying gaps between the p-rings have been made (all with double p-stop rings, similar to figure 3.2). The resulting inter-pixel resistances are plotted in figure 4.14. The kink which denotes the change from the bulk current regime to the surface regime is clearly shifted to higher voltages for wider gaps. And furthermore, the surface current regime spans a larger voltage interval for wider gaps. The distance between the p-stop rings definitely influences the pixel-isolation.

The inter-pixel resistance for structures with cross-like p-stop rings (see

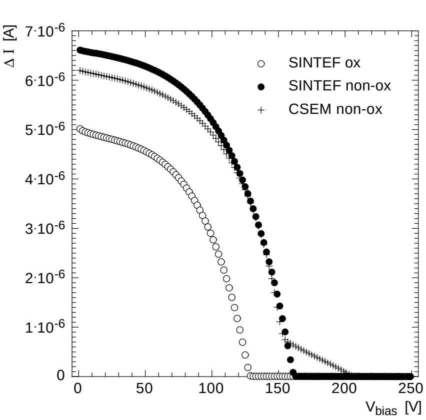

Figure 4.12: The pixel current ΔI for SINTEF devices with one p-stop ring per pixel, for oxygenated- (ox) and non-oxygenated (non-ox) silicon. As a comparison the corresponding CSEM current is also plotted.

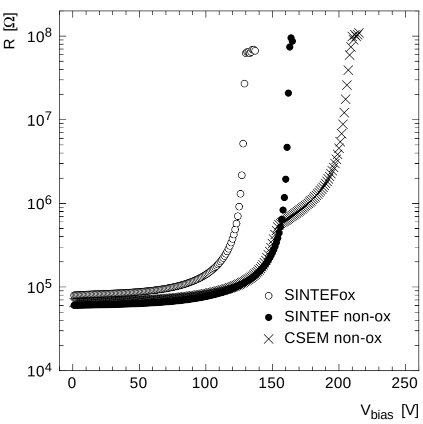

Figure 4.13: The resistances for the same devices as in figure 4.12.

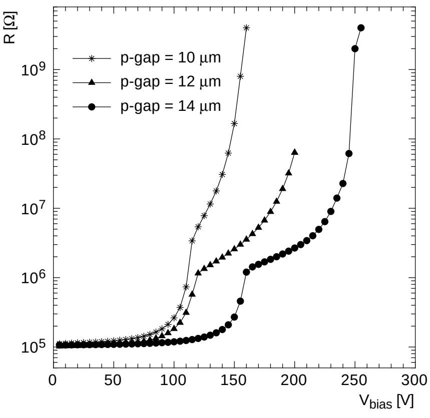

Figure 4.14: Inter-pixel resistances for devices with 10, 12 and 14 μm gaps between the p-stop rings.

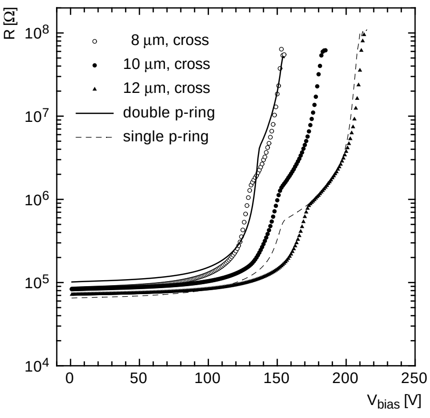

Figure 4.15: Pixel isolation for cross-pstop rings with different p-stop gaps (figure 3.4) compared to double and single rings (from figure 4.10).

figure 3.4) is compared to single and double p-stop rings (from figure 4.10) in figure 4.15. All of them were processed by CSEM. The "cross-p-stops" had gaps of 8, 10 and 12 μm. The gap between the double p-stops was 8 μm and the one between the single p-stop rings 22 μm. The channel lengths from one pixel to another were in the order of 300 μm for the cross-structures, 150 μm for the single p-stop and 450 μm for the double p-stop ring. These channel lengths do not seem to influence the pixel isolation. The cross-structure with a 8 μm gap and the double p-stop ring have similar resistances. The same is true for the single p-stop ring and the cross p-stop with a 12 μm gap. But again there are distinct differences between the devices with diverse p-gap widths.

Let us **summarise** the results achieved so far:

- ➢ The inter-pixel resistance of **unirradiated** sensors with open, atoll-like p-stop rings is mainly dominated by the gap between the p-stop rings, due to pinch-off effects (i. e., smaller resistances for wider gaps). The length of the labyrinth-like conductive channel between the pixels is of much less importance.
- ➢ For bias voltages in the order of the full depletion voltage V_{FD} one single pixel is isolated from its neighbours with a few MΩ.
- ➢ Depending on the production process (i. e., on the oxide quality) there is a surface current regime already before irradiation. There are indications that oxygen enriched silicon has a slightly higher inter-pixel resistance than silicon with normal oxygen concentrations.

4.1.3 Simulation of the Bulk Contributions

In this section a proof is given that the inter-pixel currents ΔI really contain a bulk and a surface contribution. In order to separate these two parts a SPICE [38] simulation of a three dimensional resistive network was performed. Its purpose was to simulate the inter-pixel current through the undepleted (and hence conductive) bulk-region of a sensor as a function of the bias voltage[5].

The resistive network consisted of cells with three resistors in x- y- and z-direction which represented an elementary cube of undepleted silicon. Each cube corresponded to one SPICE node[6]. The resolution (cube size) was mainly determined by the available computing power. An initial resolution of 30 μm was chosen to simulate an area of 5 × 5 pixel (750 × 750 μm^2 surface area). The resistivity of the silicon bulk could be extracted from the full depletion voltage V_{FD}. The value of V_{FD} was determined with a C-V measurement of a gated diode (see section 3.3). For the CSEM wafers it was measured to be 140 V which leads with equation (2.2) to a resistivity of $\rho = 2.5\,\text{k}\Omega\,\text{cm}$.

A cube of $\ell = 30\,\mu\text{m}$ side length then corresponds to a resistance of

$$R_{cube} = \frac{\rho \ell}{\ell^2} = 0.83\,\text{M}\Omega \quad . \tag{4.2}$$

---

[5] Since in a unirradiated sensor the depletion zone grows from the backside the undepleted region under the pixels becomes smaller and smaller with increasing bias voltage.

[6] A point in a circuit where several lines or component-connections come together.

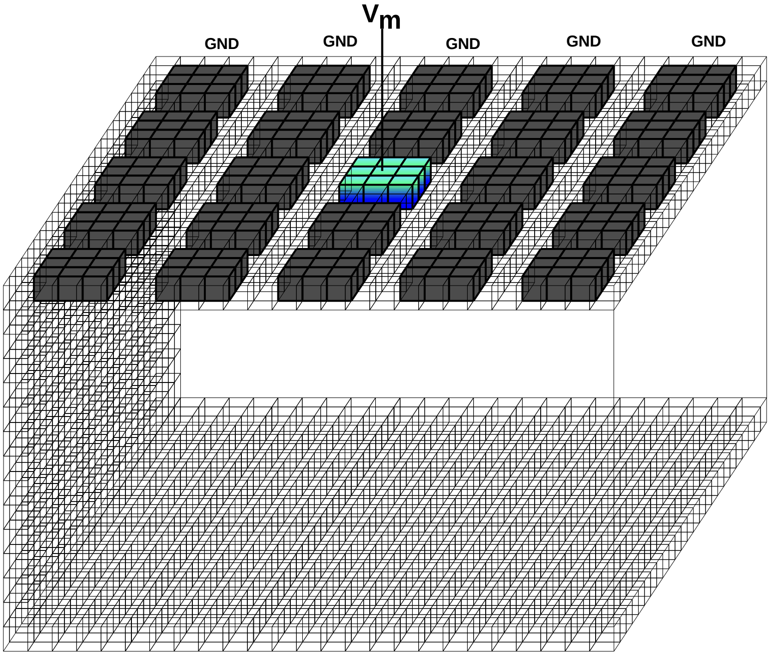

Figure 4.16: *SPICE cube network: each pixel was simulated by an area of* 5×5 *cubes. The depth was variable. Each cube represents a SPICE node. The top* 3×3 *inner cubes of each pixel were connected to a potential (*V_m *for the innermost pixel, indicated in light gray, GND for all the others (dark gray)).*

Hence, each of the 25 pixels ($150 \times 150\,\mu\mathrm{m}^2$) consisted of the following number of elementary cubes (nodes)

$$N = \left(\frac{150\,\mu\mathrm{m}}{30\,\mu\mathrm{m}}\right)^2 \cdot \left(\frac{\mathrm{depth}}{30\,\mu\mathrm{m}}\right) \quad , \tag{4.3}$$

which were connected in x- y- and z-direction by $0.83\,\mathrm{M}\Omega$ resistors. The inner 3×3 nodes of each pixel were held at a fixed potential (V_m for the innermost pixel, ground for the other ones), the rest of the nodes were floating (see figure 4.16).

The vertical resolution is of crucial importance in order to reproduce the measured bulk behaviour. First a two dimensional $x - z$ test-simulation was performed to study the influence of changes in the vertical resolution. Therefore the number of nodes in vertical direction was increased and the value of the vertical resistors was decreased accordingly. E. g. if one resistor represented a vertical dimension of $15\,\mu\mathrm{m}$ (instead of $30\,\mu\mathrm{m}$) its value was divided by two. At the same time the horizontal resistors had to be increased by a factor of two, since the horizontal resolution had to be kept at $30\,\mu\mathrm{m}$.

The resulting two-dimensional current through the mid-pixel at $V_m = 0.2\,\mathrm{V}$ is plotted in figure 4.17 as a function of the number of vertical nodes (nodesz). The simulation depth was $300\,\mu\mathrm{m}$ for all points. Beyond roughly

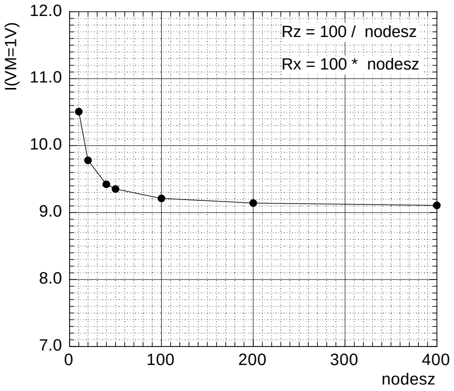

Figure 4.17: *Two-dimensional test simulation to determine the dependence of the pixel current on the number of vertical nodes.*

100 vertical nodes the simulated current remains almost constant. This corresponds to a vertical resolution of 3 μm.

Since the available computing memory did not allow a three-dimensional simulation of the full 300 μm deep device with a maximal vertical resolution of 3 μm it was fist run with a lower resolutions (30 μm $\triangleq$ 10 vertical nodes and 15 μm $\triangleq$ 20 vertical nodes). The vertical resolution was then increased for smaller depths of the undepleted zone (down to a vertical resolution of 3 μm).

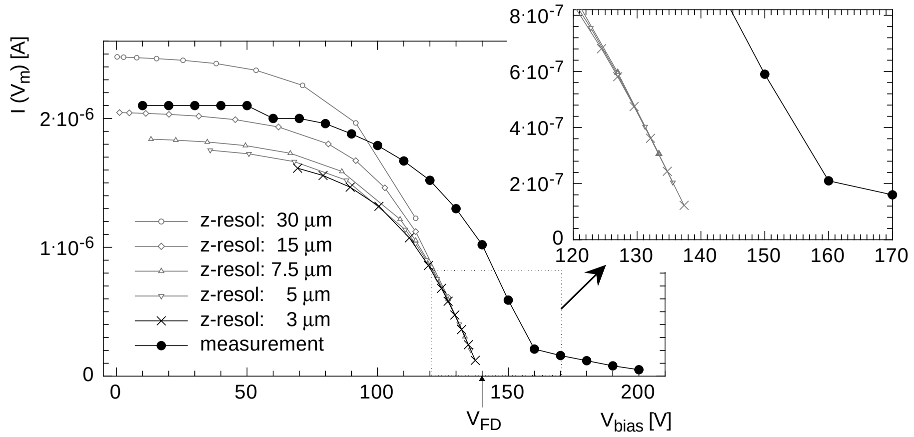

Figure 4.18: *The simulated inter-pixel currents through the bulk for different vertical resolutions together with a measured curve from a device with one open p-stop ring (ignoring surface currents). The input parameters for the simulations were V_{FD} = 140 V (measured) and V_m = 0.2 V.*

Figure 4.18 shows the results of the 3D-simulation. The simulated current through the central pixel at V_m =0.2 V is plotted versus the bias voltage. In addition, a measurement on a CSEM device with one open p-stop ring (see e. g., figure 3.3) is also shown. The shape of the lower resolution simulations (zresol = 7.5 μm and below) is in very good agreement with the measurement. They are only slightly shifted along the voltage axis. This is due to the surface currents which still flow after full depletion and which were not included in the simulation. It has to be emphasised that these results have not been adapted to the measured curve in any way (the simulation had no free parameter). The only input parameter was V_{FD}, which was extracted from a measurement. This result clearly shows that the measured current below the kink at 160 V is a result of the current flow through the bulk and along the surface whereas the current above the kink is determined by surface effects only.

4.1.4 Measurements on Irradiated Pixels

Pixel sensors similar to the ones described in the last section have been irradiated with pions and protons. The proton irradiations were done at CERN with the RD48 (ROSE) irradiation facility, which uses the PS accelerator with 24 GeV/c protons. The first irradiation could be done with a flux of $8 \cdot 10^{10}\,\mathrm{p\,cm^{-2}\,s^{-1}}$ leading to $6 \cdot 10^{14}\,\mathrm{p\,cm^{-2}}$ in about 20 hours. For the other proton irradiations the flux varied between 2 and $9 \cdot 10^{9}\,\mathrm{p\,cm^{-2}\,s^{-1}}$. Pion irradiations were done at PSI in the experimental area π-E1 with 300 MeV/c pions and a flux of $3.2 \cdot 10^{9}\,\pi\,\mathrm{cm^{-2}\,s^{-1}}$. The total irradiation period lastet about 15 days, since it was interrupted many times to perform measurements on the test devices. The effective integrated irradiation time was about 60 hours. During the beam time the sensors were at room temperature, the rest of the time and after the irradiation they were kept at +1°C to slow down annealing effects.

The determination of the flux was made with the help of thin aluminium foils. During the irradiation of aluminium with pions or protons ^{24}Na-nuclides are produced with a well known cross section. They decay by β^- emission with a half life of 15 h and associated γ energies of 1369 keV and 2754 keV. By counting these γs the original flux of particles can be calculated with an accuracy of about 6 % [39].

To ensure realistic electric field conditions the sensors were kept biased during the irradiation. This required a small double-sided *PCB*[7] where the sensors could be embedded in epoxy and bonded to solder pads. These *PCB*s were highly activated during the irradiation. A few hours after the end of the pion irradiation the small boards showed an averaged dose rate of 200 $\mu\mathrm{Sv\,h^{-1}}$. The mostly short-lived isotopes decayed with a measured half life of 26 h. After a few weeks the activity had fallen to a value that allowed a save handling of the devices. At that point the main activity came from ^{7}Be with a half life time of 54 days (250 Bq after 50 days which corresponds to an equivalent dose rate $\leq 0.25\,\mu\mathrm{Sv\,h^{-1}}$ at a distance of 10 cm [40]).

---

[7] Printed circuit board.

4.1.4.1 Low Dose Irradiations

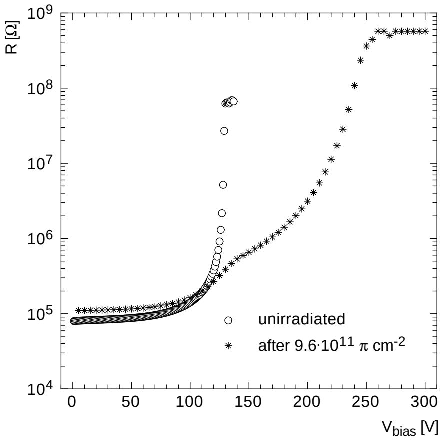

Figure 4.19: *The inter-pixel resistance for a oxygenated device with one p-ring before irradiation and after $9.6 \cdot 10^{11}\,\pi\,cm^{-2}$.*

In section 4.1.2 it was found that the oxygenated device lacks a surface current regime before irradiation. This was put down to the low oxygen charge concentration Q_{ox} in the oxygenated SINTEF device. With low dose irradiations it can be shown that this assumption was right. After the introduction of some oxide charges with a low dose pion-irradiation (below type inversion, $\Phi = 9.6 \cdot 10^{11}\,\pi\,\text{cm}^{-2}$, $300\,\text{MeV}/c$) the surface current regime appears also in the SINTEF device (see figure 4.19). Therefore, the different inter-pixel resistances of the oxygenated SINTEF and the non-oxygenated CSEM devices were due to differences in the production process of these two vendors and not due to the higher oxygen concentration itself. This conclusion is also confirmed by the MOS-measurements in section 4.3. As it is shown in section 4.1.4.4 the oxygenated SINTEF devices have even a slightly lower resistance than the non-oxygenated CSEM ones after high irradiation doses.

4.1.4.2 High Dose Irradiations

The inter-pixel resistances after high dose irradiation were measured with the method described on page 53. To compensate for the higher leakage current a potential of $V_m = \pm 2.0V$ was applied on the centre pixel (instead of $\pm 0.2\,V$). A sketch of the cross section through an irradiated sensor showing the measurement setup is displayed in figure 4.20. Note, that due to the type inversion the depletion layer now grows from the pixel side (see also figure 4.5).

On page 23 the *NIEL*-factor was introduced. It was already mentioned that above roughly 100 MeV the *NIEL*-factors for protons and pions are comparable [22, 41]. Therefore, we can assume that the changes in the inter-pixel resistance caused by pions and protons are about the same. This assumption is confirmed by my measurements. In figure 4.21 the resistance R is plotted

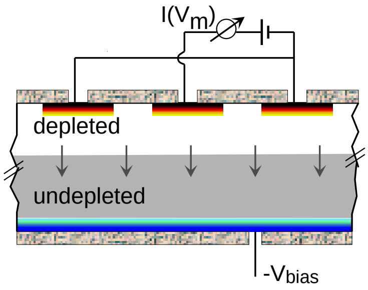

Figure 4.20: *Cross section through an irradiated sensor and the measurement electrodes.*

after $6 \cdot 10^{14}$ pions and protons per cm^2. As a comparison the inter-pixel resistance curve of an irradiated sensor with double p-stop rings is also shown. The difference between the double p-ring device and the single p-ring sensors is much more pronounced than the difference between proton and pion irradiations. Therefore, the same irradiation-damage model can be applied to proton- and pion irradiations.

The CERN-PS protons had a much higher energy (24 GeV) than the PSI pions (300 MeV). Due to the energy dependence of the *NIEL*-factor the two cases should be treated separately. But the available simulation-data are still not conclusive enough to justify an exact quantitative distinction of the two cases with respect to the *NIEL*-factor. The difference between them lies in the order of 20%, which is less than the model-uncertainties. Therefore, I assumed that the PSI-pions and the CERN-protons have the same *NIEL*-factor for the further analysis.

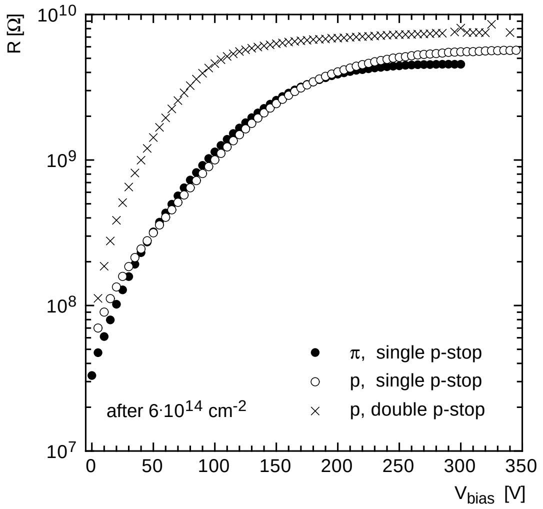

Figure 4.21: *Inter-Pixel resistance of a single p-ring sensor after pion and proton irradiation. As a comparison the resistance of a double p-ring device is also shown.*

For the CMS pixel detector the average *NIEL*-factor was calculated to be about 0.7 [4]. With the radiation simulation package FLUKA [42] it can be estimated that a dose of $\mathcal{D} = 10^5$ Gy corresponds to $\sim 3 \cdot 10^{14}\,\pi\,\mathrm{cm}^{-2}$ in the

LHC environment[8] [4]. Assuming that LHC does not reach its full design luminosity of $10^{34}\,\mathrm{cm}^{-2}\,\mathrm{s}^{-1}$ in the first year this fluence will be obtained after about $3-4$ years of operation in the innermost layer. The dose of 10^5 Gy is the operational limit of the read-out chips. Hence, after $3-4$ years the modules will have to be replaced. For the prototype sensor tests a safety factor of two was assumed which leads to a canonical irradiation fluence of $\Phi = 6 \cdot 10^{14}\,\mathrm{cm}^{-2}$.

As outlined in section 2.3 the n-type bulk silicon changes its behaviour with irradiation. Some of the crystal defects or defect-clusters act like acceptor-ions (they trap electrons rather than holes). Since acceptor-states compensate the donor atoms the effective doping concentration $N_{\mathit{eff}} = |N_D - N_A|$ also changes with irradiation. The effective doping concentration of an originally n-type bulk decreases with irradiation until it is fully compensated (type-inversion point), after which the sensor behaves as it would be p-type doped. The full depletion voltage V_{FD} follows this behaviour with (after equation (2.7))

$$V_{FD} = \frac{q N_{\mathit{eff}}\, d_{\mathit{wafer}}}{2\varepsilon_{si}\varepsilon_{o}} \quad . \tag{4.4}$$

The built in voltage of the p-n junction was neglected in equation (4.4), since it is normally much lower than the depletion voltage.

4.1.4.3 Determination of the Type Inversion Fluence

After type inversion the depletion zone grows from the front-side (the pixel-side). The p-n junction then occurs at the pixel-side between the n$^+$ pixel implants and the inverted bulk. The area between the pixels is already depleted even at quite low values of V_{bias}. This causes the dependence of the inter-pixel resistance on V_{bias} curves to change dramatically compared to the unirradiated case. Figure 4.22 shows a few resistance curves just before and after type inversion of a CSEM pixel sensor with single p-stop rings (figure 3.3), which was irradiated with pions. After type inversion there is no flat resistance regime any more at low voltages as there is no undepleted zone below the pixels[9], and the charge flows as a surface current only. Therefore, the inter-pixel resistance sharply rises to high values already at moderate bias voltages (compare with figure 4.10).

The regime for which the resistance is almost independent of V_{bias} before type inversion (figure 4.22) spans a smaller and smaller voltage interval the closer we come to type inversion. This fact can be used to estimate the type-inversion fluence of the devices. The fluence for which the "kink bias

---

[8] For the innermost layer at 4cm and with $E_\pi \leq 1\,\mathrm{GeV}$.

[9] Between the n$^+$ implants remains a wedge-shaped zone of low electric field-strength which disappears at massive over-depletion only (see sections 4.2 and 4.7 and reference [7]), however, the current flow is restricted by the local potential of the p-stop rings.

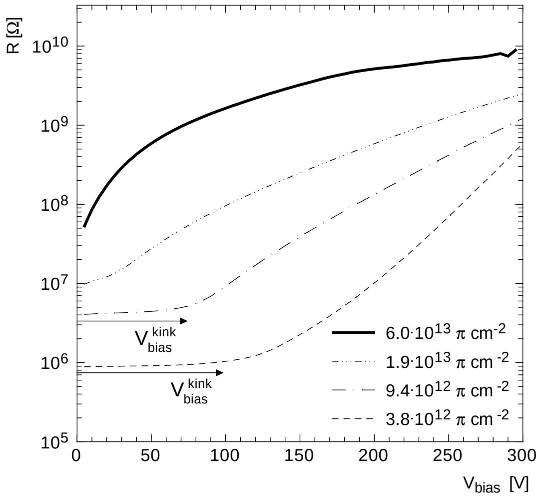

Figure 4.22: *Change of the inter-pixel resistance due to type inversion; dotted curves: for various fluences before type inversion; full, thick line: after type inversion (CSEM device with one open p-stop ring).*

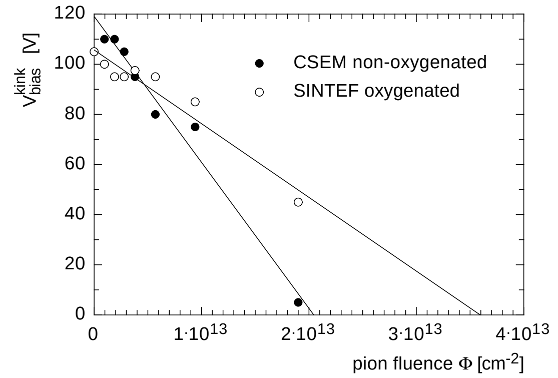

Figure 4.23: *"Kink bias voltage" V_{bias}^{kink} versus fluence. The straight lines show linear extrapolations to $V_{bias}^{kink} = 0\,V$ (type inversion fluence).*

voltage" $V_{bias}^{kink} = 0\,\mathrm{V}$ (i. e., where the linear regime ceases to exist) corresponds to the type-inversion fluence. In figure 4.23 this "kink-voltage" V_{bias}^{kink} is plotted versus the pion-fluence Φ for an oxygenated SINTEF sensor and a standard CSEM device. The lines are linear fits to the data to extrapolate to the value $\Phi(V_{bias}^{kink} = 0\,\mathrm{V})$. The type inversion fluences obtained from the extrapolations are:

$$\text{CSEM:} \qquad \Phi_{inversion} = 2.1 \cdot 10^{13}\pi\ \mathrm{cm}^{-2} \tag{4.5}$$

$$\text{SINTEF:} \qquad \Phi_{inversion} = 3.6 \cdot 10^{13}\pi\ \mathrm{cm}^{-2} \quad , \tag{4.6}$$

with an estimated uncertainty of about 10%. These values are in accordance with measurements using other, more precise methods, performed by the RD 48 collaboration at CERN [20]. The non-oxygenated CSEM device reaches $V_{bias}^{kink} = 0\,\mathrm{V}$ at a lower fluence than the oxygenated SINTEF one. This is due to combination of the different initial doping concentrations of the two devices and the oxygen enrichment. Unfortunately, these two contributions cannot be disentangled.

4.1.4.4 Comparison of Different p-Stop Designs and Materials after High Fluences

The measured currents through the mid-pixel at $V_m = 2.0\,\mathrm{V}$ are shown in figure 4.24 versus V_{bias} (for the design with a single p-stop ring and an additional cross at the pixel corners, see figure 3.4). The corresponding resistance, calculated with equation (4.1), is also given. For $V_{bias} > 140\,\mathrm{V}$ the resistance becomes independent of the bias voltage. The subsequent measurement were therefore only carried out for bias voltages up to 300 V. Unless mentioned otherwise the measurements were performed directly after the irradiation or after a few days storage at low temperatures (below 0°C).

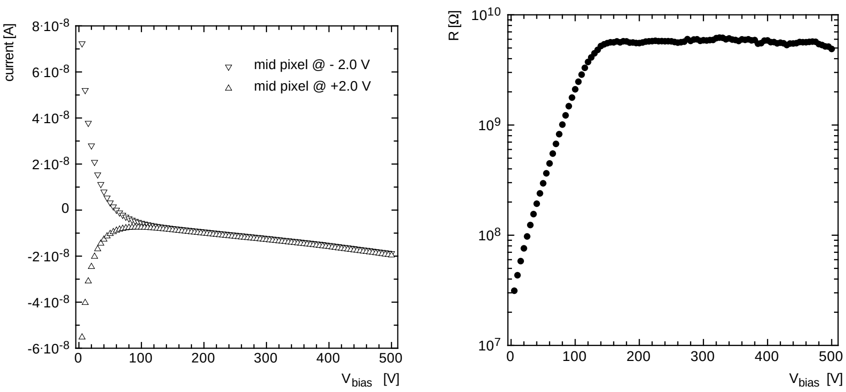

Figure 4.24: *Left: typical mid-pixel currents for $V_m = \pm 2.0\,V$ of an irradiated device; right: inter-pixel resistance calculated from these currents with equation (4.1).*

The inter-pixel resistances of three different designs are plotted in figure 4.25. The double p-stop design is shown in figure 3.2 (with a $8\,\mu\mathrm{m}$ gap between the p-stops), the single p-stop ring device in figure 3.3 (gap $22\,\mu\mathrm{m}$) and the single+cross p-stop device in figure 3.4 (all from CSEM). The applied fluence was $5.8 \cdot 10^{14}\,\mathrm{p\,cm^{-2}}$ and the devices were annealed for 10 weeks at +1°C.

After reaching the plateau value there is no difference between the resistances of the single and and the single+cross p-stop. The resistance of the double p-stop is slightly higher. But this difference is within the measurement uncertainty. Therefore, the inter-pixel resistance at high values of V_{bias} does not significantly depend on the design. Only the rising-slope varies between the different designs.

At high bias voltages the resistance reaches several GΩ and remains constant. Before irradiation the inter-pixel resistance was much lower for under-depleted sensors (a few hundred kΩ), rising exponentially with increasing V_{bias} (see e. g., figure 4.10). One would expect a smaller resistance after irradiation due to the accumulation of mobile charges at the surface. This turned out to be wrong: the pinch off effect and (to a smaller extent) the sur-

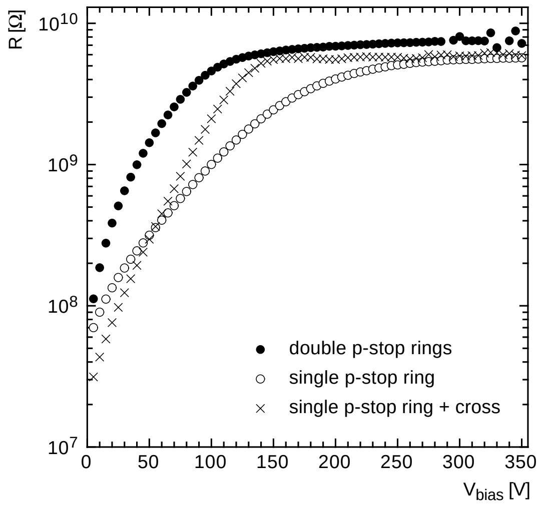

Figure 4.25: *Inter-pixel resistance versus bias voltage for different design variations after irradiation with $10^{14}\,\pi\,cm^{-2}$. All devices were from CSEM.*

face mobility reduction over-compensate for the higher accumulation layer concentration. Surface damages (e. g., surface traps due to dangling bonds or displaced atoms) reduce the surface mobility μ_S. The latter is related to the change of the interface defect density ΔD_{it} by (see e. g., [10, 19, 43])

$$\mu_S = \frac{\mu_{S_0}}{1 + \kappa(\Delta D_{it})} \quad , \tag{4.7}$$

where μ_{S_0} denotes the pre-irradiation surface mobility and κ is equal to $(8 \pm 2) \cdot 10^{-13}\,\text{cm}^2$ [19]. A method to measure the interface defect density D_{it} with MOS-capacitors is described in section 4.3.

The next measurements deal with oxygenated devices. It is not clear whether the oxygenation influences the surface properties of a sensor after irradiation. Furthermore, do surface defects show any annealing effects (beneficial or reversal) around 0°C?

In figure 4.26 R is plotted for an oxygenated (SINTEF) and a non-oxygenated (CSEM) pixel sensor with double p-stop rings (both had a gap of $8\,\mu$m between the p^+ implants, see figure 3.2). They were irradiated with $1.8 \cdot 10^{14}\,\pi\,\text{cm}^{-2}$. As a comparison the resistance-curves for the unirradiated devices from figure 4.13 are also given. Before irradiation the oxygenated device had a higher resistance than the non-oxygenated one. This is reversed after irradiation, the oxygenated device having a now a slightly lower resistance than the non-oxygenated one. Since we had only very few oxygenated sensors no systematic investigation of this question could be made. The different behaviour after irradiation could well be due to differences between the SINTEF- and CSEM-manufacturing processes. The inter-pixel resistance of sensors with only one p-stop ring is shown in figure 4.27. The irradiated samples were exposed to a fluence of $\Phi = 6.5 \cdot 10^{14}\,\pi\,\text{cm}^{-2}$. At high voltages these devices show the same behaviour as the ones with two p-stop rings after irradiation.

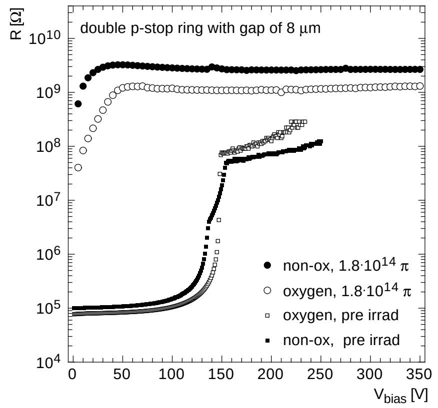

Figure 4.26: *Inter-pixel resistance of oxygenated and non-oxygenated double p-stop sensors before and after irradiation.*

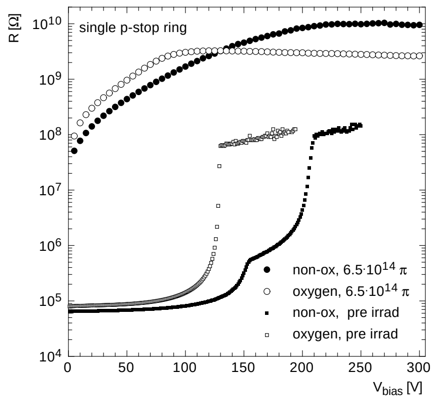

Figure 4.27: *The same plots as in figure 4.26 for a device with one p-stop ring.*

The annealing-behaviour of an irradiated sensor is addressed in figure 4.28. The device under test was an oxygenated sensor with one p-stop ring. The applied fluence was again $6.5 \cdot 10^{14}\,\pi\,\mathrm{cm}^{-2}$. After irradiation the devices were stored at a temperature of +1°C (the tracker part of CMS is operated at a temperature of −10°C. But during the maintenance periods it will be warmed to room temperature. Therefore an averaged value of 1°C was chosen for our annealing studies). The plateau-value of the inter-pixel resistance does not change with time at this temperature (no annealing effect). However, the longer the device is annealed the earlier (i. e., at a lower bias voltage) it reaches the resistance-plateau. Most probably this is due to the beneficial bulk-annealing (see on page 26).

As a **recapitulation** of this subsection the following can be stated:

- **After irradiation** the inter-pixel currents are pinched off at much lower bias voltages than before irradiation. Moreover, the inter-pixel resistance is much higher than before irradiation (several GΩ).

- The resistance is not much design dependent any more. There are minor, but not significant differences between the oxygenated and the non-oxygenated sensors: After irradiation the oxygenated SINTEF devices had a slightly lower inter-pixel resistance than the non-oxygenated CSEM ones.

- At reasonable high bias voltages and at a temperature of 1°C the inter-pixel resistance did not show any annealing effects.

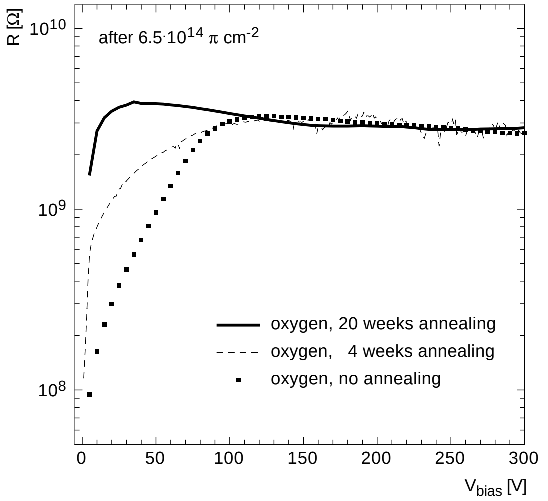

Figure 4.28: *Annealing behaviour of an oxygenated pixel sensor with one open p-stop ring.*

4.1.4.5 Pixel Isolation as a Function of Fluence

A dedicated measurement was performed to clarify whether the high inter-pixel resistances occur only at very high doses. The inter-pixel resistance was investigated as a function of fluence and bias voltage. In a first approach I tried to determine the resistance by measuring the current through the central pixel (at potential V_m) during the irradiation. This current consists of a leakage current and a surface current which flows between the pixels. The radiation induced increase of the leakage current is proportional to the applied fluence, $\Delta I_{vol} = \alpha\Phi(t)$, with α being the current related damage constant [20]. Unfortunately, the sensor could not be kept at full depletion, especially at higher fluences (due to thermal run-away[10]). This influenced the active volume which contributed to the leakage current. Furthermore, the device heated up during irradiation which strongly influenced the damage constant α. For these reasons the leakage current and inter-pixel current could not be disentangled.

Instead, the irradiation was done in short intervals, after which the device under test was cooled in the lab to $-1°C$ and measured with the method described on page 53. A mid-pixel potential $V_m = \pm 2.0\,V$ was chosen to guarantee measurable currents despite of the high resistances at higher doses and to compensate for the increased leakage current. The complete irradiation with all interruptions lasted over 300 hours.

One of the devices under test was an oxygenated SINTEF sensor and the other a standard one from CSEM. Both had single, open p-stop rings (see fig-

---

[10] In thermal run-away a high power dissipation heats up the device to a point where the semiconductor becomes intrinsic. Consequently, the majority carrier concentration in the conduction band increases, causing an increase of the leakage current. This, in turn, causes another increases in temperature, leading to a vicious cycle.

ure 3.3). The irradiations were done with pions. In figure 4.29 the inter-pixel resistances for all doses are plotted separately for the oxygenated and the non-oxygenated device. Curves for fluences below type-inversion are drawn as solid lines, the ones beyond type-inversion are dashed. The measurements after 4 and 20 weeks annealing are also shown.

From the plots in figure 4.29 one can derive the fluence-dependence of the inter-pixel resistance for a given bias voltage (see figure 4.30). For the non-oxygenated device the resistance grows with fluence up to $\sim 10^{10}\,\Omega$ until $\Phi \approx 10^{14}\,\mathrm{cm}^{-2}$ (almost linearly for $V_{bias} < 300\,\mathrm{V}$). For even higher fluences the resistance slightly decreases to a few $10^{9}\,\Omega$ at $\Phi = 6 \cdot 10^{14}\,\mathrm{cm}^{-2}$. For the oxygen-enriched device the behaviour is a bit different. Here, the inter-pixel resistance decreases for low doses (at least for $V_{bias} < 300\,\mathrm{V}$) and steeply rises for $\Phi > 10^{13}\,\mathrm{cm}^{-2}$ reaching a maximum at $\Phi \approx 1.5 \cdot 10^{14}\,\mathrm{cm}^{-2}$ (also $\sim 10^{10}\ \Omega$). At $2 \cdot 10^{14}\,\mathrm{cm}^{-2}$ R falls to $3 \cdot 10^{9}\,\Omega$ and remains constant up to $\Phi = 6 \cdot 10^{14}\,\mathrm{cm}^{-2}$. Additional 20 weeks annealing at +1°C do not significantly change the inter-pixel resistances. Moreover, both sensors had about the same R value after $6 \cdot 10^{14}\,\pi\,\mathrm{cm}^{-2}$ and 20 weeks annealing at +1 degC:

$$R \approx 3.5 \cdot 10^{9}\,\Omega \quad . \tag{4.8}$$

The differences at low fluences between the oxygenated SINTEF sensor and the non-oxygenated CSEM could lie in the higher oxide quality of the SINTEF device before irradiation (see section 4.3). The low oxide charge concentration in the SINTEF sensor before irradiation also causes a low electron accumulation concentration between the pixels. At low doses the oxide charge concentration increases until it reaches a saturation value. Conversely, this process increases the electron concentration in the accumulation layer, which in turn augments the surface mobility. In the non-oxygenated CSEM sensor the electron concentration in the accumulation layer is already so high before irradiation that a further increase does not significantly change the surface mobility. After $\Phi \approx 1 \cdot 10^{13}\,\mathrm{cm}^{-2}$ ($3 \cdot 10^{12}\,\mathrm{cm}^{-2}$) in the SINTEF (CSEM) device the surface crystal defects causing trapping centres become dominant and lead to an increase of the resistance.

4.1.4.6 Potential of p-Stops and Unbonded Pixels

From the previous isolation-measurements alone it is not easy to predict whether the high inter-pixel resistance after irradiation will lead to a destructive charging of badly bonded pixels. Since the theory of avalanche creations in semiconductors is very complicated and highly dependent on geometry and doping of the implants, it is difficult to predict the potential at which an unbonded pixel starts to break through. This subject has therefore to be studied experimentally. The 5×5 pixel arrays shown in figure 3.5 were used for that purpose.

On a unirradiated device with double p-stop rings an unbonded pixel reached approximately 80 V at $V_{bias} = 500\,\mathrm{V}$. For an irradiated device the potential

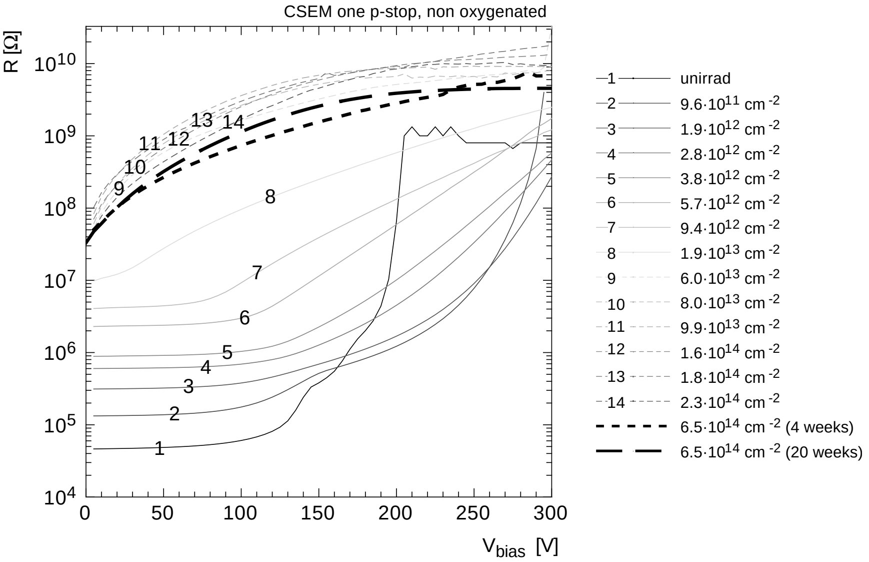

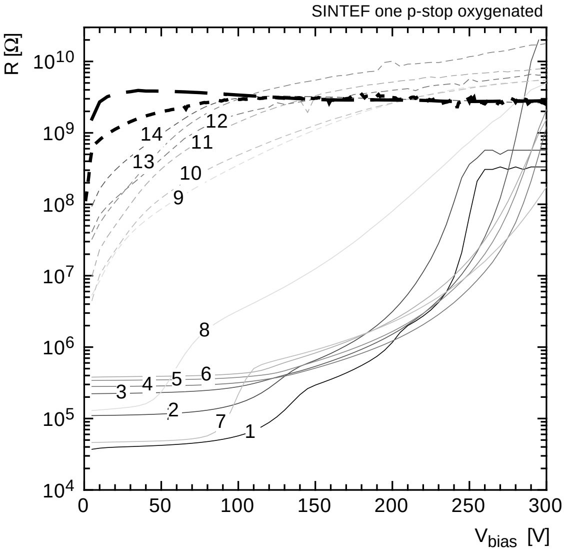

Figure 4.29: *Inter-pixel resistance for different pion-fluences (thin lines) and after 4 and 20 weeks annealing at 1°C (thick lines); top: non-oxygenated CSEM; right: oxygenated SINTEF (both with one p-stop ring). Resistances after type inversion are shown by dashed curves.*

Figure 4.30: *Inter-pixel resistance R as a function of pion-fluence for different bias voltages. The circles on the right axis show R after 20 weeks annealing. Right: non-oxygenated, CSEM; bottom: oxygenated, SINTEF; both had one p-stop ring.*

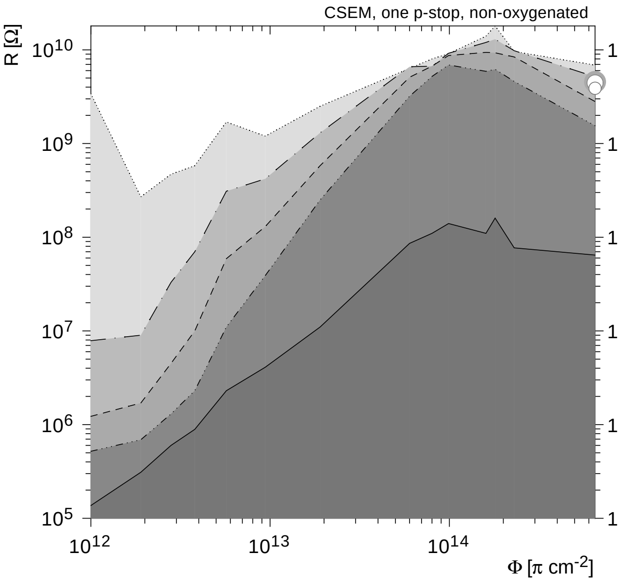

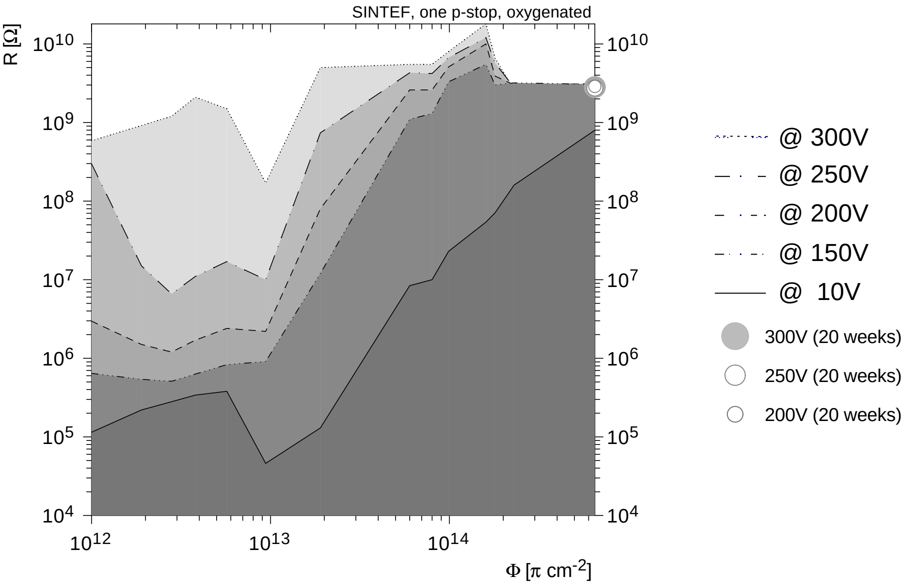

of an unbonded pixel after a fluence of $6 \cdot 10^{14}\,\mathrm{p\,cm^{-2}}$ and 38 weeks annealing is plotted in figure 4.31 as a function of V_{bias}. The same measurement was made twice, once at $T = +9°\mathrm{C}$ and once at $T = -9°\mathrm{C}$. There is almost no difference in the pixel potential. The inset shows the leakage current for both temperatures, which is clearly different between $+9°\mathrm{C}$ and $-9°\mathrm{C}$. Obviously, the surface properties relevant for the pixel isolation are much less temperature dependent than the leakage current.

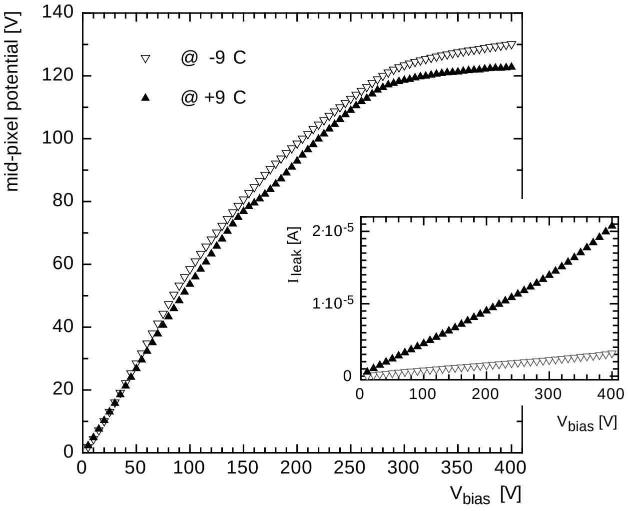

Figure 4.31: *Potential of an unbonded, irradiated pixel for $+9°C$ and $-9°C$. The inset shows the leakage current of the whole device for the same temperatures (measured with the Keithley 617 electrometer).*

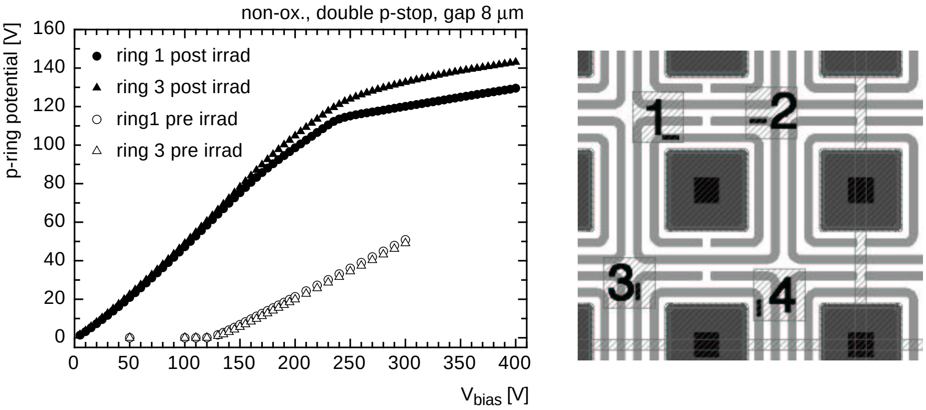

Figure 4.32: *Left: p-stop potentials before and after irradiation, the numbering of the p-rings is explained on the right 1, 4: p-rings next to a pixel implant, 2, 3: p-rings in between ring 1 and 4 (measured with the Keithley 617 electrometer).*

The saturation value of about 130 V is so high that there is a non-negligible probability of discharges. Since the distance between the sensor and the readout chip is around $20\,\mu\mathrm{m}$ the electric field between the unbonded pixel and the chip reaches $6.5 \cdot 10^{6}\,\mathrm{V\,m^{-1}}$. This is in the range of spontaneous spark ignitions. However, in section 4.6 it will be shown that no such phenomenon was observed on irradiated and bump-bonded detectors.

Figure 4.32 shows the potentials of two of the four p-stop rings between two pixels with double p-stops before and after irradiation. As for the unirradiated case the p-ring potentials after $6 \cdot 10^{14}\,\mathrm{p\,cm^{-2}}$ and 38 weeks annealing for ring 1 and 3 do not differ very much, even at high bias voltages. But the absolute potential of the p-stop rings for a given V_{bias} is much higher after irradiation than before, which implies that after irradiation the conductive channels are pinched off much stronger than before irradiation for $V_{bias} \geq V_{FD}$. This is in fact the main reason for the higher inter-pixel resistance after irradiation.

These measurements served as an input to a TCAD simulation of influences of the electron accumulation layer at the surface between the pixels, which is described in the next section.

4.1.5 Summary

- Before irradiation the open p-stop labyrinth provides a pixel isolation of a few $\mathrm{M\Omega}$ at $V_{bias} \approx V_{FD}$. The current between pixels at different bias voltages could clearly be separated into a bulk and a surface contribution. Depending on the production process (i. e., the oxide quality) the surface currents can be negligible small before irradiation. This causality could be confirmed with measurements on MOS-capacitors (see section 4.3). Whenever a surface current regime exists its pinch-off voltage depends on the distance between the p^+ implants.

- After hadron irradiations with $10^5\,\mathrm{Gy}$ the pixel isolation R is several orders of magnitude higher than before, namely in the order of $\mathrm{G\Omega}$. No difference between π- and p-irradiations was found. In contrast to the unirradiated case, R does not significantly depend on design variations (e. g., one or two p-stop rings). But after irradiation the surface currents are pinched off at a much lower bias voltage than before irradiation.

- The inter-pixel resistance saturates at a fluence $\Phi \approx 2 \cdot 10^{14}\,\mathrm{cm^{-2}}$, which corresponds to a dose of $\mathfrak{D} \approx 7 \cdot 10^4\,\mathrm{Gy}$.

- The high inter-pixel resistance causes an unbonded pixel to reach a constant potential of $\sim 130\,\mathrm{V}$ for $V_{bias} > 300\,\mathrm{V}$.

- The pixel isolation does not show any annealing for $V_{bias} \geq V_{FD}$ when the device is kept at temperatures around 0°C or below.

- For oxygenated silicon a higher inversion fluence was found compared to non-oxygenated material. Concerning the pixel isolation no significant difference between oxygen enriched and standard material could be seen.

The high inter-pixel resistance after irradiation gives cause for concern. If an unbonded pixel really charges up to 130 V the break-through-probability is not negligible. However, in section 4.6 it will be shown that no such phenomenon was observed during beam- and laboratory-tests. The p-stop rings fulfilled their task. But nevertheless, in the conclusions in chapter 5 some changes of the designs are proposed to reduce the danger of break-through.

Since there is no difference between oxygen enriched and standard material with regard to the pixel isolation, future investigations can be made with standard silicon, even when the final sensor will be produced with oxygenated material.

4.2 Electric Field Simulations

Apart from the inter-pixel resistance the electric field distribution close to the surface also alters with irradiation. In the worst case this can lead to breakdown[11] already at moderate bias voltages. A less fatal version of breakdown is the so called weak breakdown: At a certain bias voltage the leakage current starts to rise exponentially, but only in a very limited volume of the semiconductor. Therefore, the rise of the total leakage current is much slower than in a severe breakdown. An example of such a weak breakdown is shown in figure 4.33. The two curves denote the guard ring current and the pixel current of a 22×30 pixel sensor from our US-collaborators [44]. The pixels had double p-stop rings and were irradiated with $10^{14}\,\mathrm{p\,cm^{-2}}$ and measured at $-10°\mathrm{C}$. The guard rings start to break down at about 550 V. The pixel region shows a normal, square root like behaviour until the sensor is fully depleted. Around 300 V the current starts to rise with increasing bias voltage until a severe breakdown occurs roughly at the same voltage as for the guard rings. Similar behaviours have already been observed earlier (see e. g., [7]). To keep the overall leakage current as low as possible one would like to avoid such weak breakdowns or at least shift them to high bias voltages.

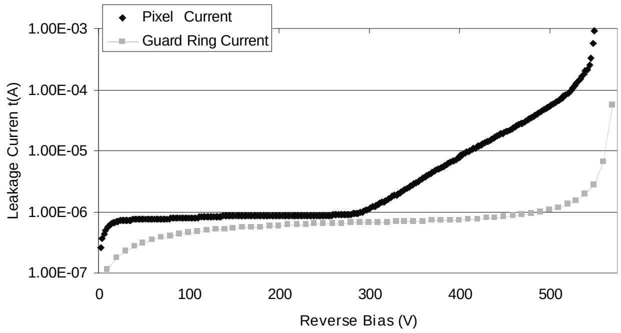

Figure 4.33: *Guard ring and pixel current of an irradiated* 22×30 *pixel sensor. At 300 V the pixels show a weak breakdown.*

Such phenomena can be explained by high field strengths close to the p-stop rings (see e. g., [45, 46]). Locally the field can be high enough to ionise the silicon atoms. Either thermally excited electrons get enough kinetic energy to empower - through collisions - other electrons to overcome the bandgap (avalanche generation) or the depletion widths are that small that electrons can tunnel through the band gap at the junction (Zener breakdown).

The purpose of the simulation was to understand where the maximal field strength occurs and how it depends on the accumulation layer concentration and on design parameters. This knowledge is important to avoid breakdowns and to control the drift of the signal charges to the pixels. First, I have simulated the device geometry with the process parameters described in

---

[11] See section 4.4 for a short introduction to breakdown theory.

section 2.2, using the program DIOS from the ISE-TCAD package [16]. Afterwards, the electric field simulation was performed with the DESSIS program from the same package. DESSIS numerically solves a system of combined differential equations containing the Poisson equation and two continuity equations for electrons and holes. The Poisson equation can be expressed as

$$-\nabla^2 V = \nabla \cdot \vec{\mathcal{E}} = \frac{\rho_q}{\varepsilon_{si}\varepsilon_o} \quad , \tag{4.9}$$

with V being the potential, $\mathcal{E}$ the electric field and $\rho_q = q(p_0 - n_0)$ the volume charge density. The electron and hole continuity equations are

$$\begin{aligned} \nabla \cdot \vec{J_n} &= qR + q\frac{\partial n_0}{\partial t} && (4.10) \\ \nabla \cdot \vec{J_p} &= qR + q\frac{\partial p_0}{\partial t} \quad , && (4.11) \end{aligned}$$

where R is the electron-hole recombination rate, $\vec{J_n}$ and $\vec{J_p}$ are the electron and hole current densities and n_0 and p_0 denote the electron and hole concentrations.

The boundaries are normally treated with reflective von Neumann boundary conditions:

$$\vec{\psi} \cdot \vec{N} = 0 \tag{4.12}$$

where ψ stands either for $\vec{\mathcal{E}}$, $\vec{J_n}$ or $\vec{J_p}$ and $\vec{N}$ is the direction normal to the surface. Only for ohmic contacts Dirichlet boundary conditions are applied to guarantee charge neutrality and equilibrium:

$$\begin{aligned} n_0 - p_0 &= N_D - N_A && (4.13) \\ n_0 \cdot p_0 &= n_i^2 \quad , && (4.14) \end{aligned}$$

where n_i is the free electron density in intrinsic silicon. The n$^+$pixel implants were on ground potential and the p-stop rings were kept floating. The bias voltage was applied on the backside (−300 V). The simulation was done in two dimensions and comprised the cross-sectional area between two n$^+$pixel implants (100 μm wide and 300 μm deep).

Figure 4.34 shows the electric field distribution in the top third of such a cross-section (100 μm in depth). Pixels with double p-stop rings were used here. On the top right and top left corner parts of the n$^+$ implants of the pixels are visible. The four shallow regions between the pixels with very low field strength are the p$^+$ implants of the p-rings. Between the n$^+$pixels there are several regions where the field strength is drastically reduced (bright spots in figure 4.34). As it is shown in the next subsection this is due to the large gaps between the n$^+$ implants. In the silicon bulk below these gaps the electric field lines are not parallel any more. They are bended apart towards the n$^+$ electrodes, which causes the electric field strength to be lower right between the pixel-electrodes.

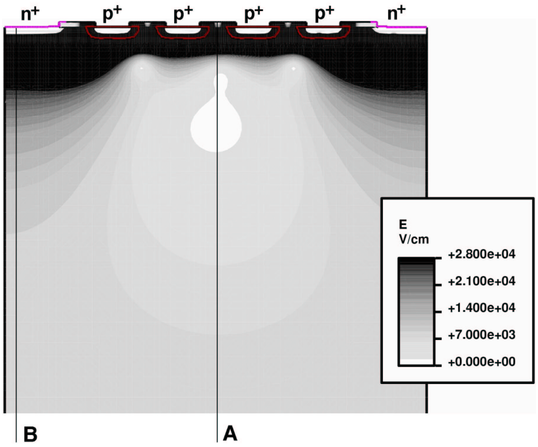

Figure 4.34: *Cross-section through the $\mathcal{E}$-field distribution of a double p-stop sensor with an electron accumulation layer of $2.5 \cdot 10^{13}\,cm^{-2}$ ($\sim 100\,\mu m$ in vertical as well as in horizontal dimension).*

4.2.1 Electric Field Distribution Perpendicular to the Surface

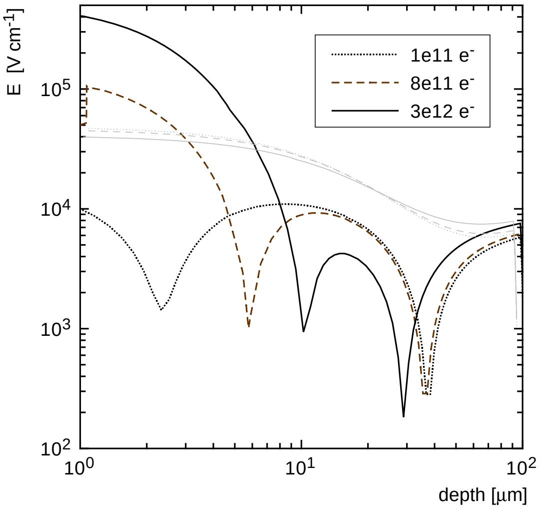

Figure 4.35: *Simulated electric fields in the bulk in z-direction (perpendicular to the surface) for different accumulation layer concentrations; dark lines: between pixels (along line A in figure 4.34), gray lines: below n^+implant (line B in figure 4.34).*

The electric field through the bulk - perpendicular to the surface - is plotted in figure 4.35 for three different values of the electron accumulation layer concentrations (10^{11}, $8 \cdot 10^{11}$ and $3 \cdot 10^{12}\,\text{cm}^{-2}$). The black curves show the field strength versus bulk depth between two pixels (along line A in figure 4.34), while the light gray lines give the field strength right below the n^+ implants (along line B in figure 4.34 . The field strength below the pixel implants does not depend on the electron accumulation layer concentration, in contrast to the field strength between the pixels. A high electron concentration in the accumulation layer clearly shifts the low-field zones deeper into the bulk.

The results of the same simulations for a device with one p-stop per pixel are

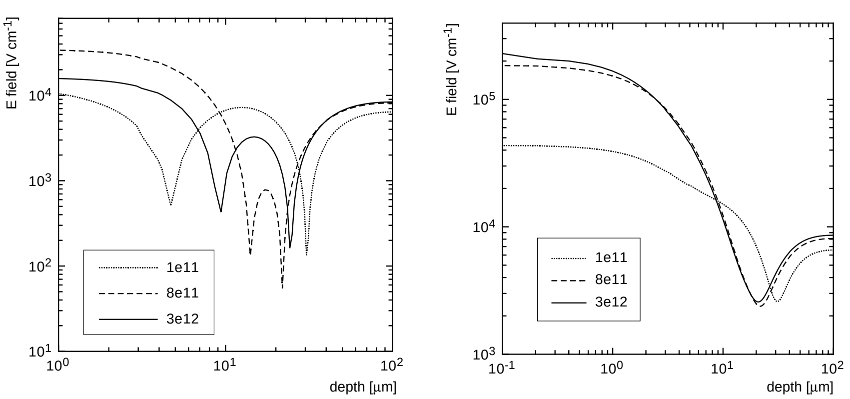

Figure 4.36: *The same electric field strengths as in figure 4.35, but for a sensor with only one p-stop ring per pixel. Left: a 72 μm gap between the n$^+$implants of two neighbouring pixels (22 μm between the p-stops), right: the gap between the n$^+$implants only 60 μm wide (18 μm between the p-stops).*

displayed in figure 4.36. For the curves on the left side the gap between the n$^+$ implants was 72 μm, for the one on the right side it was 60 μm. As can be seen the low-field area is much less intense and more localised in the right plot of figure 4.36 than in the left one. Obviously, the smaller gap between the n$^+$ implants reduces the bending of the field lines. In particular, this result is important for the Lorentz-angle measurement described in section 4.7. There, we found that the charge sharing due to the Lorentz-drift is strongly influenced by this low electric field zones between the pixels ("non-uniform Lorentz angle"). If this low field zone can be partly eliminated by shrinking the gap between the n$^+$ implants the charge sharing pattern is simplified and hence more predictable.

In addition, a reduction of this gap-width would also improve the charge collection efficiency of tracks which traverse the sensor between two pixels. As shown in section 4.6 the charge collection efficiency for such tracks is reduced by about 20 % in a sensor with double p-stop rings. A less pronounced low field zone between the pixels would help to improve the charge collection efficiency for such tracks.

4.2.2 Electric Field Distribution Parallel to the Surface

Unlike in the perpendicular case, problems arise due to too high field strengths in the directions parallel to the surface. In figure 4.34 one can already see that the highest electric field strengths occur just below the surface of the sensor. This fields can cause breakdowns, as it was described above. In figure 4.37 one finds the simulated electric field and the potential distribution between two pixels with one p-stop ring each.

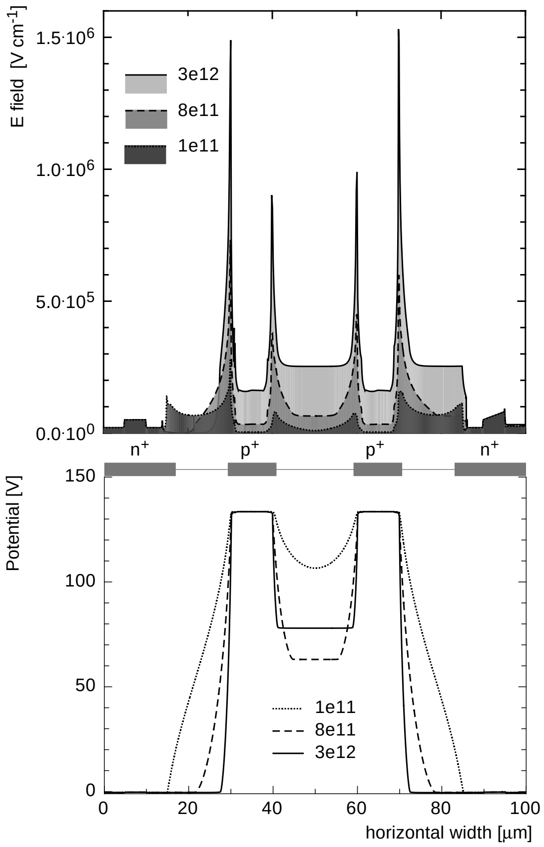

Figure 4.37: *Electric field (top) and potential (bottom) along the surface between two pixels, each pixel has a single p-stop ring (p$^+$), the pixel-implants are denoted with n$^+$.*

The maxima of the electric fields sit at the p-n junctions between the p-stops and the n-type bulk. The highest fields occur at the edge of the p$^+$ implants which face the n$^+$ layers of the pixels (see also figure 4.38). That is due to the high potential of the p-stop rings. The n bulk silicon is on ground potential, since it is connected to the n$^+$ pixel implants. Hence, the whole potential drop happens across the thin depletion zones of the junction. Their widths x_n and x_p (in the n-type, p-type region, respectively) are related to the doping concentration by

$$x_n \, N_D = x_p \, N_A \quad . \tag{4.15}$$

The higher the doping (or the accumulation layer concentration) the smaller the depletion width and hence the higher the electric field. This is quantitatively shown in figure 4.39 for two devices with a different gap between the n$^+$ pixel implant ($72\,\mu$m and $60\,\mu$m). With an increasing accumulation layer concentration also the electric field maxima rise.

The accumulation layer concentration can not be influenced, since the introduction of oxide charges is unavoidable. But is the distance between the implants can be changed. The maximum electric fields strengths extracted from simulations with different distances between the n$^+$ implants are plot-

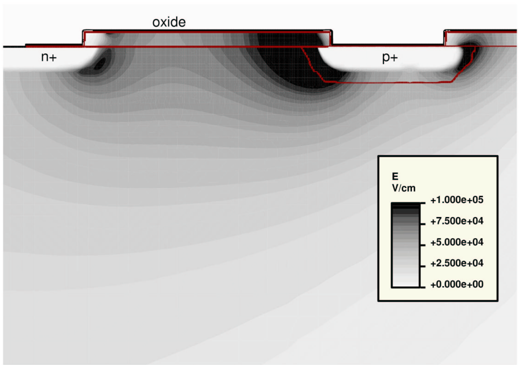

Figure 4.38: *The maximum electric field strength occurs at the edges of the p^+implants.*

ted on the right side of figure 4.39. The maximum fields are reduced for smaller distances. The effect is small but it could shift the starting point of the weak breakdown (figure 4.33) to higher voltages, which in turn would allow to run the sensor at higher values of V_{bias}.

Another possibility is to reduce the doping concentration in the p^+implants of the p-stop rings. According to equation (4.15) this measure increases the depletion widths $x_{n,p}$, which has a similar beneficial effect as a low accumulation layer concentration (figure 4.39 left).

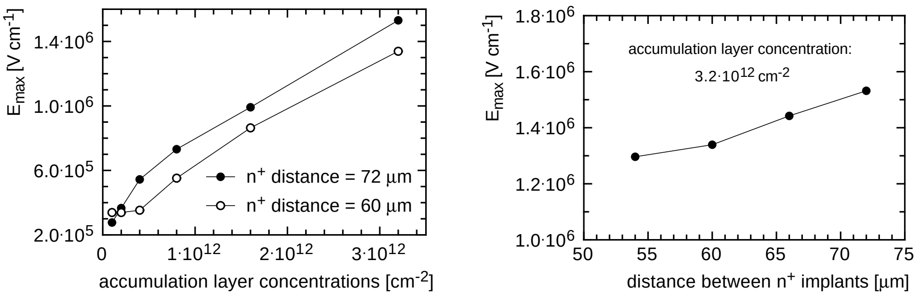

Figure 4.39: *Left: maximum field strengths as a function of the accumulation layer concentration; right: maximum field as a function of the distance between n^+ implants.*

4.2.3 Summary

- The electric field between pixels is strongly dependent on the distance between the n^+ pixel implants. In the direction perpendicular to the surface strong non-linearities occur which are, after irradiation, shifted deeper into the bulk by the negative charge accumulation layer at the surface. They can reach as far as 50 μm into the silicon bulk. Shrinking the gap between the n^+ implants reduces their intensiveness, which has a favourable effect on the charge sharing caused by the Lorentz-force, as described in section 4.7.

➢ In the directions parallel to the surface the electric field maxima occur at the edges of the p-stop rings, which face the n^+ implant. They also increase with an increasing electron accumulation layer concentration. A reduction of the distance between the n^+ implants causes the maxima to go down again.

Hence, from the electric field point of view it would be favourable to make the gap between the n^+ pixel implants as small as possible.

4.3 Measurements on MOS Capacitors

An important tool to study semiconductor surfaces and interfaces is the MOS capacitor shown in figure 4.40. It consists of a weakly doped silicon substrate (n^-or p^-) on which a thin SiO_2 layer is grown. On top an aluminium layer is deposited, called gate contact - a term from the MOS-transistor technology. The backside of the silicon substrate is provided with an ohmic contact (n^+ implant).

I used such MOS-capacitors to investigate the Si-SiO_2 interface, namely to separately measure the oxide charge density Q_{ox} and the interface trap density D_{it}. The oxide charge Q_{ox} is a fixed positive charge layer in the SiO_2 film, created by imperfections during the oxidation process and by radiation damages in the oxide. The electron accumulation layer at the bulk silicon surface mainly consists of mirror charges to Q_{ox}. The interface traps D_{it} (or trapped interface charges Q_{it}) are due to the breaking of covalent bonds at the Si-SiO_2 interface, created by structural defects or radiation.

The basic principles of MOS capacitors are explained in appendix D, where also the equations used to extract Q_{ox} and D_{it} from the measurements are derived. Sections 4.3.1 and 4.3.2 describe my measurements on unirradiated and irradiated MOS capacitors, and section 4.3.3 summarises the results.

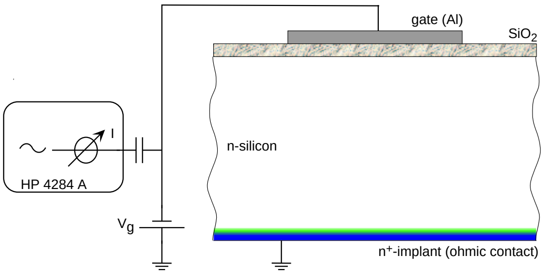

Figure 4.40: *Cross section of a MOS capacitor with a sketch of the high frequency measurement setup.*

4.3.1 Q_{ox} and D_{it} of Unirradiated MOS Capacitors

With the tools developed in appendix D the interface trap density D_{it} and the oxide charge concentration Q_{ox} can be separated. The idea is to use the fact that interface traps only respond to low frequency AC-signals, whereas the charge accumulation layer (which is the mirror charge of Q_{ox}) responds to both, high and low frequency modulations.

For the **oxide charge** a high frequency C-V measurement was used. From this measurement I extracted the flat band voltage shift[12] ΔV_{FB}. With the knowledge of ΔV_{FB} the oxide charge Q_{ox} could be determined. To do so,

---

[12] The voltage that has to be applied on the gate to counterbalance the band bending due to oxide charges, work-function differences, etc., see appendix D.

the first step was to calculate the flat band capacitance C_{FB}, using equation (D.6) and the oxide capacitance C_{ox}, which was measured for each device in the accumulation regime. The gate voltage V_g, which corresponds to the calculated flat band capacitance C_{FB}, was then extracted from the measured C-V curve. This value of V_g directly translates to the flat band voltage shift ΔV_{FB}, given in equation (D.16). With the known work function difference ϕ_{ms} and oxide capacitance C_{ox}, the oxide charge concentration Q_{ox} was calculated.

The flat band capacitances were measured with $5 \times 5\,\mathrm{mm}^2$ capacitors at room temperature (293 K), using the HP 4284 A capacitance meter[13] (AC signal: 5 mV, 10 kHz). A sketch of the setup is shown in figure 4.40. For n-type bulk material the relation $(n_0 + p_0) \approx N_D$ holds, and N_D is known from table 3.2. With that information the Debye length[14] L_D can be calculated with equation (D.5). Afterwards the corresponding values of ΔV_{FB} are extracted from high frequency MOS-CV measurements, which are displayed in figures 4.41, 4.42 and 4.43. In table 4.1 the results for two SINTEF devices (oxygenated and non-oxygenated) and a CSEM capacitor are listed.

Table 4.1: *Results of the Q_{ox} measurements before irradiation.*

	L_D	C/C_{ox}	ΔV_{FB}	Q_{ox}
SINTEF ox	2.3 μm	0.49	-1.6 V	$3.3 \cdot 10^{10}\,\mathrm{q^+\,cm^{-2}}$
SINTEF non-ox	2.3 μm	0.50	-1.4 V	$2.5 \cdot 10^{10}\,\mathrm{q^+\,cm^{-2}}$
CSEM non-ox	3.0 μm	0.49	-7.5 V	$15.8 \cdot 10^{10}\,\mathrm{q^+\,cm^{-2}}$

The final results for Q_{ox} were calculated with equation (D.16). They are also listed in table 4.1. Concerning the uncertainties of the measurements the systematic errors were believed to be much higher than the statistical ones. Therefore, only an estimated error can be given for the numbers in table 4.1. An error of about 10 % was assumed for L_D and for the measured CV curve. The determination of C_{ox} was afflicted with an error of 20 %. This leads to a total uncertainty of 23 %.

It is striking that the oxide charge concentration in the CSEM device is about a factor five higher than in the two SINTEF ones. The indication of differences in the production process between the two vendors found in section 4.1.4.1 is confirmed here: The oxide quality of the CSEM process is much worse than the one of the SINTEF process, i. e., has a much higher oxide charge concentration. Since the vendors do not publish the exact environmental conditions of their oxide growing process (gas-mixture, pressure, ...) I can not give a reason for this difference.

---

[13] The capacitance meter measures the current voltage phase-shift and amplitude-difference of the applied AC-signal.

[14] The screening length of the Debye Hückel-theory; i. e., the characteristic distance over which charges are shielded.

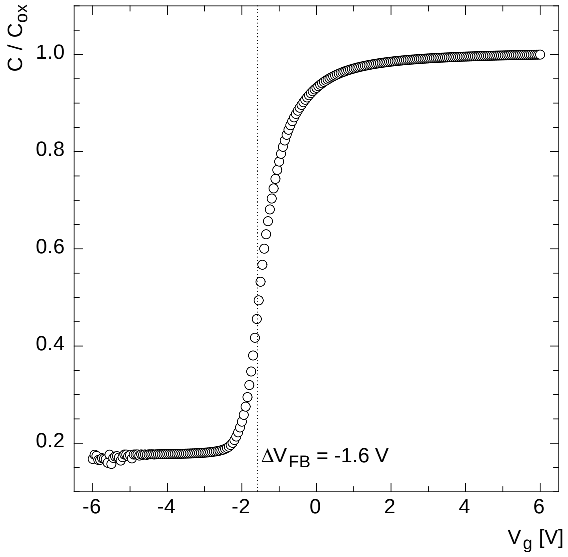

Figure 4.41: *High frequency MOS-CV measurements of an oxygenated SINTEF capacitor to extract V_{FB}.*

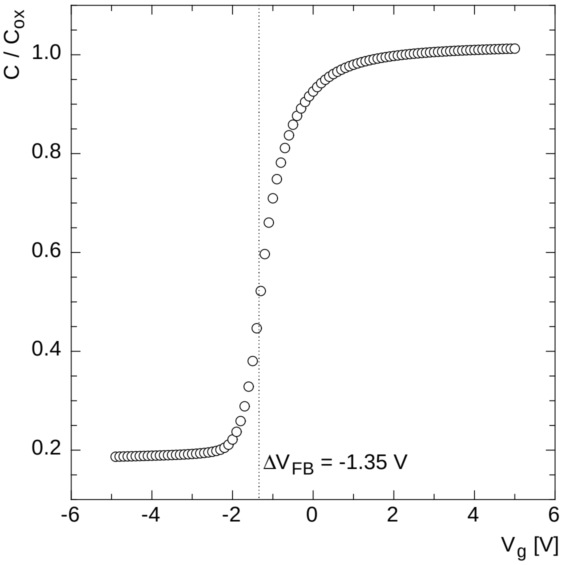

Figure 4.42: *Ditto for a non-oxygenated SINTEF device.*

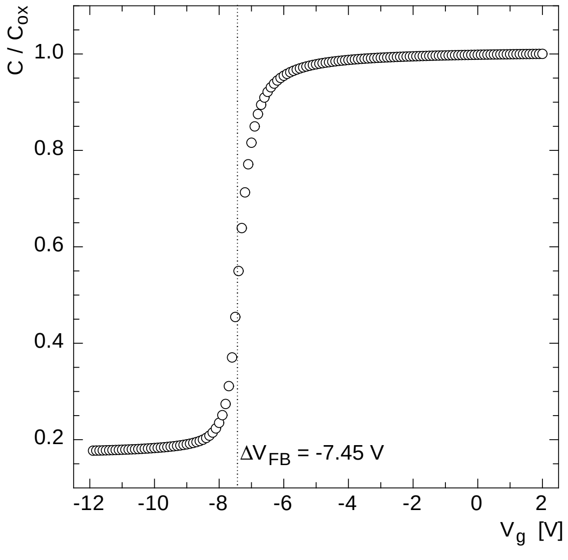

Figure 4.43: *Ditto for a non-oxygenated CSEM capacitor.*

The oxygenation of the silicon bulk does not have an influence on the oxide charges since the Q_{ox}-values of the oxygenated and the non-oxygenated SINTEF device are consistent within their errors. This result indicates that the oxygen charges in the SINTEF sensors can not be annealed at high temperatures, since the devices are heated to about 1000°C for dozens of hours during the bulk oxygenation process.

In order to determine the **interface trap density** D_{it} a combination of high and low frequency measurements was used [47]. From the difference between the two around the flat band voltage V_{FB}, D_{it} can be calculated using equations (D.20) and (D.21) from appendix D.

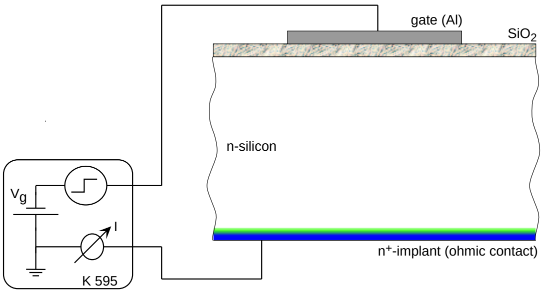

Figure 4.44: Setup for the low frequency measurements.

The measurements were done with $5 \times 5\,\mathrm{mm}^2$ capacitors for the non-oxygenated devices. For the oxygenated material a smaller capacitor with an area of $3\,\mathrm{mm}^2$ was tested. A 100 kHz AC signal was used for the high frequency measurements (done with the HP 4248 A capacitance meter and the setup in figure 4.40), whereas the low frequency curves were obtained with the quasi-static technique with frequencies of 1 Hz or 0.5 Hz (using the Keithley 595 capacitance meter). In the quasi-static technique not a sine-like AC signal is used, but a voltage step of about 0.1 V is applied to one electrode of the capacitor and the influenced charge on the other electrode is measured with an electrometer (see figure 4.44). All measurements were performed at room temperature.

The resulting CV-curves are displayed in figures 4.45, 4.46 and 4.47. The D_{it} values obtained with equations (D.20) and (D.21) are shown as insets. The averaged values are summarised in table 4.2. The first error denotes the standard deviation of the D_{it} values for different V_gs, the second is a systematic error that originates in measurement uncertainties of C_{LF}, C_{HF} and C_{ox}, which were all estimated to be 20 %.

The values are all consistent within errors. In contrast to the oxide charges there are no significant differences between CSEM and SINTEF concerning the interface defect densities. Hence, the different production processes do not influence the Si-SiO$_2$ interface, i. e., both processes have about the same amount of lattice mismatches or dangling bonds at the interface.

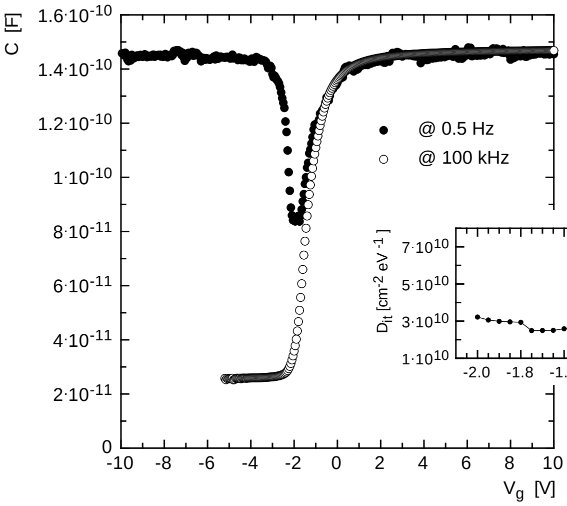

Figure 4.45: *D_{it} measurement of an oxygenated SINTEF MOS-capacitor ($3\,\mathrm{mm}^2$).*

Figure 4.46: *Ditto of a non-oxygenated SINTEF MOS-capacitor ($25\,\mathrm{mm}^2$).*

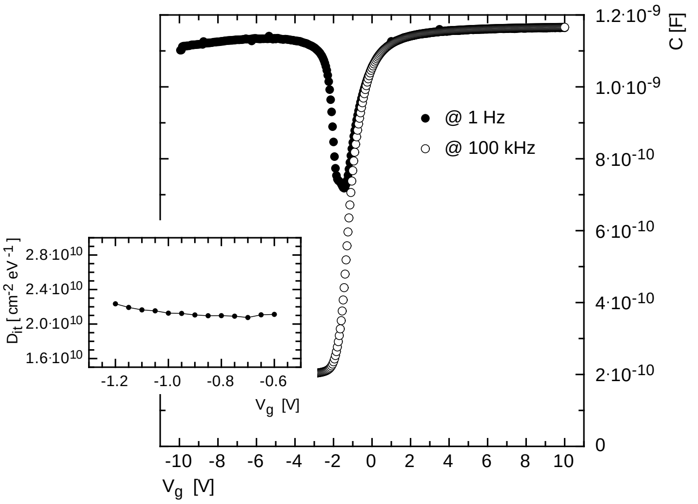

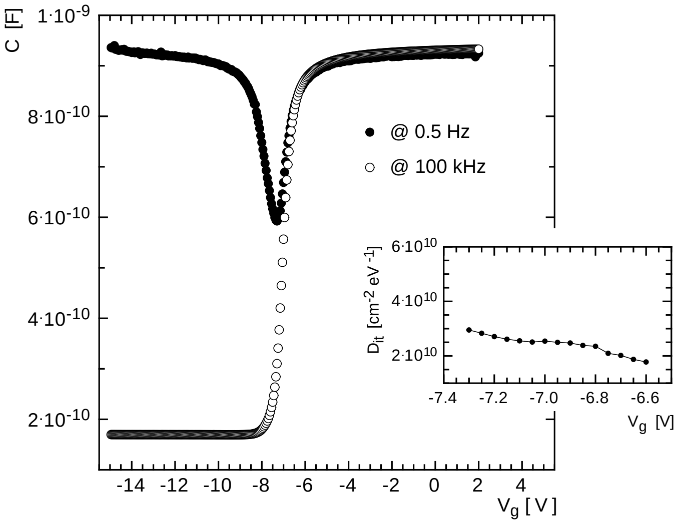

Figure 4.47: *Ditto of a non-oxygenated CSEM MOS-capacitor ($25\,\mathrm{mm}^2$).*

Table 4.2: *D_{it} measurements before irradiation.*

SINTEF ox	$D_{it} = (3.0 \pm 0.4 \pm 0.9) \cdot 10^{10}\,\mathrm{cm}^{-2}\,\mathrm{eV}^{-1}$
SINTEF non-ox	$D_{it} = (2.1 \pm 0.1 \pm 0.6) \cdot 10^{10}\,\mathrm{cm}^{-2}\,\mathrm{eV}^{-1}$
CSEM non-ox	$D_{it} = (2.4 \pm 0.3 \pm 0.7) \cdot 10^{10}\,\mathrm{cm}^{-2}\,\mathrm{eV}^{-1}$

4.3.2 Measurements After Irradiation

Two difficulties occurred after irradiation. On the one hand no reasonable low frequency (or quasi-static) CV measurements were possible any more. This was due to the high concentration of bulk defects which acted as generation and recombination centres. They created a statistical noise which completely covered up the tiny AC-induced charge signal.

On the other hand the calculation of the Debye length L_D turned out to be more troublesome than expected. According to equation (D.5) all free charge carriers that can respond to the AC signal have to be taken into account to calculated L_D, and not only the effective doping concentration N_{eff}. If it is assumed that, after type inversion, all irradiation induced acceptor states respond to the AC signal, the correct charge concentration expression in L_D would be $(2N_D + N_{\mathit{eff}})$. If non of the bulk defects would react to the AC signal the correct term would simply be N_D, as in the unirradiated case. Both of these assumptions lead to flat band capacitances C_{FB} that could not be brought into accordance with the measurements. As a conclusion it must be assumed that the bulk defects only partly respond to the AC signal.

Accordingly, the flat band voltage V_{FB} can not be determined with the method that was used in the unirradiated case. A simpler method to estimate V_{FB} uses the following relation instead of equation (D.6):

$$\frac{C_{FB}}{C_{ox}} \approx \frac{1}{2}\left[\left(\frac{C}{C_{ox}}\right)_{max} + \left(\frac{C}{C_{ox}}\right)_{min}\right] \quad . \tag{4.16}$$

Here, the flat band capacitances C_{FB} is approximated by the arithmetic mean between the maximal high frequency capacitance (in the accumulation regime) and its minimum (in the inversion regime). The corresponding flat band voltage shifts ΔV_{FB} was then extracted from the measured CV-curve, in the same way as for the unirradiated capacitors.

In figure 4.48 the measured CV-curves after irradiation with $4.3 \cdot 10^{14}\,\pi\,\mathrm{cm}^{-2}$ and 8 weeks of annealing at +1°C are plotted. As a comparison the unirradiated CV measurements are also displayed. The ΔV_{FB} values obtained with the estimation (4.16) are drawn as dotted lines. The following values were obtained:

$$\text{CSEM:} \qquad \Delta V_{FB} \approx -40\,\mathrm{V} \tag{4.17}$$

$$\text{SINTEF:} \qquad \Delta V_{FB} \approx -4\,\mathrm{V} \tag{4.18}$$

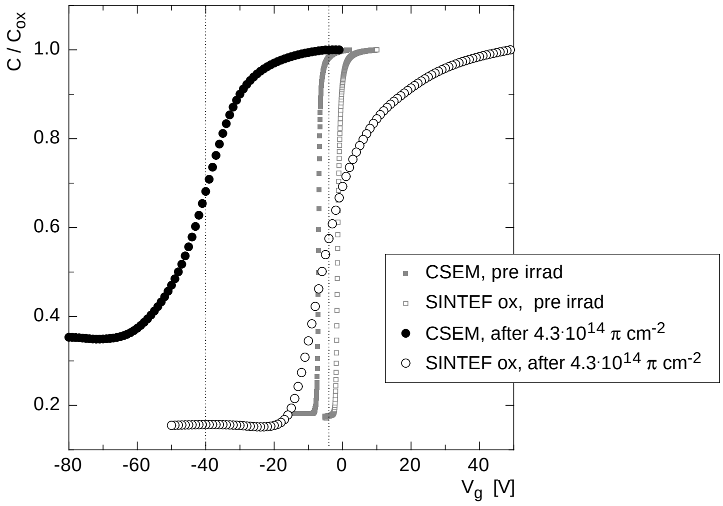

Figure 4.48: *MOS-CV measurements after irradiation with* $4.3 \cdot 10^{14}\,\pi\,cm^{-2}$*. In addition, the unirradiated measurements are displayed in gray (small symbols).*

The big difference between CSEM and SINTEF is conspicuous. The high value of V_{FB} for CSEM can easily be explained by the radiation induced increase of the oxide charge density Q_{ox}. But why is the SINTEF value so low? Both curves are clearly stretched out. This implies that D_{it} increased after irradiation for both devices[15]. But there is a big difference in case of the flat band voltage[16]. As shown on page 66 it is unlikely that the low SINTEF value was caused by annealing during the 8 weeks storing-period. Surface annealing only plays a significant role at much higher temperatures.

It is much more conceivable that, at least in the SINTEF device, the interface traps also respond to the high frequency AC signal. According to [19] interface traps sometimes follow the AC modulation up to 100 MHz (unfortunately our CV-meter (HP4284A) was limited to 1 MHz). As a consequence, equation (D.16) is not valid any more to calculate V_{FB}. Therefore, the only statement concerning Q_{ox} and D_{it} that can be made is that in the SINTEF case D_{it} is presumably of the same order of magnitude as Q_{ox}, whereas for the CSEM device Q_{ox} is much higher.

But another fact is also striking in figure 4.48. The capacitance is still high for gate voltages higher than V_{FB} and low for $V_g < V_{FB}$. This can only mean that the surface silicon layer is still n-type and did not experience a type inversion, even after $4.3 \cdot 10^{14}\,\pi\,\mathrm{cm}^{-2}$! Similar hints were also found from surface resistivity measurements by other groups [14]. Up to now this

---

[15] See on page 145 for explanations about D_{it}.

[16] The high frequency CV-curves were also measured at different frequencies, but the flat band voltage V_{FB} was not found to be frequency dependent.

phenomenon is only poorly understood. It is thought to be related to the defect-complex formation mechanisms (see section 2.3 and [14]).

4.3.3 Summary

MOS capacitors are very powerful tools to measure parameters like oxide charge, accumulation layer concentration or interface defect densities. Therefore, they are very well suited to compare the quality of different production processes. Capacitors from the vendors CSEM and SINTEF were investigated in this work. They were checked before irradiation and after a dose of $\sim 10^5\,\mathrm{Gy}$.

- ➢ Before irradiation the oxide charge density Q_{ox} in the CSEM devices was found to be five times higher than in the SINTEF ones. The oxide charge directly translates into the accumulation layer concentration. This explains why no surface current regime could be found for the unirradiated SINTEF devices in the pixel isolation measurements (see section 4.1.2). The interface defect densities D_{it} were similar (within errors) for both vendors.
- ➢ After a harsh irradiation with $4.3 \cdot 10^{14}\,\pi\,\mathrm{cm}^{-2} \triangleq 1.4 \cdot 10^5\,\mathrm{Gy}$ the interface defect density was still much lower than the oxide charge density in the CSEM device. In the SINTEF capacitors both were presumably of the same order of magnitude. It was difficult to give quantitative results after irradiation since a clear determination of Q_{ox} and D_{it} would have required measurements in extreme frequency domains which were not feasible with the available equipment.
- ➢ But a clear signature for a shallow n-type surface regime was found that did not experience a type-inversion. The investigation of the processes responsible for this effect are still going on. They also have to take into account the complicated defect formation procedures in silicon.

4.4 Guard Ring Tests

The function of guard rings is to prevent high currents in the sensor, which on the one hand could completely cover up the signal charge and on the other hand heat up the sensor, which in turn would further increase the current. To illustrate the mechanisms involved consider a device with a single, large, planar pn-junction, as shown in figure 4.49. Due to crystal defects the energy band structure is destroyed at the cut edge. On the left side of figure 4.49 the oxide is not covered by a metal gate. From section 4.3 we know that an electron accumulation layer forms at the semiconductor surface due to the positive oxide charges. This conductive layer is at the potential V_{bias}, because the resistivity of the cut edge on the left side is low enough to guarantee a charge exchange between the accumulation layer and the backside n^+ implant. The full bias voltage drops over a short distance next to the diode (marked as "high field region" in figure 4.49). When the electric field strength at this point exceeds a certain value it causes a sudden increase of the current flow, leading to breakdown.

On the right side of figure 4.49 another cause for breakdown is shown. There, the silicon surface potential is kept close to ground by the covering metal field plate, which extends to the right cut edge. This causes the depletion region to expand laterally. If it reaches the cut edge, a huge generation current is produced since the crystal is heavily damaged at the edge.

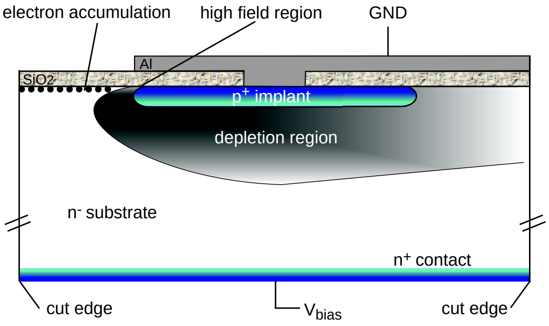

Figure 4.49: *Two different causes for breakdown. See text for explanations (after [14]).*

The current creation on the right side of figure 4.49 is relatively easy to control with design measures (e. g., by reducing the overlap of the metal field plate). But the breakdown phenomena on the left side are more difficult to avoid. They are discussed in more detail in section 4.4.1. Section 4.4.2 deals with my measurements and results, which are then briefly summarised in section 4.4.3.

4.4.1 Phenomenological Description of Breakdown

First, it is noteworthy that the breakdowns are purely electrical (there is no mechanical damage) and that they are reversible, as long as the power dissipation is kept small.

There exist two different mechanisms for the current creation in the high field region. One speaks of Zener breakdown and avalanche breakdown. The Zener mechanism involves a direct excitation of electrons from the valence band into the conduction band due to tunnelling. In avalanche breakdown the acceleration of thermally excited electrons is sufficient to ionise other silicon atoms and create an avalanche.

It is helpful to consider the relationship between the doping concentration N_D, the depletion region width x_n and the average electric field $\mathcal{E}$ in a pn-junction. For simplicity, let us consider an abrupt p$^+$-n$^-$ junction and neglect the depletion width in the p$^+$ region. The depletion width x_n in the n-type silicon is (see appendix C)

$$x_n = \sqrt{\frac{2\varepsilon_{si}\varepsilon_o}{qN_D}\left(V_{bias} + V_i\right)} \tag{4.19}$$

and the average electric field

$$\mathcal{E} = \frac{(V_{bias} + V_i)}{x_n} = \sqrt{\frac{qN_D\left(V_{bias} + V_i\right)}{2\varepsilon_{si}\varepsilon_o}} \quad , \tag{4.20}$$

with $\varepsilon_{si}\varepsilon_o$ as the permittivity of silicon, N_D the donor concentration, q the elementary charge and V_i the built in voltage of the junction.

4.4.1.1 Zener Breakdown

Equations (4.19) and (4.20) show that, when N_D is large, x_n is small and $\mathcal{E}$ is high. Under these conditions electrons from the valence band of the p-side of the junction can tunnel into the conduction band of the n-side as shown on the left side of figure 4.50. Calculations show (see e. g., [11]) that the tunnelling probability is significant only when the width of the potential barrier is small compared to the wavelength of the electron. For thermal electrons at room temperature the wavelength[17] is of the order of 1 μm. For significant tunnelling to occur, the barrier width should be orders of magnitude lower. The barrier width x_t is given by $q\mathcal{E} = -E_g/x_t$ [11]. Hence, for silicon with a band gap energy $E_g = 1.12\,\text{eV}$, a significant tunnelling current can establish for $\mathcal{E} \gtrsim 10^7\,\text{V}\,\text{m}^{-1}$.

4.4.1.2 Avalanche Breakdown

According to equation (4.20) the electric field $\mathcal{E}$ becomes smaller for smaller doping concentrations N_D. At a certain point, $\mathcal{E}$ is too small to allow the charge carriers to tunnel through the band gap. But it might still be high enough for the thermally excited charge carriers to be accelerated to a kinetic

---

[17] For a free electron as an approximation, the wavelength λ is given by $\frac{3}{2}kT = h\frac{c}{\lambda}$.

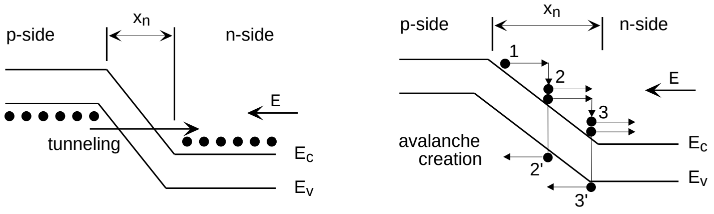

Figure 4.50: *Energy diagrams of the breakdown mechanism in a pn-junction. Left: Zener breakdown, right: avalanche multiplication.*

energy higher than the band gap energy E_g. A carrier that has an energy higher than E_g can produce a secondary electron-hole pair by knocking out an electron from a covalent bond in the lattice (see the right side of figure 4.50). The secondary carriers produced by this process can create further electron-hole pairs which leads to an avalanche.

A quantitative treatment of avalanche breakdown is given by the ionisation integrals of the minority carriers (see e. g., [11]). They state that avalanche breakdown for electrons or holes sets in if the following conditions are fulfilled:

$$\int_0^{x_n} \alpha_p \exp\left(-\int_0^x (\alpha_p - \alpha_n)\, dx'\right) dx \;\geq\; 1 \tag{4.21}$$

for holes and

$$\int_0^{x_p} \alpha_n \exp\left(-\int_0^x (\alpha_n - \alpha_p)\, dx'\right) dx \;\geq\; 1 \tag{4.22}$$

for electrons, where α_n and α_p are ionisation coefficients[18] for electrons and holes and x_n, x_p the depletion widths in n-type, p-type silicon, respectively.

The ionisation integrals (4.21) and (4.22) can be numerically calculated with the DESSIS program from the ISE TCAD package [16]. I have done several such calculations for different guard ring designs and accumulation layer concentrations. In all of them breakdown occurred first at the p^+-n junctions between the guard rings and the bulk silicon, which point towards the centre of the diode (see figure 4.51). Therefore, it is important to have small metal field plates on top of the guard rings - which slightly extend over the p^+ implant - to reduce the electric field peaks and shift the breakdown to higher bias voltages. (see also figures 3.11 and 4.49).

Experimentally, Zener breakdown can be distinguished from avalanche breakdown by the following criteria [11]:

---

[18] A material constant which is determined by the impact ionisation cross-section averaged over a non-equilibrium electron distribution function [37, 48].

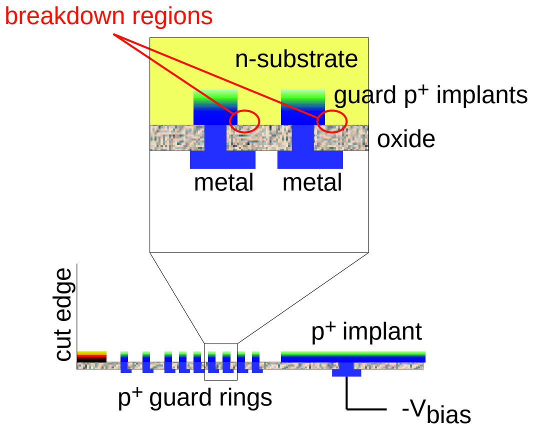

Figure 4.51: *Schematic picture of the guard rings. The ionisation integrals (4.21) and (4.22) are highest in the breakdown regions.*

- The I-V characteristic in the breakdown region is soft (slowly rising current) in case of Zener breakdown, and hard high and fast current increase) in case of avalanche breakdown.
- For Zener breakdown, the breakdown voltage decreases with temperature, whereas for avalanche breakdown it increases.
- Avalanche breakdown is always accompanied by current instabilities at the onset of breakdown. No such instabilities are observed in Zener breakdown.

4.4.2 Measurements on Different Designs

The CMS pixel guard ring concept is illustrated in figures 3.10 and 4.51. Most of the specific guard ring tests were done with CSEM test diodes, which used the same guard ring concept, but had only a $1 \times 1\,\mathrm{mm}^2$ large p^+ backside-implant and the pixels were replaced by a continuous $1\,\mathrm{mm}^2$ n^+ implant. All of them were provided with the metal field-plates described above. Apart from these test-diodes the guard rings of the 22×30 pixel- and 5×5 pixel-structures were also used. The various designs of the guard ring test diodes are described in section 3.1, and the different devices are listed in table 4.3.

Two methods were applied to measure the guard ring performance. Their measurement setup is shown in figure 4.52. With the first one (method 1) only the diode current is measured, but the guard ring current is disregarded. With method 2 the total current (diode + guard-ring + cut-edge) is measured. All measurements were done with the Keithley 487 and 6517 A current meters. An avalanche breakdown in the guard-ring region should also be visible with method 1, since the avalanche normally extends to the diode region. But method 2 has the advantage of indicating the whole current that has to be supplied by the bias voltage source. On the one hand this

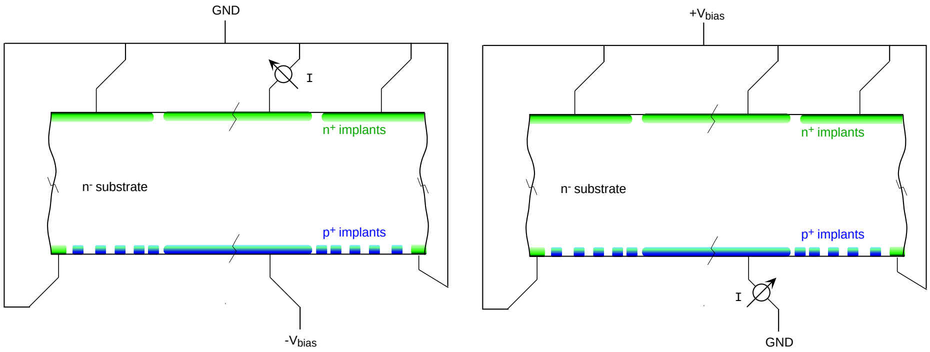

Figure 4.52: *Two different methods to take I-V curves of guard ring test-diodes. With the left setup only the diode current is measured (method 1), whereas the right setup takes also the guard current and the cut-edge generation current into account (method 2).*

is important for the detector design (power dissipation, cooling, …). The current difference between the two methods, on the other hand, allows to monitor the current through the periphery (guard rings + cut edge), which should be kept as small as possible.

Table 4.3: *Nomenclature for the guard ring designs.*

abbreviation	description	# guards	see figure
narrow	narrow distance to cut edge	10	3.8
middle	middle distance to cut edge	10	3.8
brick14	“brickwall” with bricks of p^+	14	–
brick28	“brickwall” with bricks of p^+	28	3.14
22×30	22×30 pixel with narrow guards	10	3.8
5×5	5×5 pixel with reduced guards	6	3.12

First, the devices under test were measured directly on the wafer. As an example the I-V curves of seven 22×30 pixel structures are displayed in figure 4.53. The I-V characteristic of a similar device after irradiation can be found in figure 4.33.

Then, they were cut, glued on a *PCB* and bonded. The irradiations were done at the CERN-PS accelerator (protons) and in the PSI πE1 beam (pions) under the conditions already described in the pixel isolation section 4.1.4, including the biasing during irradiation. After the irradiation the devices were stored in a refrigerator at +1°C.

In figure 4.54 one finds I-V curves of 5×5 pixel devices taken with methods 1 + 2 . As expected the leakage current is higher after irradiation (see

__Figure 4.53:__ Leakage current of seven 22 × 30 pixel sensors on the uncut wafer.

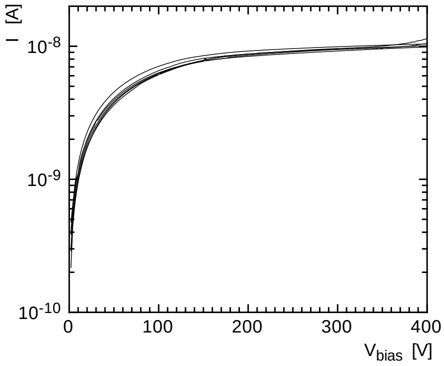

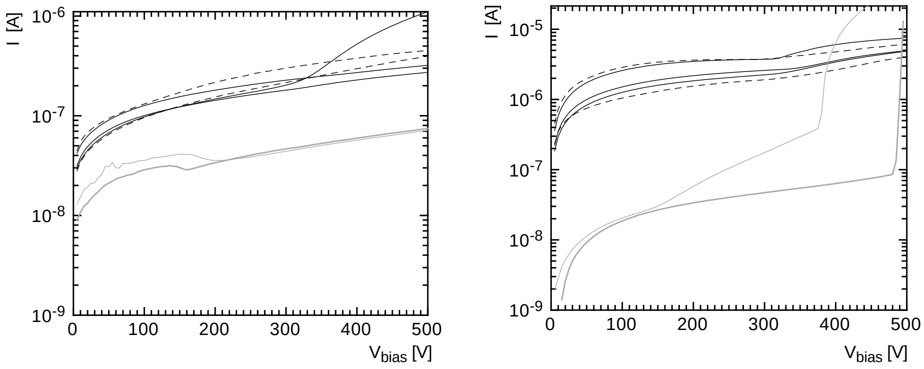

__Figure 4.54:__ Measurements of the I-V characteristics of 5 × 5 pixel devices to test their guard-ring designs. Left: method 1, right: method 2 (see figure 4.52 for an explanation). The light gray curves are from unirradiated sensors, the dashed ones were taken after 6.5·10^{14} π cm^{-2} and 28 weeks annealing at +1° C, the full, black curves denote I-V measurements taken after 5.3·10^{14} p cm^{-2} and 39 weeks annealing.

section 2.3). However, the breakdown voltage before irradiation is lower than after. One of the devices had a hard breakdown just below 500 V before irradiation, while the other one showed a weak breakdown (limited to a small volume of the sensor) before irradiation already at ∼150 V, which becomes more severe around 400 V. These breakdowns are visible only with method 2, probably because one occurs very close the maximum voltage of 500 V (with method 1 it would appear a little bit above 500 V) and the other one is spatially limited to a small volume in the guard ring area.

However, after irradiation with pions or protons these breakdown phenomena disappear. Only one device shows signs of a weak breakdown above ∼300 V. Again, there is no significant difference between the sensors irradiated with pions or with protons (see page 61). Furthermore, there is also no difference between 28 and 39 weeks annealing. This is in accordance with the results already presented in section 4.1.4.

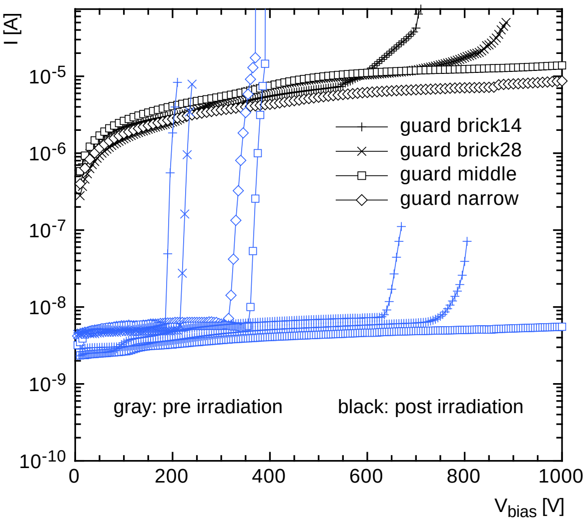

Figure 4.55: *I-V characteristics of the designs middle, narrow, brick14 and brick28 (method 2). The curves of the unirradiated devices are drawn in gray, the ones after a fluence of* $6{\cdot}10^{14}\,\mathrm{p\,cm^{-2}}$ *+ 10 weeks annealing in black.*

This "healing effect" after irradiation is even more pronounced for some of the guards in figure 4.55. There, several examples of the brick-wall-like (brick14 and brick 28), the narrow and the middle guard rings are plotted (see table 4.3 for explanations). All of them were measured with method 2. Before irradiation, but after cutting, four out of seven devices show a hard breakdown below 400 V (gray in figure 4.55). These four devices were chosen to be irradiated with protons to investigate the "healing effect" ($6{\cdot}10^{14}\,\mathrm{p\,cm^{-2}}$ + 10 weeks annealing). The resulting I-V characteristics for these four devices are shown in black in figure 4.55. Only the two brick-wall designs do have a breakdown below 1000 V. The standard guard rings, which also broke down below 1000 V before irradiation, are stable up to 1 kV now.

For this healing effect there exists no satisfactory explanation up to now. Similar observations were reported by other groups (see e. g., [32, 17]). Probably some impurities from the production process were responsible for the high electric field strengths before irradiation. After irradiation, the influence of these impurities on the electric field is smoothed by a higher defect density in general.

From figures 4.54 and 4.55 it can also be seen that, after irradiation beyond the type inversion fluence, the currents measured with method 2 are about one order of magnitude higher than the currents measured with method 1. This indicates generation currents from the guard ring area or even more likely from the cut edge (see figure 4.49). If this current increase is due to an encroaching of the depletion zone on the scribe line it would imply that the space between the last guard ring and the cut edge should be enlarged. However, in figure 4.55 there is no significant difference between the middle and the narrow guard rings after irradiation (the narrow one has even a slightly lower current than the middle one). Therefore, the current generation happens most probably only in a small volume close to the surface and not along the cut edge. This implies that the distance between the outermost guard ring and the scribe-line is sufficient in both cases, and that the differences between method 1 and 2 are due to generation currents in the silicon bulk below the guard ring area.

In addition, the measured guard ring current is still negligible compared to the pixel leakage current after irradiation. In a full module the main part of the current is drawn by the much larger pixel area (~42'000 pixels with 10 nA per pixel, leading to ~0.4 mA). The guard ring current, in comparison, is ~1 μA for the small test devices with ~1 cm circumference, which translates to a module guard current (circumference 16.1 cm) of ~0.016 mA.

4.4.3 Summary

Two guard ring designs were found which hold up to 1 kV after irradiation (the ones called middle and narrow, see table 4.3 and figure 3.8). This perfectly fulfils the requirements of the CMS pixel sensor. The breakdowns at voltages around 300 V before irradiation are no problem since the full depletion voltage before irradiation is around 150 V. The same conclusion also applies to the higher guard ring currents after irradiation.

4.5 Measurement of the Pixel Capacitance

The exact knowledge of the capacitance of one single pixel to the rest of the sensor is important for the read-out chip design. On the one hand it influences the noise performance of the analogue amplifiers. The capacitance dependent noise sources lead to an equivalent noise charge[19] which linearly depends on the detector capacitance (an introduction to noise theory can be found in [37, 49, 50]). On the other hand it may causes a signal crosstalk to other channels. Actually, such a crosstalk could even be used to reduce the number of read-out channels: with enough capacitive charge coupling it would only be necessary to read out every second channel. This is a standard practice for some silicon strip detectors.

In section 4.5.1 the pixel capacitance is calculated with the help of parametrised simulation results. Section 4.5.2 explains the measurement method and section 4.5.3 deals with the results, which are then discussed in section 4.5.4.

4.5.1 Capacitance Calculation

The capacitance can be numerically calculated by solving the three dimensional Poisson-equation (4.9) with appropriate boundary conditions. After full depletion the charge distribution in the silicon bulk is uniform (assuming that the doping is uniform[20]) and the Poisson-equation reduces to the Laplace-equation:

$$\nabla^2 V = \nabla \vec{\mathcal{E}} = 0 \quad . \tag{4.23}$$

From a known electric field distribution the surface charge distribution can be calculated by integrating $\varepsilon_{si}\varepsilon_{\circ} \int \mathcal{E}(x,y,0)\, dA$ over the surface at $x = 0$ (Gauss-integral, see e. g., [51]). With the requirement of charge neutrality one also obtains the backside charge. In [52] numerical solutions to this problem are parametrised with respect to the pixel size, the gap between pixels and the depletion width. These analytical expressions can be used to estimate the pixel capacitance, which is done in the following.

The total pixel capacitance can be divided into three different contributions (see figure 4.56): Each pixel has a pixel-to-backplane capacitance C_0. Each of the four nearest neighbours is capacitively coupled to the centre pixel by C_1, and all diagonal (next to nearest) neighbours by C_2. These capacitance contributions are all normalised to the one-dimensional parallel plate capacitance C_p, and all dimensions to the depletion depth x_n. The following

---

[19] Equivalent noise charge (ENC): The charge that would be necessary at the input of the amplifier stage to compensate the noise voltage at the output.

[20] As a simplification it is assumed that, after full depletion, all bulk and surface charges are fixed charges whose electric field component is independent of the bias voltage. Therefore they do not influence the capacitance.

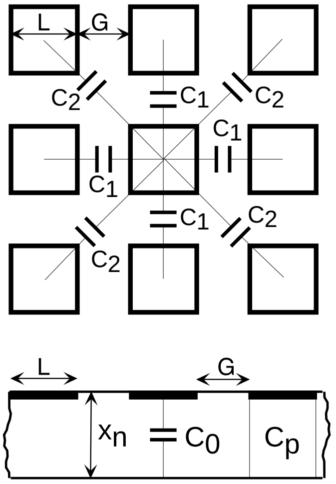

Figure 4.56: *Definition of parameters and capacitance contributions for the simulation.*

definitions will be useful: the normalised pixel side length $\lambda = L/x_n$, and the normalised gap between the pixel implants $g = G/x_n$. According to [52] these (numerically calculated) contributions can be expressed as:

$$\frac{C_0}{C_p} = 1.15^{1/\lambda} + \frac{2.3}{\lambda}\left[1 - \exp\left(-\frac{g}{\sqrt{\lambda}}\right)\right] \tag{4.24}$$

$$\frac{C_1}{C_p} = \frac{0.23}{g + 0.18}\left(\frac{1}{\lambda}\right)^{0.75} - 0.07\left(\frac{1}{\lambda}\right) \tag{4.25}$$

$$\frac{C_2}{C_p} = 0.1^{\lambda} \cdot \left[1 - 1.15\,g\left(\frac{7}{g+3} - 1\right)\right] \quad . \tag{4.26}$$

When all adjacent pixels are virtually grounded through the read-out chip the total capacitance of a single pixel is

$$C_{tot} = C_0 + 4C_1 + 4C_2 \quad , \tag{4.27}$$

with an estimated error of about 10 % [52].

In reference [52] equations (4.24) to (4.26) are plotted as functions of λ and g. For the CMS pixel detector the total pixel size (implant plus gap) will be 150 μm × 150 μm. But the separation of this area into n$^+$ implant and p-stop area is a free design parameter, which is only limited by the design rules of the production process. For the pixel isolation measurements in section 4.1 one was interested in keeping the ratio between the n$^+$and the p-stop area at a fixed value to obtain comparable results for the different p-stop designs. Therefore, all the designs described in section 3.1 have the same implant width. However, in figure 4.39 it was shown that the maximum electric field strength becomes smaller for narrower gaps between the pixel implants. The reverse is true for the pixel capacitance: it becomes larger for smaller gaps, as shown in figure 4.57 for two different pixel sizes. The capacitances were calculated with equation (4.27), assuming a parallel plate capacitance C_p of 300 μm thickness and a square surface-area of (150 μm − gap)^2.

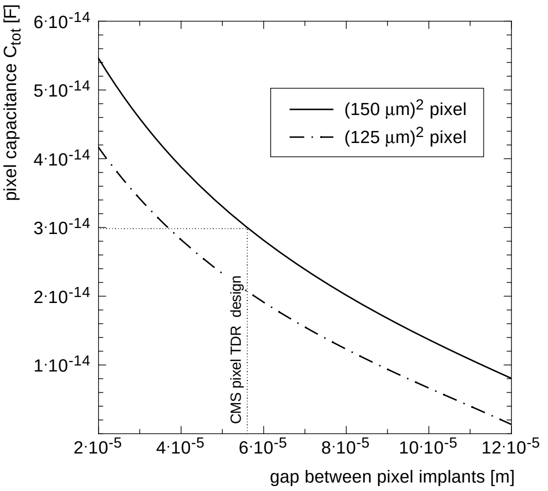

Figure 4.57: *Calculated pixel capacitance as a function of the gap between the implants for pixels with 150 μm and 125 μm side length.*

For the calculations in reference [52] data from square p^+-in-n pixels were used. Yet, in CMS the pixels consist of a n^+ implant in a n type bulk. Due to the electron accumulation layer the Si-SiO$_2$ interface is at the same potential as the pixel implant, unless the accumulation layer (and hence the electric contact) is interrupted by a p-stop ring. Therefore, the capacitively active region of one pixel is the area of the n^+ implant plus the n-type surface area between the implant and the first p-stop ring. For example, in the design proposed in the CMS Tracker Technical Design Report [4] the n^+ implant is 78 μm wide and the distance to the first p-stop ring is 8 μm (shown in figure 3.2). This leads to a parallel plate capacitor area of $(78+2\cdot 8)^2\ \mu\text{m}^2$. With a pixel to pixel distance of 150 μm the gap between the pixel capacitances becomes 56 μm. Using equations (4.24) to (4.27) one obtains a total pixel capacitance of $C_{tot} \approx 30$ fF. In figure 4.57 this calculated capacitance is marked.

4.5.2 Capacitance Measurement Method

Technically, it is extremely difficult to measure such a small capacitance. Therefore, 140 pixels were connected in parallel to reach a measurable capacitance value of a few picofarad. This is accomplished with the help of a parallel router chip, which was already described in section 3.1 (see figure 3.15). The capacitance was measured with the HP 4284 A capacitance meter, and the bias voltage was delivered by the voltage source of the Keithley 487.

The measurement setup is shown in figure 4.58. The parallel router chip was bump bonded to a pixel sensor with a standard, double p-stop pixel design (see figure 3.2). The whole setup was then placed on a grounded, gold plated *PCB* laying on a chuck in a shielded probe station. The two pads of the parallel router chip were contacted with probe needles. Through the bump bonds they also provided the ground potential of the pixel sensor. The backplane of the pixel sensor was contacted with a third probe needle to apply the bias voltage.

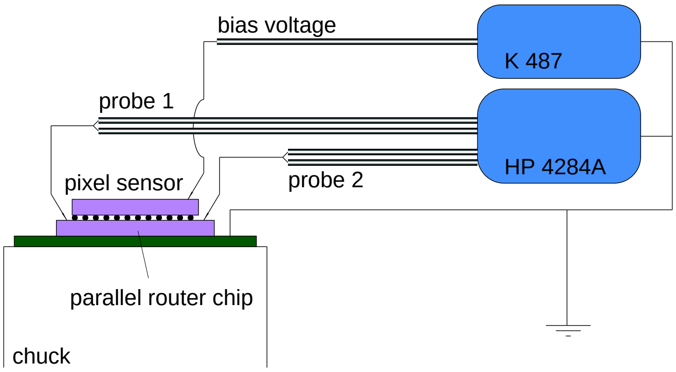

Figure 4.58: *Setup for the pixel capacitance measurement (housed in a probe-station).*

In order to accurately measure picofarad capacitances much attention must be paid to reduce parasitic effects. The two probes were connected to the capacitance meter with coaxial cables of equal length. The cable and probe capacitances were automatically subtracted by using the open and short circuit correction facility of the HP 4284 A (measured at different frequencies and averaged). The small capacitances lead to high impedances $Z_c = (\omega C)^{-1}$. This means that the parallel parasitic resistances influence the measurement results more than the serial parasitic resistances. Therefore, the parallel resistance mode of the HP 4284 A was chosen (with an AC signal of 0.1 V).

The parasitic capacitance contribution of the parallel router chip was also measured alone: one of these chips without a sensor attached to it (but with already reflowed bumps) was investigated on the same setup. Averaged over 6 different frequencies between 5 kHz and 1 MHz, this contribution was (10.44 ± 0.03) pF, where the error is only statistical. The systematic error is estimated to be about 0.2 pF (with different measurements of commercial ceramic capacitors with the same setup). The same measurement was also performed with a dummy pixel sensor placed on the parallel router chip with narrow, 60 μm thick capton pads in-between (in such a way that the pixel area was not covered by capton). Within errors the capacitance with this setup was the same as with the naked router chip alone.

4.5.3 Capacitance Results

The measured capacitance of the 140 pixels in parallel - after subtraction of the parasitic capacitances of the parallel router chip - are displayed in figure 4.59 as a function of V_{bias}. The measurements were performed for seven different frequencies, to filter any frequency dependent distortions. For bias voltages blow the full depletion voltage V_{FD} the pixels are short-circuited and no reliable capacitance can be measured. However, in figure 4.59 the capacitance is only independent of the sensor bias voltage for $V_{bias} > 190\,\mathrm{V}$, even if the full depletion voltage was around 160 V. This can be explained as follows:

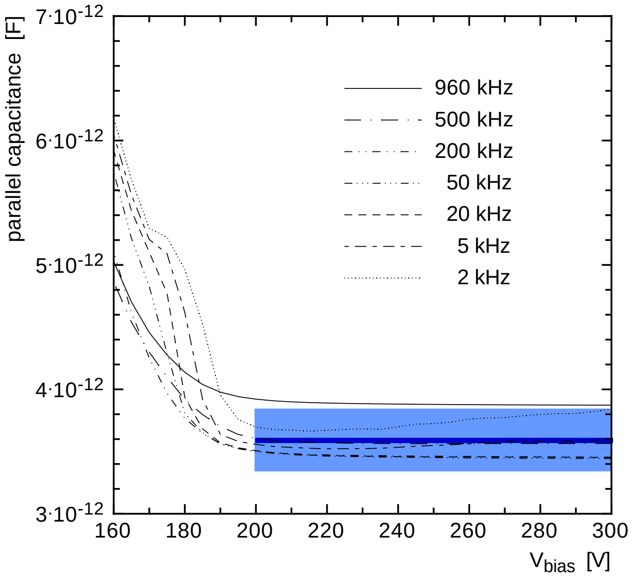

Figure 4.59: *Total capacitance for 140 pixels in parallel for different measurement frequencies after subtraction of parasitic capacitances. The gray bar denotes the average value and its error.*

Figure 4.60: *Measured parallel parasitic resistances of the 140 pixels and leakage currents (inset) as a function of bias voltages. The vertical line at 190 V shows the point where the p-stop channels get pinched off.*

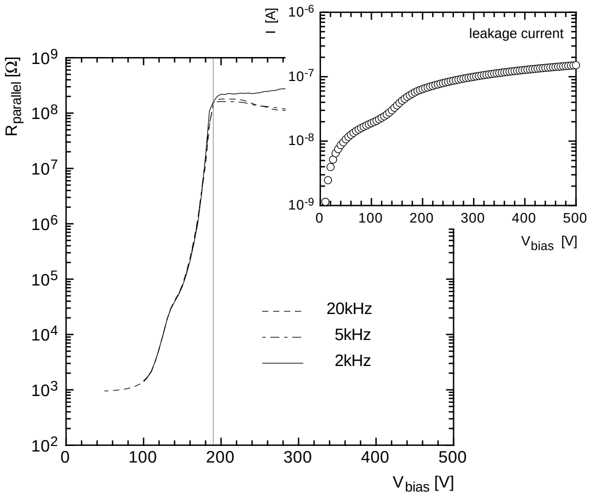

Even above V_{FD} the pixels are resistively connected through the labyrinth of the open p-stop rings. These resistive channels are only pinched off (interrupted) at bias voltages much higher than V_{FD}, as shown in section 4.1. In figure 4.60 the measured parasitic parallel resistances for a few frequencies are shown as a function of bias voltage. For voltages lower than 190 V the parallel resistance rapidly varies with bias voltage, but remains constant above 190 V . This implies that it is extremely difficult to measure a reliable capacitance below 190 V. For this reason only capacitance values for $V_{bias} \geq 200$ V were taken into account. The mean value in the bias voltage interval 200 V $\leq V_{bias} \leq$ 300 V and for all frequencies in figure 4.59 is

$$(3.59 \pm 0.15 \pm 0.20)\,\mathrm{pF} \quad , \tag{4.28}$$

where the first error denotes one statistical standard deviation and the second the systematic error (derived by measuring commercial capacitors). Dividing this result by 140 leads to

$$C_{pixel} = (25.7 \pm 1.8)\ \mathrm{fF} \quad . \tag{4.29}$$

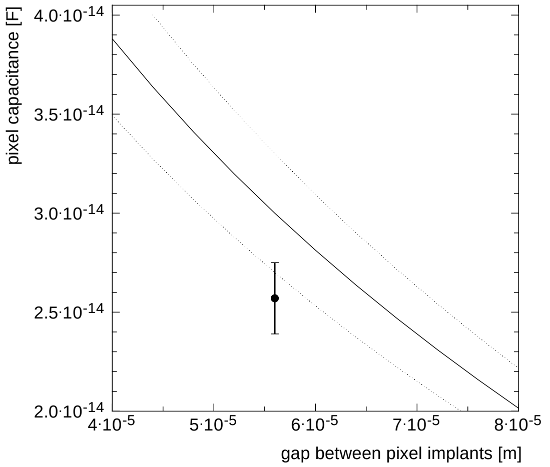

Figure 4.61: *Measured pixel capacitance compared to the calculation from figure 4.57. The calculations estimated error of ~10 % is also shown.*

In figure 4.61 this result is compared to the calculation of section 4.5.1 for pixels with 150 μm side length (figure 4.57). The measured capacitance value is slightly below the calculation. But taking into account the simplicity of equations (4.24) to (4.27) and that they do not include any information about doping densities or oxide thicknesses the agreement is still amazingly good.

4.5.4 Discussion

In order to find out what the capacitance result (4.29) means in terms of amplifier noise some more thoughts are necessary.

After 10^5 Gy the available signal charge will be about 12'000 e^- (assuming a half depleted sensor[21], see [4]). Therefore, the maximal threshold should be

---

[21] A minimal ionising particle in silicon normally creates about 80 e-h pairs per μm.

below 10'000 electrons. Requiring a signal to noise ratio of at least five, the maximally allowed noise is $ENC \approx 2000\,\mathrm{e}^-$, which is by far above the experimentally found value of $(840 \pm 180)\,\mathrm{e}^-$, [49], measured with an irradiated read-out chip and an unirradiated, 80 fF test diode as sensor.

In addition to the measured $840\,\mathrm{e}^-$ also the leakage current of the sensor will contribute to the noise. The leakage current per pixel after 10^5 Gy of hadron irradiation is on average roughly 10 nA. However, the distribution has tails up to 100 nA, which have to be absorbed by the input amplifier [4]. For shaping times comparable to the LHC bunch crossing time of 25 ns this leads to a charge flow of $\sim 15'000\,\mathrm{e}^-$. Assuming that the charge carriers are independent, Poisson statistics can be applied and the additional contribution of the leakage current to the equivalent noise charge is $ENC_{leak} \lesssim \sqrt{15'000}\,\mathrm{e}^- \approx 120\,\mathrm{e}^-$.

Concluding from this arguments one can say that a) the leakage current makes only a minor contribution to the noise, and that b) the pixel capacitance of 25,7 fF can still be increased by at least a factor of three without impairing the operation conditions of the pixel detector system after irradiation. And even with a threefold increased pixel capacitance the capacitive coupling to the neighbouring pixels would still be negligible[22].

Bearing in mind the results of section 4.2 (dealing with the electric field strengths between pixels) and the results of the capacitance simulation on page 99 the conclusion would be to shrink the gap between the n^+ pixel implants by up to a factor two. This would reduce the high surface field strengths between the pixels and reduce the strong nonlinear variations of the field strength perpendicular to the surface. It would also increase the pixel capacitance, which would however remain in the tolerated limits.

---

[22] Using equation (4.25), the relation $C = Q/V$ and assuming a threshold of $\sim$ 5000 electrons, a voltage step $> 50\,\mathrm{mV}$ would be necessary to trigger a neighbouring pixel.

4.6 Tests with Bump-Bonded Assemblies

Pixels whose connection to the read-out chip fail charge up and probably cause stochastic discharges. Such discharges were observed in earlier tests [7]. The atoll-like p-stop rings were introduced to avoid these discharges (see section 4.1). However, in section 4.1.4 the inter-pixel resistance was found to be much higher than expected after irradiation. The question to be answered in this section is whether the atoll p-stop design is nevertheless able to prevent stochastic discharges.

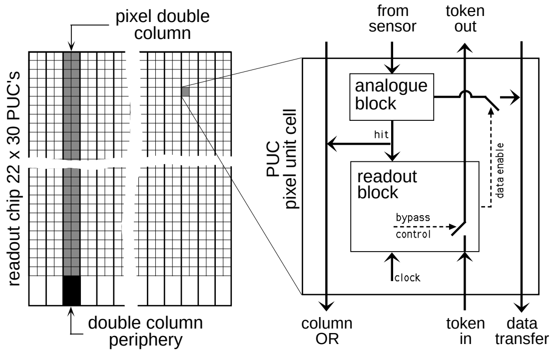

Figure 4.62: *A schematic view of the PSI 34 read-out chip.*

For this purpose three 22 × 30 pixel sensors were irradiated at the CERN-PS accelerator with $6 \cdot 10^{14}\,\mathrm{p\,cm^{-2}}$ (see section 4.1.4 for more details on the irradiation) and bump bonded to unirradiated PSI 34 read-out chips. The chip is described in detail in the references [4, 49]. It is a simplified version of the final CMS pixel read-out chip, which was accomplished for testing purposes. A brief summary of its functionality is given below in section 4.6.1. Section 4.6.2 deals with a beamtest at CERN and section 4.6.3 treats following laboratory tests with the same assemblies. The results are briefly summarised in section 4.6.4.

4.6.1 The PSI 34 Read-Out Chip

The PSI 34 chip is a 22 × 30 pixel chip for $150 \times 150\,\mu\mathrm{m}^2$ pixels, which is produced in the radiation hard DMILL SOI technology[23]. The basic building blocks are outlined in figure 4.62. The pixels are grouped in 2 × 30 pixel double columns, with a common bus to a double column periphery. Each pixel has its pixel unit cell (PUC), which consists of an analogue and a digital block. All of them are equipped with a comparator with an individually adjustable threshold. Whenever a PUC detects a signal height above threshold it stores the analogue signal in a capacitor and notifies the double column periphery, which immediately copies the time stamp into a memory

---

[23] SOI: Silicon on Insulator, a technique to reduce the silicon volume which is sensitive to radiation defects; DMILL: a radiation hard CMOS process, which is provided by the ATMEL company.

and asks for read-out. A read-out token is then sent through the whole chip and all double columns with hits are read out. All analogue signals of a hit double column are daisy-chained to the data line and linked with the time stamp (3 analogue signals, to have enough dynamic depth) and a double column address (1 analogue signal). Therefore, 64 analogue signals arrive at the ADC for each hit.

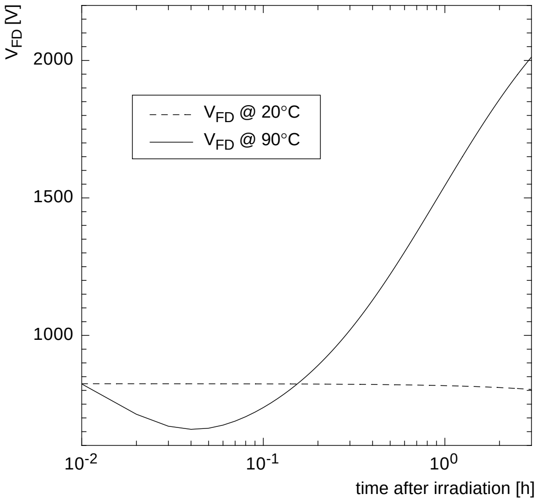

Figure 4.63: *Simulated influence of the annealing on V_{FD} for different temperatures (after $\Phi = 6 \cdot 10^{14}\,p\,cm^{-2}$; the dashed curve corresponds to figure 2.10).*

4.6.2 Beamtest at CERN

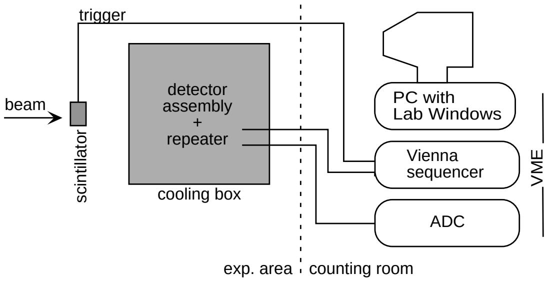

Figure 4.64: *Schematic view of the setup used in the beamtest.*

By mistake the irradiated sensors were heated to 90°C for one hour during the bump bonding process. This accelerated the annealing (beneficial and reverse) by a factor of roughly 20'000, which lead to a full depletion voltage of about 1500 V [24] (calculated with a model from [20], see figure 4.63) and a much increased leakage current . On the one hand this reduced the signal charge, since the maximal voltage of the available voltage source (Keithley 487) was 500 V. The high current, on the other hand, caused the detector to be very noisy, which made the detection of real hits difficult.

---

[24] Before irradiation the full depletion voltage was 140 V, see table 3.2.

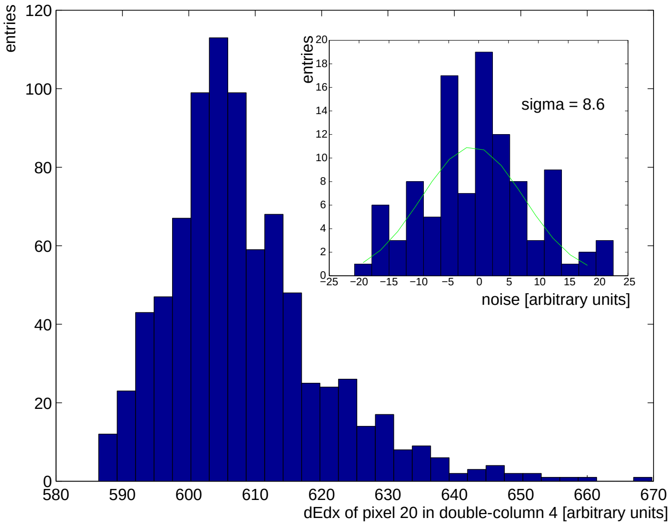

Figure 4.65: *Landau-distribution of a single, unirradiated pixel and the corresponding noise.*

Nevertheless, the detectors were brought to a beamtest at CERN. A sketch of the setup is displayed in figure 4.64. No beam-defining telescope (e. g., [53]) was used because parameters that require tracking, like spatial resolution or the Lorentz-angle, had already been measured in former beam-tests (see e. g., [9, 54, 55, 56]). The test took place in summer 2000 at CERNs SPS accelerator, with 220 GeV/c pions from the secondary H2 beamline. The readout control was done with a specially built sequencer [57]. The detectors were kept at $-5°$C by Peltier cooling during the test.

Figure 4.65 shows a Landau distribution of an unirradiated pixel. The mean energy value corresponds to a signal charge of 24'000 electrons. This was the proof that the read-out system worked correctly. From figure 4.65 a signal to noise ratio of ~70 could be deduced. For several unirradiated detectors the signal to noise varied between ~50 and ~100 in these tests.

The collected sample of reconstructed hits in the irradiated detectors was too small for a Landau distribution (because of the high noise and the low signal charge). In figure 4.66 such a hit is displayed. The continuous line shows the contents of the analogue cells of one daisy-chained double column. The first analogue signals (up to count 8 on the horizontal axis) consist of the three time stamps of the hit and its double-column address. The analogue values of the 60 pixels of a double column are displayed above $x = 9$. The dashed token at the bottom indicates a pixel with an analogue signal above threshold (the so called "digital out"). At $x = 42$ an (negative) analogue signal can be seen, confirmed by it is "digital out". In order to be recognised as a hit, a signal had to lie $5\,\sigma$ above the mean pedestal of all analogue values in its double column. In addition, a confirming "digital out" was also required.

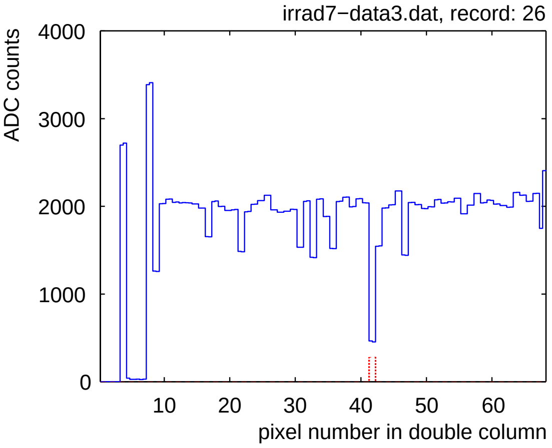

Figure 4.66: *Output signal from the PSI 34 chip with an irradiated sensor, showing a (negative) signal at* $x = 42$ *(corresponds to pixel 34).*

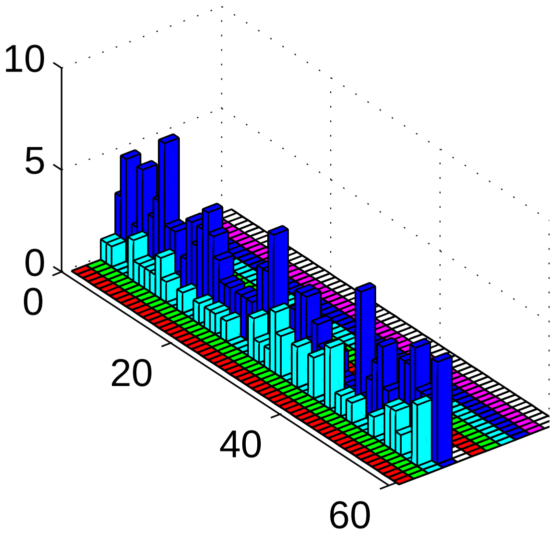

Figure 4.67: *Hit occupancy of an irradiated detector. Only the columns 3 and 4 were activated.*

The total number of reconstructed hits during a runtime of seven hours is shown in figure 4.67 as an occupancy-plot. Only two double columns (three and four) were activated. For non of the pixels in these two double-columns more than six hits could be reconstructed during that run.

With such low statistics and high pedestal variations it is very difficult to make any comment concerning possible stochastic discharges. Nevertheless, the fact that signals could be seen at all after the overheating-accident proves the capability of this detector system to be useful even in a worst case scenario (e. g., after an accelerator beam loss in the detector, when several proton bunches hit one single module).

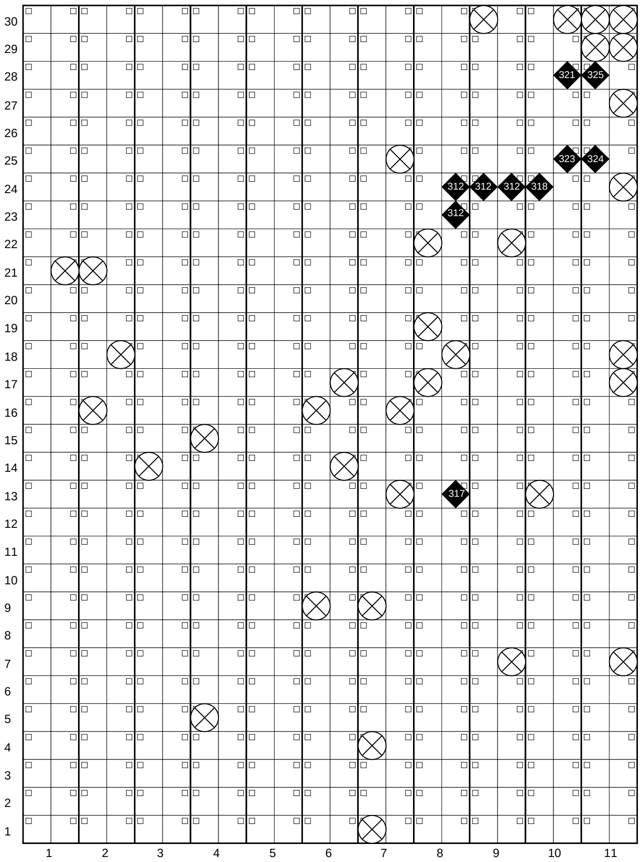

Figure 4.68: *Missing bonds ($\bigotimes$) and noisy pixels (♦) with their breakdown-voltages (in volts) for an irradiated sensor with open double p-stop rings.*

4.6.3 Laboratory Tests

In order to further investigate the discharge behaviour of irradiated detectors additional measurements were performed in the laboratory. First, we looked for unbonded pixels and, in a second step, detected early breakdown regions. In figure 4.68 these two characteristics are displayed for an open, double p-stop ring sensor (see figure 3.2) on a 22 × 30 pixel floorplan. The missing bumps (labelled with $\bigotimes$) were determined with backplane-pulsing: a small step pulse $dV = 2.6\,V$ was superimposed on the bias voltage V_{bias}, which was applied on the sensors backside. Due to the capacitive coupling through the depletion region such a pulse induces a small charge flow on all pixels: $dQ = C_s \cdot dV$, where C_s stands for the depletion region capacitance. This signal is then recognised by the read-out chip, provided that the corresponding read-out channel has a working indium bump connection to the sensor. When a read-out channel was working with a calibration pulse, but did not respond to the backplane pulse, the corresponding bump bond was assumed to be bad. The breakdown regions (labelled with ♦) were found by looking at the noise of the pixels in the read-out chip as a function of V_{bias}. Breakdown was assumed when a pixel went into permanent saturation. All measurements were carried out at $T = -25°\mathrm{C}$.

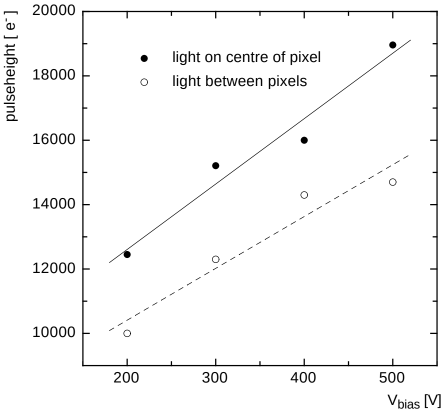

Figure 4.69: *Pulse heights obtained with an IR-laser pointing at the centre of a pixel and at the gap between two pixels. The sensor of figure 4.68 was used for this test.*

None of the pixels which showed an early breakdown had a missing bond! Furthermore, there seemed to be no correlation between missing bonds and breakdowns. The pixels with an early breakdown worked properly at voltages below the breakdown voltage, and all of them broke down between 310 and 330 V. Similar results were obtained for two other irradiated devices (both with an exceeded thermal budget, too). This indicates that the breakdowns were not due to unbonded pixels. They were caused by impurities or defects between the n^+ pixel implants and the p-stops. The electric field strength reaches a maximum in this region (see figure 4.37), which is further increased by the electron accumulation layer. At low bias voltages such defects are not vexatious, but above 300 V they cause micro discharges which lead to local avalanches. Obviously, the open, atoll-like p-stop rings fulfilled their task in spite of the high inter-pixel resistance after high-dose irradiations.

Additional measurements on the irradiated detectors were made with the help of an infrared laser spot. The aim was to investigate the charge collection efficiency of an irradiated sensor with open p-stop rings. A 1064 nm Nd-laser was used for these tests. The absorption coefficient in silicon for this wavelength is about $10\,\mathrm{cm}^{-1}$ [58]. Therefore, the electron-hole pair creation by the the absorption of the photons can assumed to be equally distributed in the silicon bulk. The pulse heights obtained with the laser pointing at the centre of a pixel and in the gap between two pixels (summed pulse heights) is shown in figure 4.69 as a function of the applied bias voltage ($T = -25°\mathrm{C}$). As a comparison, the signal charge in an irradiated sensor ($\Phi = 6.3 \cdot 10^{14}\,\mathrm{cm}^{-2}$) at $V_{bias} = 300\,\mathrm{V}$ was measured to be $\sim 10'000$ electrons [7]. The straight lines in figure 4.69 are linear regressions through the measured points. The average ratio between the two pulse heights is 0.82, which means that the charge collection efficiency is reduced by a factor of 0.8 when a traversing particle hits the detector between two pixels. This is not fatal since there is still enough charge for the read-out amplifier (the threshold will be set at a few thousand electrons, and a *MIP*[25] creates about 24'000 electrons in 300 μm silicon). Nevertheless, if there is a possibility the fraction of 0.8 should be improved.

In section 4.2 we found that there are zones of low electric field strength between the pixels when the sensor is not over-depleted. These low-field zones are also responsible for the reduced charge collection efficiency between the pixels in the irradiated sensor. The low field zones can be diminished by shrinking the gap between the n^+ pixel implants. This would also lead to an increase of the charge collection efficiency between the pixels. As we have seen in section 4.5, a reduction of the n^+ implant gap would also be tolerable with respect to the pixel capacitance.

4.6.4 Summary

- ➢ Unbonded pixels in irradiated sensors with open p-stop rings do not show any stochastic discharges, in spite of the high inter-pixel resistance after irradiation. Such sensors could even be read out after a 20'000 times accelerated annealing during one hour due to accidental heating.
- ➢ In some pixels micro-discharges occur above $V_{bias} = 300\,\mathrm{V}$, but they are not correlated with unbonded pixels. These discharges are most likely due to defects or impurities close the the p-stop implants. However, since the CMS pixel sensor will probably have to be operated at $V_{bias} > 300\,\mathrm{V}$, one should keep this micro-discharges in mind for the choice of the final production process.

---

[25] Minimum ionising particle: a particle with $v \approx 0.96\,c$, where the ionising energy loss in matter has a minimum (according to the Bethe-Bloch formalism).

4.7 Measurement of the Lorentz-Angle after Irradiation

The following measurements are published in Nuclear Instruments and Methods in Physics Research A [55].

4.7.1 The Lorentz Effect

Due to the electric field $\vec{\mathcal{E}}$ the charge carriers produced along the track of a traversing particle drift to the corresponding electrode. A magnetic field $\vec{B} \not\parallel \vec{\mathcal{E}}$ causes a Lorentz-force and hence the charge carriers do not drift along the electric field any more. This Lorentz-effect distributes the charge carriers to several strips or pixels. The charge sharing can be used to calculate the centre of gravity of the charge distribution which improves on the traversing charged particles track information.

Consider a charged particle drifting in constant electric and magnetic fields. The resulting force on the particle is

$$\vec{F} = q \cdot (\vec{\mathcal{E}} + \vec{v} \times \vec{B}) \tag{4.30}$$

where v is the drift velocity and q the elementary charge. When the scattering relaxation time τ_s (the average time between two phonon- or impurity-scatterings) is long enough the particle performs a circular motion (cyclotron motion) with $\omega_c = qB/m^*$, where m^* denotes the effective particle mass (condition $\omega_c \tau_s \gg 1$). However, if $\omega_c \tau_s \ll 1$ the particle "forgets" its history with each collision and performs a random walk with an averaged net velocity in the direction of $\vec{F}$. If $\vec{B}$ is perpendicular to $\vec{\mathcal{E}}$ the carriers drift at an angle Θ_L (Lorentz angle) with respect to the direction of the electric field

$$\tan(\Theta_L) = \mu_H \cdot |\vec{B}| \quad . \tag{4.31}$$

The Hall mobility μ_H is related to the drift mobility via

$$\mu_H = r_H \cdot \mu \quad , \tag{4.32}$$

where r_H is of the order of unity[26]. The factor r_H represents the influence of the magnetic field on the scattering relaxation time τ_s.

The Hall factor r_H normally depends on the carriers energy states and on the scattering mechanisms involved. There are some models for analytical calculations (see e. g. [12]), but in most cases of applications of semiconductors r_H has to be measured or evaluated numerically with Monte Carlo techniques. Some values for r_H for different temperatures and doping concentrations are given in [59]. For electrons in n-type silicon ($N_D = 1.75 \cdot 10^{14}\,\mathrm{cm}^{-3}$) and holes in p-type silicon ($N_A = 3.1 \cdot 10^{14}\,\mathrm{cm}^{-3}$) it is [59] stated that

$$r_H^n = 1.15 \quad \text{and} \quad r_H^p = 0.72 \quad . \tag{4.33}$$

---

[26] r_H is also related to the Hall coefficient R_H used for the Hall effect: $R_H = r_H/(n_0\, q)$, where n_0 is the density of carriers.

4.7.2 Irradiation Effects

In highly irradiated silicon sensors the drift properties are affected by radiation induced lattice displacements. In particular they are influenced by the change of the effective doping, by the increased depletion voltage and by trapping effects.

The change of the effective doping concentration under irradiation $N_{\mathit{eff}}(\Phi)$ with fluence Φ was subject to many investigations and is quite well understood. A summary and a description of the important parameters can be found in [20]. A key result is that, after type inversion has occurred, the effective doping concentration increases linearly with the flux.

Due to the increased doping concentration after type inversion a higher reverse bias voltage is needed to maintain a reasonable depletion depth. The resulting higher electric field reduces the mobility such that

$$\mu(\mathcal{E}) = \frac{\mu_n}{\left(1 + \left(\frac{\mathcal{E}}{\mathcal{E}_c}\right)^{\zeta}\right)^{1/\zeta}} \quad , \tag{4.34}$$

with μ_n being the mobility at low electric fields; $\mathcal{E}_c$ is a normalisation parameter depending on the material and $\zeta = 1$ is used for holes and $\zeta = 2$ for electrons [60]. However, this formula can not be easily adapted to the Hall mobility, e. g., it is well known that the Hall mobility becomes less dependent on the electric field with increasing magnetic field strength [15]. Moreover, the magnitudes of the high field effects depend on the orientation of the fields with respect to the crystal lattice. In [15] and in the references quoted therein some theoretical considerations about the Hall mobility are made. Measurements and numerical calculations dealing with these subjects can be found in [61].

Trapping effects lead to a decrease of the number of charge carriers. But from the electrical point of view trapped charge remains active. Since the preamplifiers are charge sensitive, they are also sensitive to image charge induced by trapped carriers.

4.7.3 Experimental Principle

In order to avoid a measurement of the Lorentz-angle depending on cluster-formation or an underlying charge carrier dependent model a method was chosen which determines the angle only using trigonometric relations.

To experimentally determine the Lorentz angle a method relying only on trigonometric relations was chosen. This grazing angle method [62] was developed in order to determine the depletion depth profile of irradiated silicon pixel detectors, alternatively to the commonly used C-V measurement.

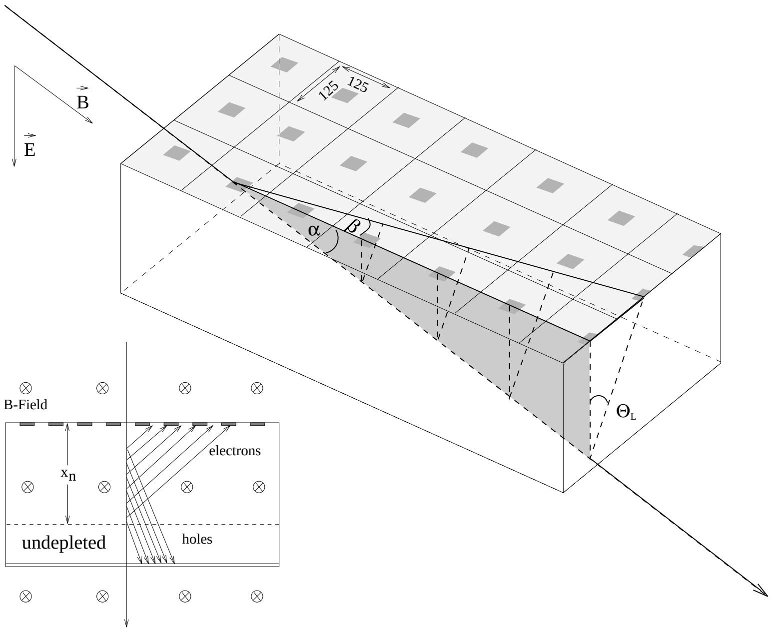

__Figure 4.70:__ The upper figure shows a three-dimensional section of the pixel detector with a traversing particle. α is the grazing angle and β parametrises the mean arrival position of the electron cloud. Knowing these two angles the Lorentz-angle Θ_L can be calculated. The front view of the detector below shows the drift directions of electrons and holes from different bulk-depths.

The principle is shown in figure 4.70. Ionising particles, traversing the detector under a very shallow angle α, generate signals which can be seen on a line of pixels forming a "signal-street". Each pixel in the line collects charge from a given segment of the traversing particles trajectory and hence from a given depth segment in the bulk. The signal ends at the pixel row under which the particle leaves the detector or enters the undepleted region (at depth x_n). The latter applies mostly to the irradiated case when the full depletion voltage would exceed the breakdown voltage.

With a magnetic field perpendicular to the electric field the drifting charge carriers are deflected by the Lorentz-force. They reach the surface with a displacement proportional to their drift length. Therefore, Pixels near the end of the "signal-street" are expected to share some charge with the adjacent pixel rows. From the angle of incidence of the traversing particle (α in figure 4.70) and form the deflection distance $y = x_n \cdot \tan \Theta_L$ it is possible to obtain the Lorentz-angle directly. Due to the linear dependence of y on the charge creation depth Θ_L can be parametrised by a single angle (β in figure 4.70). This then leads to the simple equation

$$\tan \Theta_L = \frac{\tan \beta}{\tan \alpha} \quad . \tag{4.35}$$

4.7.4 Experimental Setup

For the measurements mentioned above two silicon pixel detectors were available. They consisted of 256 n-type pixels (8 rows à 32 pixels) in a 280 μm thick low resistive n-type bulk. The pixel dimensions were 125 μm × 125 μm, isolated with a closed, 8 μm thick p-stop ring. The full depletion voltage was measured to be -123 V, the bias voltage applied for the measurements was -144 V. A more detailed description of the devices can be found in [7]. For the readout the 256 pixels were routed with metal connections to wire bond pads. The readout was done with two APC-128 analogue readout chips [63].

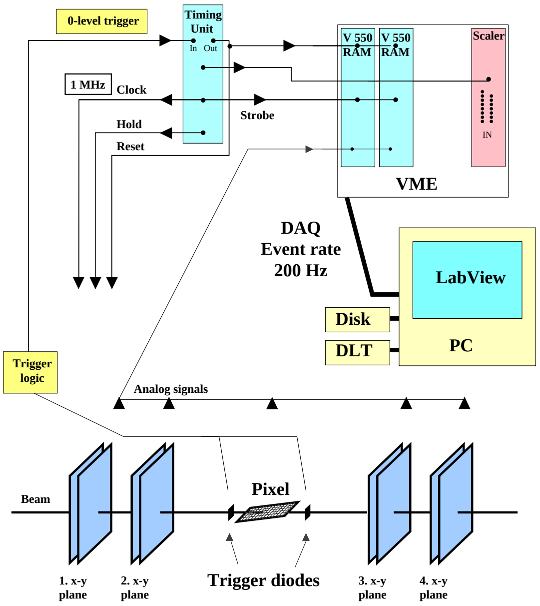

__Figure 4.71:__ The setup of the beam-test with the pixel detector in the middle of the four x-y planes of the telescope. The overall length was about 60 cm.

One of the detectors was then irradiated with $6 \cdot 10^{14}$ pions per cm^2 and annealed for more than a year in a cooled environment (+ 1°C). This device was also kept cool during the measurements. After the irradiation the n-bulk material had converted to p-type which means that the depletion zone was growing from the pixel side. Therefore, this detector was still operational after irradiation even when it was only partially depleted. The bias voltage applied was -256 V which led to a depletion zone of 160 μm. The full depletion voltage was calculated to be around 800 V.

In order to obtain information about the track positions a beam telescope built by the University of Zürich was used. Four layers consisting of two crossed silicon strip detectors each led to a spatial resolution of less than 1 μm. The strip detectors (32 × 32 mm^2 of size) had a 50 μm readout pitch. For the readout VA2 chips were used with a shaping time of 2.3 μs. More details about this telescope can be found in [53, 56].

For the grazing angle measurement the pixel detectors were tilted by $\alpha = 8°$

with respect to the horizontal beam axis. As a trigger two silicon diodes were placed in front and behind the pixel detectors (see figure 4.71). A Lab-View controlled VME crate was used for the data acquisition. In order to have good statistics for the alignment the trigger diodes could be switched to logical "or". The data taking was done with both in coincidence.

The experiment was performed at the CERN SPS accelerator ring using 225 GeV/c pions. The trigger rate achieved was about 100 Hz. Two superconducting Helmholtz coils provided a longitudinal magnetic field of up to 3 Tesla.

4.7.5 Analysis

First, the data alone were searched for typical signatures of pixel-streets which were then used to align the pixel detector relatively to the telescope. In a third step the telescope impact information was taken into account and finally the angle β was extracted.

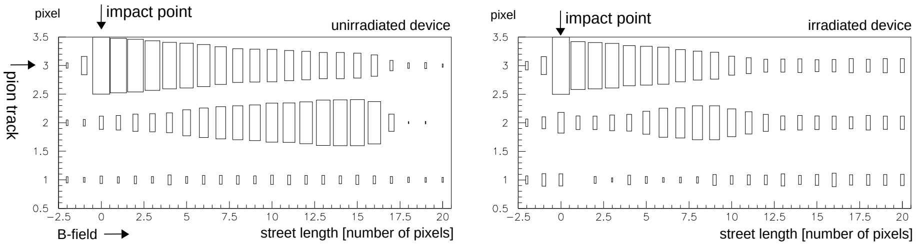

Figure 4.72: *Left: accumulated street signals in the unirradiated detector, one pixel per bin, impact point on the left, magnetic charge deflection downwards; right: the same plot generated with data from the irradiated detector.*

Figure 4.72 shows the pixel-streets. Here a few hundred events were superimposed and aligned according to their impact pixel. The impact point is located on the left. The B-field vector pointed from left to right, which led to a downward deflection. The pixels on the right of the signal street had the longest drift-path and hence the biggest deflection.

Figure 4.73 shows the same data as figure 4.72 but with a finer binning for the impact point. The horizontal axis is the same as in figure 4.72 whereas the vertical axis only covers two pixels (in units of μm).

For the analysis only equation (4.35) was applied. The angle of incidence of the traversing particle (α) was measured using the projection of the pixel detector onto the telescope detector plane. All the telescope entries which had a corresponding pixel entry were recorded. With the knowledge of the physical dimension of the pixel detector the angle α could be obtained from the the telescope information. Afterwards the angle α was cross-checked with a vertical laser beam reflected from the surface of the pixel detector. The

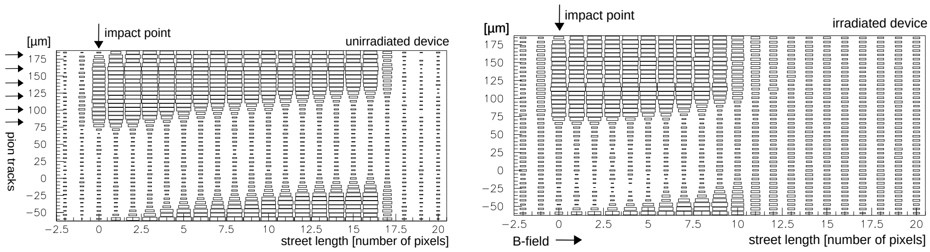

Figure 4.73: *The same picture as in figure 4.72 but with the telescope impact information included; left: unirradiated detector ($V_{bias} = -144\,V$, $T = 20°C$, $B = 3$ T); right: irradiated detector ($V_{bias} = -256\,V$, $T = -3°C$, $B = 3$ T).*

result for α was $(7.63\pm0.03)\,°$ in the unirradiated case and $(5.93\pm0.07)\,°$ in the irradiated one.

For the angle β the charge distribution asymmetry

$$A = \frac{Q_n - Q_i}{Q_n + Q_i} \quad \in [-1, 1] \tag{4.36}$$

was calculated for each pixel of a signal street, where Q_i stands for the charge collected by pixels of the impact pixel street and Q_n for the charge deflected to its neighbour. For $A = -1$ all charge carriers drifted parallel to the E-field and were collected by the impact pixel row. A value $A = +1$ corresponds to the case where all charge carriers were collected by the neighbouring pixel. Therefore, the interval $A = [-1, 1]$ corresponds to a full pixel pitch of $125\,\mu$m. In figure 4.74 the values for the +3 T data are plotted versus the street length for the unirradiated and the irradiated detector. The angle β of equation (4.35) was obtained by fitting a straight line to the data. In order to decrease the systematic error the values of β at symmetric B fields ±2 T and ±3 T were averaged in the unirradiated case. Due to technical problems only data for +3 T were available for the irradiated device.

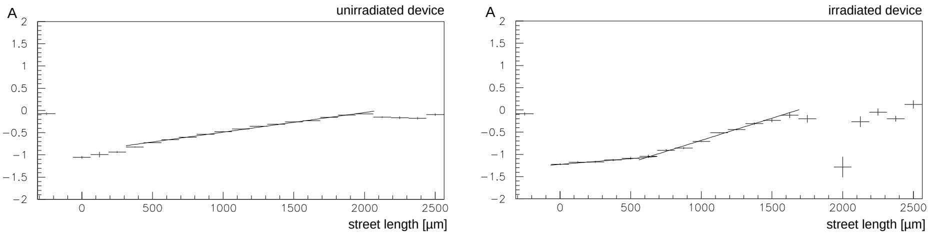

Figure 4.74: *Charge asymmetry A along a pixel street according to equation (4.36).*

In figures 4.73 and 4.74 it can be seen that for the unirradiated device the charge sharing is linear as a function of street length (which in turn is proportional to the depth of the released charge carriers). The results are given in table 4.4. However, the situation seems more complex for the irradiated device, since the first part of the pixel street (originating from the bulk area close to the surface) indicates a reduced charge sharing compared to the second part (which comes from the deeper bulk-area). This different behaviour must be attributed to the changes in the device that occur after type inversion, where the effective doping N_{eff} increases and other effects like charge trapping arise The change of N_{eff} together with a limited bias voltage may also lead to low field regions close to the surface between pixels and therefore modify the detailed charge sharing pattern due to the Lorentz-effect. Less distinctly, such effects may have already been present in the unirradiated sample. This is why the first three data points in figure 4.74 were not used for the fit.

For the analysis of the irradiated device we used two straight line fits (figure 4.74 right) leading to two extreme values for the Lorentz-angle. In table 4.4 the results are shown. They refer to the conditions prevailing during the run.

Table 4.4: *Lorentz-angle values of unirradiated and irradiated sensors for different magnetic fields.*

B-field	Θ_L unirradiated	Θ_L irradiated
2 T	$(12.8 \pm 1.3)^\circ$	-
3 T	$(18.2 \pm 1.2)^\circ$	$(6.2 \pm 3.0)^\circ \leq \Theta_L \leq (26.8 \pm 3.6)^\circ$

4.7.6 Discussion

The values for the unirradiated silicon are in good agreement with previous measurements [9, 53]. Moreover, the results for 2 and 3 Tesla are consistent with the B-field dependence of equation (4.31).

The interpretation of the situation in the irradiated case is more complex. The charge sharing pattern is not uniform over the depth of the device. The result in table 4.4 shows a rather large range that is due to the simplified straight line assumption in our analysis. Our current understanding is that the reduced Hall mobility in the high $\mathcal{E}$-field regions of the detector do not sufficiently explain the observed experimental behaviour. In addition, it is assumed that regions of low electric field strength below the surface between the pixels suppress the Lorentz-effect. In order to verify this idea a simulation was performed to model the contributions that could not be resolved by the measurement. A detailed description and the results of this simulation can be found in [7]. It includes time resolved signal formation on the sensing electrodes, trapping effects for electrons and holes as well as undepleted regions. The comparison between simulations which model regions of low field, and calculations where these regions were disabled support our interpretation of the experimental data.

However, in a measurement this behaviour normally remains concealed if the applied method does not probe the sensor for various bulk depth segments. The grazing angle method, which acts like a "three dimensional light spot measurement", is an ideal tool for such studies.

The temperatures and bias voltages during the measurement were not identical for the unirradiated and the irradiated devices. It is expected that the Lorentz-angle varies with changing conditions. The comparison of the two results would therefore require a correct scaling of the different temperatures and bias conditions. However, it is important to note that our measurements for the irradiated device were done under the similar conditions that will be encountered by the CMS pixel detector at the LHC accelerator.

CHAPTER FIVE

CONCLUSIONS FOR THE CMS PIXEL DETECTOR

The main conclusion from the investigations presented in this work is that we have a working sensor design which is able to meet the demands of LHC, in particular to cope with the high radiation dose-rate. The addressed problems and their answers are listed in the following:

- The pixel isolation was found to saturate at a fluence of $\sim 2 \cdot 10^{14}$ hadrons per cm^2 with an inter-pixel resistance of a few GΩ. In spite of this unexpected high resistance no stochastic discharges were found. Such discharges were observed in former tests [7]. Therefore, the current p-stop design fulfils its task. There was no significant difference between oxygenated and standard silicon sensors with respect to the pixel isolation.

- A guard ring design was found that holds up to 1 kV after irradiation, which by far meets the specification of 300 V given in the CMS Tracker Technical Design Report [4].

- The total pixel capacitance was measured to be (25.7 ± 1.8) fF for the pixel design proposed in the Technical Design Report [4]. This value is lower than expected. Therefore, an increase due to design changes can be tolerated.

- MOS capacitors proofed to be good instruments to investigate the Si-SiO$_2$ interface. In unirradiated devices the oxide charge- and the interface defect-densities could be measured. This allows to determine variations between the processes of different vendors. For example, such measurements clarified the observed differences in pixel isolation between CSEM and SINTEF. After irradiation a shallow layer of unknown thickness was found right below the Si-SiO_2 interface, where type inversion did not occur even after a fluence of $6 \cdot 10^{14}\,\mathrm{cm}^{-2}$.

- With the grazing angle method [62] a tool is available to investigate the Lorentz-effect (charge sharing among pixels in a magnetic field) as a function of bulk depth. It was found that the charge sharing is still sufficient after a harsh irradiation and with partial depletion only. However, the charge sharing pattern is not uniform over the whole depletion depth. Zones with high electric field gradients between the pixels strongly influence the charge drift, and make the charge sharing less predictable.

Nevertheless, there is still room for improvements. Many of the presented measurements indicated possible ameliorations of the design. Since many of the design parameters are highly correlated and some are even contradictory, careful reassessments should be made when a parameter is going to be changed. Below, some summarising recommendations from my measurements and simulations for the final pixel design are itemised.

① *Only one p-stop ring with wide opening*

Due to the very high inter-pixel resistance after irradiation one open p-stop ring around each pixel provides enough isolation. In order to prevent an early pinch-off of the conductive channel, the opening of the p^+ rings and the distance between them should be made as large as possible. A value of $15\,\mu$m or even $20\,\mu$m seems to be feasible. There is no significant difference between oxygenated and non-oxygenated silicon with respect to the inter-pixel resistance. Hence, future pixel isolation tests can also be done with standard silicon.

② *Smaller gaps between the n^+ implants*

This measure reduces the high field strengths at the sensor surface between the pixels and leads to a more predictable charge sharing pattern, since the non-linearities of the bulk electric field between pixels are reduced. A disadvantage is however the higher pixel capacitance. As shown in this work the pixel capacitance can be increased by a factor of three without infringing the operation conditions of the CMS pixel detector system. Since this recommendation contradicts point ①, a compromise has to be found. For example, the distance between the n^+ implants could be chosen as $50\,\mu$m and the p-stop ring width as $8\,\mu$m, resulting in a gap of $18\,\mu$m between the p-stops.

③ *Guard ring design with ten guards, as it was presented in this work*

The guard ring design with 10 guards fulfils the CMS pixel requirements and does not need to be modified. However, since the performance of guard rings very much depends on the production process some care will have to be exercised if the sensors are finally produced by other vendors.

④ *Use oxygenated silicon*

From various CERN measurements it is known that oxygen enhancement in silicon reduces the β factor (the radiation induced acceptor introduction rate). In this work is was shown that the oxygenation does not influence surface parameters like the inter-pixel resistivity. It has however a beneficial effect on the β factor, since it was shown to increase the type inversion fluence. These results strongly suggest to use oxygen enriched silicon for the CMS pixel detector.

⑤ *Moderate doping of the p-stop rings*

A lower doping concentration in the p-stop rings would lead to a smaller doping gradient and hence to lower electric field maxima at the edges of the p-stop rings. At the extreme this leads to the p-spray technique, in which the p-implant is not spatially defined with a mask, but sprayed over the whole wafer with moderate concentration. So far, only very few vendors have experience with this technique.

With these recommendations the final pixel sensor design would look like figures 5.1 and 5.2. In figure 5.1 a proposal is shown for the pixel front side of the sensor. For the guard rings on the backside, the design already shown in figure 3.8 is proposed. For reasons of completeness it is displayed again in figure 5.2.

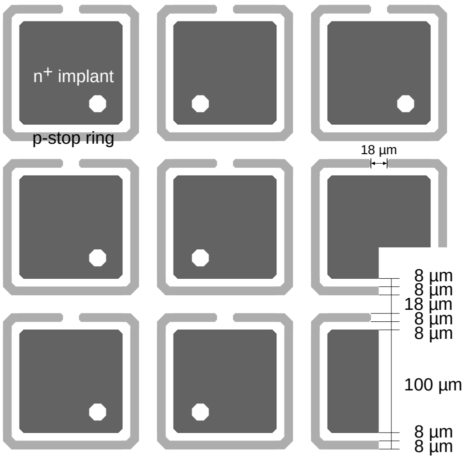

Figure 5.1: *Proposal for the front side.*

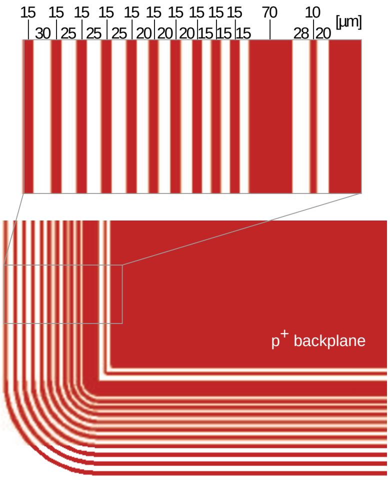

Figure 5.2: *Backside proposal.*

APPENDIX A: LIST OF SYMBOLS

A	Area (e. g., of a diode)
B	Magnetic field strength
C	Capacitance
C_{it}	Interface trap capacitance
C_{ox}	Oxide capacitance
C_p	Parallel plate capacitance
C_s	Silicon depletion layer capacitance
$\mathcal{D}$	Radiation dose or dose rate
d	Thickness or distance
D_{it}	Interface defect density
d_{ox}	Oxide thickness
E	Energy
$\mathcal{E}$	Electric field strength
E_F	Fermi energy
E_g	Band gap energy
ENC	Equivalent noise charge
h	Planck constant
$I(V_m)$	Current through pixel at V_m
I_{vol}	Leakage current per volume
$J_{n,p}$	Electron/hole current density
k	Boltzmann constant
L	Length of a channel
$\mathcal{L}$	Luminosity
L_D	Debye length
$m^\star$	Effective mass
MIP	Minimum ionising particle
n^-	Lightly n-doped
n^+	Heavily n-doped
n_0	Electron concentration
N_A	Acceptor concentration
N_D	Donor concentration
N_{eff}	Effective doping $\lvert N_A - N_D \rvert$
n_i	Intrinsic electron concentration
$NIEL$	Non ionising energy loss
p^-	Lightly p-doped
p^+	Heavily p-doped
p_0	Hole concentration
PCB	Printed circuit board
PKA	Primary knock-on atom
q	Elementary charge
Q_{it}	Interface charge density
Q_{ox}	Oxide charge density
Q_s	Silicon surface charge density
R	Interpixel- or channel-resistance
r_H	Hall factor (μ_H/μ)
S/N	Signal to noise ratio
t	Time
T	Temperature
UBM	Under bump metallisation
V	Potential or voltage
V_B	Breakdown voltage
V_{bias}	Reverse bias voltage over a p-n junction
V_{FB}	Flat band voltage
V_{FD}	Full depletion voltage
V_g	Gate voltage of MOS capacitor
V_i	Built in voltage of a p-n junction
V_m	Potential of a test- or mid-pixel
$v_{n,p}$	Drift velocity of electrons/holes
v_t	Thermal velocity of charge carriers
W	Width of a conductive channel
x_n	Depletion depth in n-type silicon
x_p	Depletion depth in p-type silicon
α	Current related damage rate
α_n	Ionisation coefficient for electrons
α_p	Ionisation coefficient for holes

β	Acceptor introduction rate after type inversion
δ	Impact parameter
ε_o	Permittivity of vacuum
ε_{si}	Dielectric constant of silicon
ε_{ox}	Dielectric constant of SiO_2
η	Pseudo rapidity
Θ_L	Lorentz angle
μ_H	Hall mobility
$\mu_{n,p}$	Mobility of electrons and holes
ρ	Resistivity
ρ_m	Density
ρ_q	Volume charge density
ρ_s	Sheet resistivity
σ	Conductivity
τ	Generation or recombination relaxation time
τ_s	Scattering relaxation time
Φ	Fluence (time-integrated flux)
ϕ	Potential
ϕ_{ms}	Work function difference between Al and Si
ϕ_s	Silicon surface potential
ω	Angular frequency $2\pi f$

APPENDIX B: CHARGE DRIFT IN SILICON

In this short compilation some empirical tools are listed to calculate the approximate silicon drift dependencies on high electric and magnetic fields, temperature, doping and irradiation induced trapping. It was published as an Internal CMS Pixel Note [64].

B.1 Introduction

The most accurate description of transport phenomena in semiconductors can be given by solving the Boltzmann equation ([65] Roth, Conwell). But quite often one is only interested in macroscopic parameters and their behaviour in strong fields (and not in the exact energy states of single electrons). The aim of this work is to summarise some simple approximating tools and values in order to get an idea how this parameters can be scaled with changing environments such as electric and magnetic fields, temperature, irradiation, etc.

B.2 A Classical Equation of Motion

It was shown in the past ([65] Smith, [66], [67]) that transport of electrons and holes in semiconductors in electric and magnetic fields can be described relatively well by a single classical (vector-) equation for each particle (accuracy $\approx 10\%$). The nature of the quantum states is introduced by the concept of the effective particle mass ($m^\star$). This equation also includes a linear damping term $q/\mu \cdot d\vec{r}/dt$ which describes the scattering (at lattice phonons and impurities) in terms of a relaxation time. The effect of the distribution of electrons in the energy bands can then be included by allowing the relaxation time and effective mass to be functions of particle energy and performing a suitable average calculation.

One parameterisation of this equation is [66]

$$m^\star \cdot \frac{d^2\vec{r}}{dt^2} = q \cdot \frac{\mu_H}{\mu} \cdot \frac{d\vec{r}}{dt} \times \vec{B} + q \cdot \vec{\mathcal{E}} + \frac{q}{\mu} \cdot \frac{d\vec{r}}{dt} \tag{B.1}$$

where $\vec{r}$ is the position vector of the electron or hole, $\vec{B}$ ($\vec{\mathcal{E}}$) the magnetic (electric) field, respectively, $m^\star$ the effective mass averaged over all directions and q the charge with appropriate sign for electrons or holes. The mobilities μ and μ_H are the normal mobility and the Hall mobility ($\mu_H = r_H \cdot \mu$).

The mobility is related to the averaged scattering relaxation time τ_s (approximately the mean free time between two scatterings) by

$$\mu = \frac{q}{m^\star} \cdot \tau_s \quad . \tag{B.2}$$

Without magnetic fields the drift velocity can be written as

$$\vec{v}_d = \mu \cdot \vec{\mathcal{E}} \quad . \tag{B.3}$$

If both fields are applied, equation (B.1) has to be solved with the appropriate directions of $\vec{\mathcal{E}}$ and $\vec{B}$. For the general directions of electric and magnetic fields the steady state solution is [66]

$$\begin{aligned} \frac{d\vec{r}}{dt} = \begin{pmatrix} dx/dt \\ dy/dt \\ dz/dt \end{pmatrix} &= \mu_{red} \\ &\times \begin{pmatrix} 1+\mu_H^2 B_x^2 & \mu_H^2 B_x B_y - \mu_H B_z & \mu_H^2 B_x B_z + \mu_H B_y \\ \mu_H^2 B_x B_y + \mu_H B_z & 1+\mu_H^2 B_y^2 & \mu_H^2 B_z B_y - \mu_H B_x \\ \mu_H^2 B_x B_z - \mu_H B_y & \mu_H^2 B_z B_y + \mu_H B_x & 1+\mu_H^2 B_z^2 \end{pmatrix} \\ &\times \begin{pmatrix} \mathcal{E}_x \\ \mathcal{E}_y \\ \mathcal{E}_z \end{pmatrix} \end{aligned} \tag{B.4}$$

where the reduced mobility μ_{red} is given by

$$\mu_{red} = \frac{\mu}{1+\mu_H^2 B^2} \quad . \tag{B.5}$$

For small field strengths and doping concentrations below $10^{12}\,\mathrm{cm}^{-3}$ the drift mobilities at room temperature are [59]

$$\mu_n = 1350\,\mathrm{cm}^2\,\mathrm{V}^{-1}\,\mathrm{s}^{-1} \quad \text{and} \quad \mu_p = 480\,\mathrm{cm}^2\,\mathrm{V}^{-1}\,\mathrm{s}^{-1} \quad . \tag{B.6}$$

B.3 Hot Electrons and Holes

Within a high electric field, free-charge carriers (electrons or holes) gain energy from this field. Since the carriers must remain in the energy band structure of the semiconductor this energy has to be relaxed to the lattice through increased carrier-phonon scattering. This effect becomes important if the energy gained from the field is of the same order of magnitude as the thermal energy of the carriers (e.g. when the drift velocity $\mu \cdot \mathcal{E}$ becomes higher than the thermal velocity $\approx \sqrt{kT/m^\star}$). Since this behaviour is similar to an increase of the carrier temperature the carriers are said to be hot (hot electron effect, see [65] Ferry).

Due to the increased phonon scattering the mobility does not remain constant but decreases with increasing field strength. Then, according to equation (B.3), the drift velocity no longer increases linearly with the field. At very high electric fields, the velocity saturates.

An empirical analytic expression for the mobility dependence on doping density and electric field strength was derived in reference [60]. The first term in equation (B.7) describes the doping dependence on the mobility whereas the second stands for the field dependence

$$\mu = \left\{ \mu_{min} + \frac{\mu_{max} - \mu_{min}}{1 + \left(\frac{N_{eff}}{N_{ref}}\right)^{\alpha}} \right\} \cdot \left\{ \frac{1}{\left(1 + \left(\frac{\mathcal{E}}{\mathcal{E}_c}\right)^{\beta}\right)^{1+1/\beta}} \right\} \quad . \tag{B.7}$$

$\mathcal{E}_c$ is a function of doping given by

$$\mathcal{E}_c = \frac{v_m}{\mu_{min} + \frac{\mu_{max} - \mu_{min}}{1 + \left(\frac{N_{eff}}{N_{ref}}\right)^{\alpha}}} \tag{B.8}$$

N_{eff} is the effective doping density and $\mathcal{E}$ the electric field. N_{ref} is a normalisation-parameter, as well as α. $\beta = 1$ is valid for holes and $\beta = 2$ for electrons, v_m is a constant related to the maximal saturation velocity. μ_{max} is the mobility in pure silicon and μ_{min} stands for the mobility saturation value at very high doping.

However, if the doping variation is so small that the mobility can be assumed to be independent of it ($N_{A,D} \leq 10^{15}\,\mathrm{cm}^{-3}$) the field dependence and the temperature are the only scaling parameters remaining. Again, there are empirical expressions for the mobility and the velocity [60] given by

$$\mu = \frac{\mu_0}{\left(1 + \left(\frac{\mathcal{E}}{\mathcal{E}_c}\right)^{\beta}\right)^{1/\beta}} \quad \text{and} \quad v = v_m \cdot \frac{\mathcal{E}/\mathcal{E}_c}{\left(1 + \left(\frac{\mathcal{E}}{\mathcal{E}_c}\right)^{\beta}\right)^{1/\beta}} \tag{B.9}$$

with $\mu_0 = v_m/\mathcal{E}_c$. $\mathcal{E}$ is the electric field, $\mathcal{E}_c$ is here treated as a normalisation-parameter, as well as v_m. And again $\beta = 1$ is employed for holes and $\beta = 2$ for electrons.

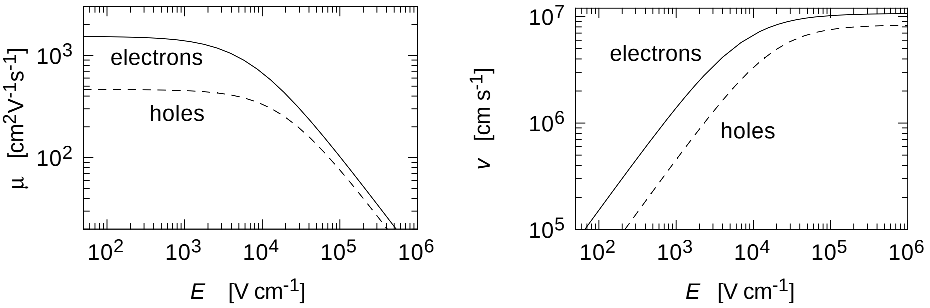

Figure B.1: *Left: mobility, right: drift velocity vs. electric field; according to equations (B.9); $T = 300\,K$, $N_{A,D} \leq 10^{15}$ cm^{-3}.*

B.3.1 Temperature Dependence

In [68] the equations (B.9) are quoted with β being a variable, depending also on the temperature. In figure B.1, μ and v_d are plotted as functions of the electric field $\mathcal{E}$, according to equations (B.9) (T=300 K). The parameters are taken from [68] ($N_{A,D} \leq 10^{15}\,\mathrm{cm}^{-3}$, $T \geq 250\,\mathrm{K}$). The values employed with their temperature dependencies are given in table B.1.

Table B.1: *Temperature dependent parameters for equations (B.9).*

electrons	holes
$v_m = 1.53 \cdot 10^9 \cdot T^{-0.87}\,\mathrm{cm\,s^{-1}}$	$v_m = 1.62 \cdot 10^8 \cdot T^{-0.52}\,\mathrm{cm\,s^{-1}}$
$\mathcal{E}_c = 1.01 \cdot T^{1.55}\,\mathrm{V\,cm^{-1}}$	$\mathcal{E}_c = 1.24 \cdot T^{1.68}\,\mathrm{V\,cm^{-1}}$
$\beta = 2.57 \cdot 10^{-2} \cdot T^{0.66}$	$\beta = 0.46 \cdot T^{0.17}$

An even simpler relationship between μ_n, μ_p and T can be found in [59]. The following values approximate the temperature dependence of the mobilities for doping concentrations $N_{A,D} \leq 10^{14}\,\mathrm{cm}^{-3}$ and $T \geq 100\,\mathrm{K}$:

$$\mu_n \propto T^{-2.42} \qquad \mu_p \propto T^{-2.20} \quad . \tag{B.10}$$

A very good review related to electron and hole velocities in silicon and their temperature dependence can be found in [69] in which drift velocities were measured with the Time-of-Flight technique for high resistivity silicon[1].

B.4 Magnetic and Electric Fields

Consider a charged particle drifting in constant electric and magnetic fields. The resulting force on the particle is

$$\vec{F} = q \cdot (\vec{\mathcal{E}} + \vec{v} \times \vec{B}) \quad . \tag{B.11}$$

If the time between two phonon- or impurity-scatterings τ_s is long enough the particle performs a circular motion (cyclotron motion) with $\omega_c = q\,B/m^\star$ (condition $\omega_c\,\tau_s \gg 1$). This method can be used to measure $m^\star$. However, if $\omega_c\,\tau_s \ll 1$ the particle "forgets" its history with each collision and performs a random walk with an averaged net velocity in the direction of $\vec{F}$. If $\vec{B}$ is perpendicular to $\vec{\mathcal{E}}$ the carriers drift at an angle Θ_L (Lorentz angle) with respect to the direction of the electric field

$$\tan(\Theta_L) = \mu_H \cdot |\vec{B}| \tag{B.12}$$

where $\vec{B}$ is the magnetic field and μ_H the Hall-mobility. This Hall mobility is related to the normal drift mobility via

$$\mu_H = r_H \cdot \mu \tag{B.13}$$

where r_H is of the order of unity[2]. The factor r_H represents the influence of the magnetic field on the scattering-relaxation time τ_s. For not too strong magnetic fields it can be written as ([65] Conwell)

$$r_H = \frac{\mu_H}{\mu} = \frac{\langle E\tau_s^2\rangle\langle E\rangle}{\langle E\tau_s\rangle^2} \tag{B.14}$$

where E denotes the carrier energy. In general, τ_s is a function of carrier energy. If τ_s were independent of energy then r_H would simply be 1. However, the energy dependence is normally not so extreme that r_H differs greatly from unity, e. g., if only phonon scattering (acoustic mode) occurs, r_H can be calculated to be $3\pi/8$. For impurity scattering alone r_H has a value of about 1.93 [12]. In most cases of applications of semiconductors there are be several scattering mechanisms involved. Silicon is even a more complicated case insofar that the surfaces of constant energy are not spherical. Hence r_H

---

[1] Also a good analysis of the negative differential mobility (NDM) in $\langle 100\rangle$ silicon for electrons is included.

[2] r_H is also related to the Hall coefficient R_H used for the Hall effect: $R_H = r_H/(n\,e)$, where n is the density of carriers (Hall voltage $V_H^y = R_H I_x B_z/d$).

has to be measured or evaluated numerically with Monte Carlo techniques. Some values for r_H for different temperatures and doping concentrations are given in [59]. For $T = 300\,\mathrm{K}$, $N_D = 1.75 \cdot 10^{14}\,\mathrm{cm}^{-3}$, $N_A = 3.1 \cdot 10^{14}\,\mathrm{cm}^{-3}$ it is stated that

$$r_H^n = 1.15 \quad \text{and} \quad r_H^p = 0.72 \tag{B.15}$$

for electrons and holes.

An interesting fact is that in this classical picture the energy dependence of τ_s vanishes in the limit $B \to \infty$. Hence $r_H \approx 1$ for very high strengths of the magnetic field.

At very high magnetic fields also quantum mechanical effects can also be found. The condition for this to occur is $\hbar\,\omega_c = \hbar\,q\,B/m^\star \geq k\,T$ ([65] Conwell). Here the energy bands are converted into a series of energy levels known as Landau levels due to the quantisation of the cyclotron motion of the carriers (see e.g. [12]).

B.4.1 Magnetoresistance

Let us look at a carrier drifting in an electric field $\mathcal{E}_x$ and a magnetic field B_z. The velocity of the carrier, which drifts at an angel Θ_L with respect to the electric field (equation (B.12)), can be split into a component parallel to the electric field $v_{\mathcal{E}_x}$ and a Lorentz component v_{L_y} perpendicular to the electric and the magnetic field. This velocity component however interacts with the magnetic field B_z again and creates a repulsive second order Lorentz force which counteracts the original accelerating electric force (see figure B.2). This effect is known as the transverse magnetoresistance[3]. The following "derivation" is very approximate and should only be used in order to get an idea about the order of magnitude of the effect.

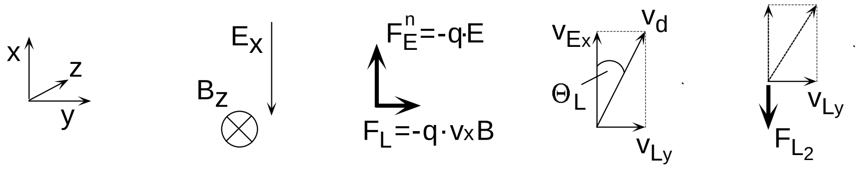

Figure B.2: *Kinetic interpretation of the transverse magnetoresistance for electrons. The velocity v_{L_y} interacts with B_z and gives rise to F_{L_2}.*

Geometric considerations and equation (B.12) lead to

$$v_{L_y} = v_{\mathcal{E}_x} \cdot \tan\Theta_L = \mu\,\mathcal{E}_x \cdot \mu_H\,B_z \quad . \tag{B.16}$$

---

[3] There is also a longitudinal magnetoresistance ($\vec{\mathcal{E}} \parallel \vec{B}$). But in silicon it is much smaller than in the transversal case, and there is no simple estimate for its strength (see e.g. [12]).

With the definition $F_L = q \cdot \vec{v} \times \vec{B}$ the repulsive second order Lorentz force becomes

$$F_{L_2} = q\,\mu\,\mu_H\,\mathcal{E}_x\,B_z^2 \quad . \tag{B.17}$$

The quotient $F_{L_2}/q\mathcal{E}_x$ gives the ratio of this second order Lorentz-force to the original accelerating electric force

$$\frac{F_{L_2}}{q\,\mathcal{E}_x} = -\,\mu\,\mu_H\,B_z^2 = -\,r_H\,\mu^2 B_z^2 \quad , \tag{B.18}$$

for example, in a magnetic field of 4 T the absolute value of this quotient is about 0.3 for electrons and 0.05 for holes. For such strong fields the magnetoresistance normally can not be neglected. Further information on this subject can be found in [12].

For high magnetic fields the magnetoresistance effect should be taken into account in the equation of motion (equation (B.1)). In this simple model with $\vec{\mathcal{E}} = (\mathcal{E}_x, 0, 0)$ and $\vec{B} = (0, 0, B_z)$, both velocity components v_x as well as v_y are affected by the same factor. The ratio of v_y and v_x however, which corresponds to the tangent of the Lorentz-angle, remains independent of the magnetoresistance

$$\tan\Theta_L = \frac{v_y}{v_x} = \mu_H\,B_z \quad . \tag{B.19}$$

More accurate models which distinguish high and low fields can be found in [12].

B.5 Effective Mass $m^\star$

In the equation of motion (equation (B.1)) the effective mass of the charge carriers (electrons and holes) is quoted instead of the free electron mass. With this concept the "definition" of the electric force as $\vec{F} = q \cdot \vec{\mathcal{E}} = m^\star d\vec{v}/dt$ remains valid even for the different energy states which charge carriers can have in a energy band.

Since in silicon the surfaces of constant energy are not spherical the effective mass depends on the energy band orientation. For electrons one normally distinguishes a longitudinal and a transversal effective mass [4] as determined in [70]

$$m_l^n = 0.98\,m_0^n \quad \text{and} \quad m_t^n = 0.19\,m_0^n \quad . \tag{B.20}$$

---

[4] In the Brioullin zones of silicon the surfaces of constant energy in the conduction band are rotational ellipsoids. Since they have two symmetry axes it is convenient to describe them with two effective masses.

Here, m_0^n denotes the free electron mass. Due to the degeneration of two valence bands in silicon, there are also two effective masses for holes. Here the terminology commonly used is light and heavy holes. The values quoted in [68] are

$$m_l^p = 0.16\, m_0^n \quad \text{and} \quad m_h^p = 0.49\, m_0^n \quad . \tag{B.21}$$

In the equation of motion the averaged effective mass is required. Normally, the so called "conductivity effective mass" is calculated by the inverse sum [48] which

for electrons is

$$\frac{1}{m_n^*} = \frac{1}{3} \cdot \left(\frac{1}{m_l^n} + \frac{2}{m_t^n} \right) \tag{B.22}$$

and for holes is

$$\frac{1}{m_p^*} = \frac{1}{2} \cdot \left(\frac{1}{m_l^p} + \frac{1}{m_h^p} \right) \quad . \tag{B.23}$$

APPENDIX C: DEPLETION WIDTH CALCULATION

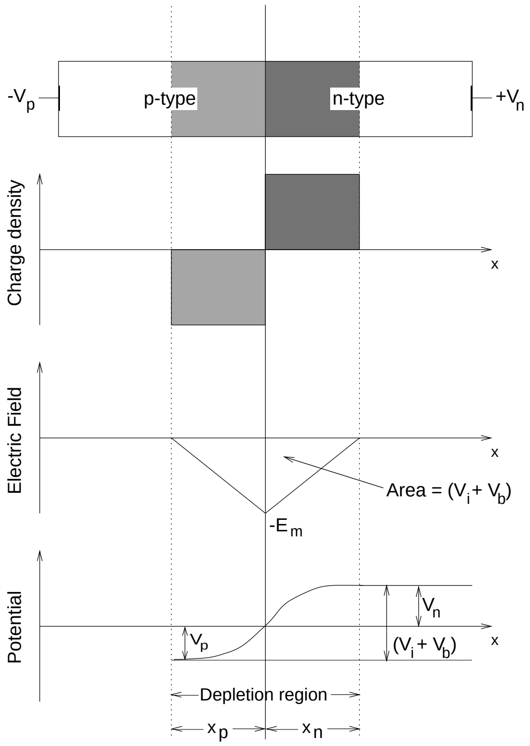

Figure C.1: *Properties of an abrupt pn-junction with a reverse voltage applied.*

The relationship between the charge distribution ρ_q in the depletion region and the electrostatic potential ϕ is given by the one dimensional Poisson-equation

$$\frac{d^2\phi}{dx^2} = -\frac{\rho_q}{\varepsilon_{si}\varepsilon_o} = -\frac{q}{\varepsilon_{si}\varepsilon_o}(N_D - N_A) \quad , \tag{C.1}$$

where $\varepsilon_{si}\varepsilon_o$ is the permittivity of silicon and $N_{D,A}$ denotes the donor (acceptor) density, respectively. The second equation already makes use of the depletion approximation, which assumes the depletion region to be totally free of any mobile charges ($n_0 = p_0 = 0$). The depletion region widths x_n and

x_p can now be calculated separately. If we take the origin at the junction, the n-type region equation becomes

$$\begin{aligned} \frac{d^2\phi}{dx^2} &= -\frac{q}{\varepsilon_{si}\varepsilon_o} N_D \quad \text{for } 0 < x \leq x_n \\ \frac{d^2\phi}{dx^2} &= 0 \qquad\qquad\quad \text{for } x > x_n \end{aligned} \tag{C.2}$$

Integrating (C.2) with respect to x and using the condition that the electric field is zero at x_n, we can write

$$\mathcal{E}(x) = -\frac{d\phi}{dx} = \mathcal{E}_m \left(1 - \frac{x}{x_n}\right) \tag{C.3}$$

where the maximum field $\mathcal{E}_m$ occurs at $x = 0$ and is given by

$$\mathcal{E}_m = -\frac{qN_D}{\varepsilon_{si}\varepsilon_o} x_n \quad . \tag{C.4}$$

The expression for $\mathcal{E}(x)$ can be integrated once again to yield

$$\phi(x) = \frac{qN_D}{\varepsilon_{si}\varepsilon_o} \left(x_n x - \frac{x^2}{2}\right) \quad . \tag{C.5}$$

In deriving this relation we used the boundary condition $\phi = 0$ at $x = 0$. The potential V_n at the edge x_n can be obtained from equation (C.5) as

$$V_n = \frac{qN_D}{2\varepsilon_{si}\varepsilon_o} x_n^2 \quad . \tag{C.6}$$

Similar calculations made on the p-side of the junction lead to the following expressions:

$$\mathcal{E}(x) = \mathcal{E}_m \left(1 + \frac{x}{x_p}\right) \tag{C.7}$$

$$\mathcal{E}_m = -\frac{qN_A}{\varepsilon_{si}\varepsilon_o} |x_p| \tag{C.8}$$

$$\phi(x) = \frac{qN_A}{\varepsilon_{si}\varepsilon_o} \left(x_p x - \frac{x^2}{2}\right) \quad \text{and} \tag{C.9}$$

$$V_p = -\frac{qN_A}{2\varepsilon_{si}\varepsilon_o} x_p^2 \quad . \tag{C.10}$$

Equation (C.10) was obtained by substituting $x_p = -x$ in (C.9). The electric field at $x = 0$ must be continuous, so that the values of $\mathcal{E}_m$ are the same for both sides. Hence,

$$N_A |x_p| = N_D |x_n| \tag{C.11}$$

which means that the space charges on the two sides of the junction have the same magnitude. From this equation one can also see that the depletion width on each side of the junction is inversely proportional to the doping concentration on that side. Thus, in a junction where N_A is orders of magnitudes higher than N_D, the depletion region extends largely on the n-side, making x_p negligible compared to x_n (one sided abrupt p^+-n junction).

The total change in potential from the p- to the n-side is the difference $(V_n - V_p)$, which can be written as

$$V_n - V_p = V_{bias} + V_i = \frac{q}{2\varepsilon_{si}\varepsilon_o}\left(N_D x_n^2 + N_A x_p^2\right) \quad . \tag{C.12}$$

It can be seen from equation (C.12) that, in a asymmetrical junction where N_A and N_D are different, the major portion of the potential drop occurs on the low doped side, where the depletion region is thicker. If the differences are several orders of magnitude, the high doping part of the voltage drop can be neglected (V_p in the example above). With this approximation one obtains the well known depletion region formula:

$$x_n = \sqrt{\frac{2\varepsilon_{si}\varepsilon_o(V_{bias} + V_i)}{qN_D}} \quad . \tag{C.13}$$

APPENDIX D: MOS-CAPACITORS

D.5.1 Model of an Ideal MOS Capacitor

In this appendix the equations needed to obtain the oxide charge concentration Q_{ox} and the interface defect density D_{it} from MOS-CV measurements are developed. The calculation mainly follows arguments given in [11, 19, 47].

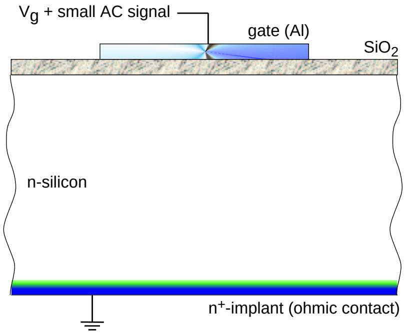

Figure D.1: *Cross section of a MOS capacitor.*

The MOS capacitor in figure D.1 would act as a parallel plate capacitor with SiO_2 as dielectric medium if silicon were a perfect conductor. However, the MOS capacitor is more complicated because the silicon surface potential is influenced by the gate voltage.

When a DC voltage V_g is applied between the gate and the silicon substrate the potential at the silicon surface under the gate is altered, but no current can flow because of the insulating oxide layer in between. Consequently, the surface space charge region in the semiconductor remains in thermal equilibrium. But the change of the potential at the semiconductor surface results in a modification of the mobile charge concentration at the surface, depending on the magnitude and the sign of V_g.

One part of V_g appears across the oxide (V_{ox}) and one part across the silicon (ϕ_S), so that

$$V_g = V_{ox} + \phi_s \quad . \tag{D.1}$$

If we assume the electric flux to be continuous (no charges directly at the interface) we get from Gausses law:

$$\varepsilon_{ox}\varepsilon_{o}\frac{V_{ox}}{d_{ox}} = \varepsilon_{si}\varepsilon_{o}\mathcal{E}_{s} = -Q_{s} \quad , \tag{D.2}$$

here $\varepsilon_{ox}\varepsilon_{o}$ and $\varepsilon_{si}\varepsilon_{o}$ represent the oxide and silicon permittivities, respectively, $\mathcal{E}_s$ is the electric field at the surface of the semiconductor , Q_s the silicon surface charge density and d_{ox} the oxide thickness. The small signal capacitance of a MOS capacitor is defined by

$$C \equiv \frac{dQ_g}{dV_g} = -\frac{dQ_s}{dV_g} \quad , \tag{D.3}$$

where $Q_g = -Q_s$ is the charge per unit area on the gate electrode. With the definitions (per unit area) of the oxide capacitance $C_{ox} \equiv \varepsilon_{ox}\varepsilon_{o}/d_{ox}$ and the silicon depletion layer capacitance $C_s \equiv -dQ_s/d\phi_s = \varepsilon_{si}\varepsilon_{o}/x_n$ (x_n represents the depletion depth) the normalised capacitance C/C_{ox} can be written as [11]:

$$\frac{C}{C_{ox}} = \frac{1}{1 + \frac{C_{ox}}{C_s}} \quad . \tag{D.4}$$

For a given oxide thickness d_{ox}, C_{ox} is constant and independent of the gate voltage. Hence, if the voltage dependence of C_s is known the ratio C/C_{ox} can be calculated for a given V_g. This is done in the following.

At $V_g = 0\,\mathrm{V}$ the MOS system is in thermal equilibrium, the bands are flat and there is no charge in the semiconductor (flat band condition, $\phi_s = 0\,V$). A small AC signal, e. g., applied to measure the capacitance, produces a narrow dynamic depletion region in the semiconductor, whose thickness equals the extrinsic Debye length L_D (the screening length of the Debye Hüeckel-theory), given by

$$L_D = \sqrt{\frac{kT\varepsilon_{si}\varepsilon_{o}}{q^2(n_0 + p_0)}} \quad . \tag{D.5}$$

For a n-type substrate $n_0 \approx N_D$ and $p_0 \approx 0$. Substituting $C_s = \varepsilon_{si}\varepsilon_{o}/L_D$ in equation (D.4), the normalised flat band capacitance C_{FB}/C_{ox} $\equiv C(\phi_s = 0\mathrm{V})/C_{ox}$ can be written as

$$\frac{C_{FB}}{C_{ox}} = \frac{1}{1 + \frac{C_{ox}L_D}{\varepsilon_{si}\varepsilon_{o}}} \quad . \tag{D.6}$$

When the gate voltage is made positive the electron concentration increases above n_0 (accumulation regime, see figure D.2). This causes a decrease of

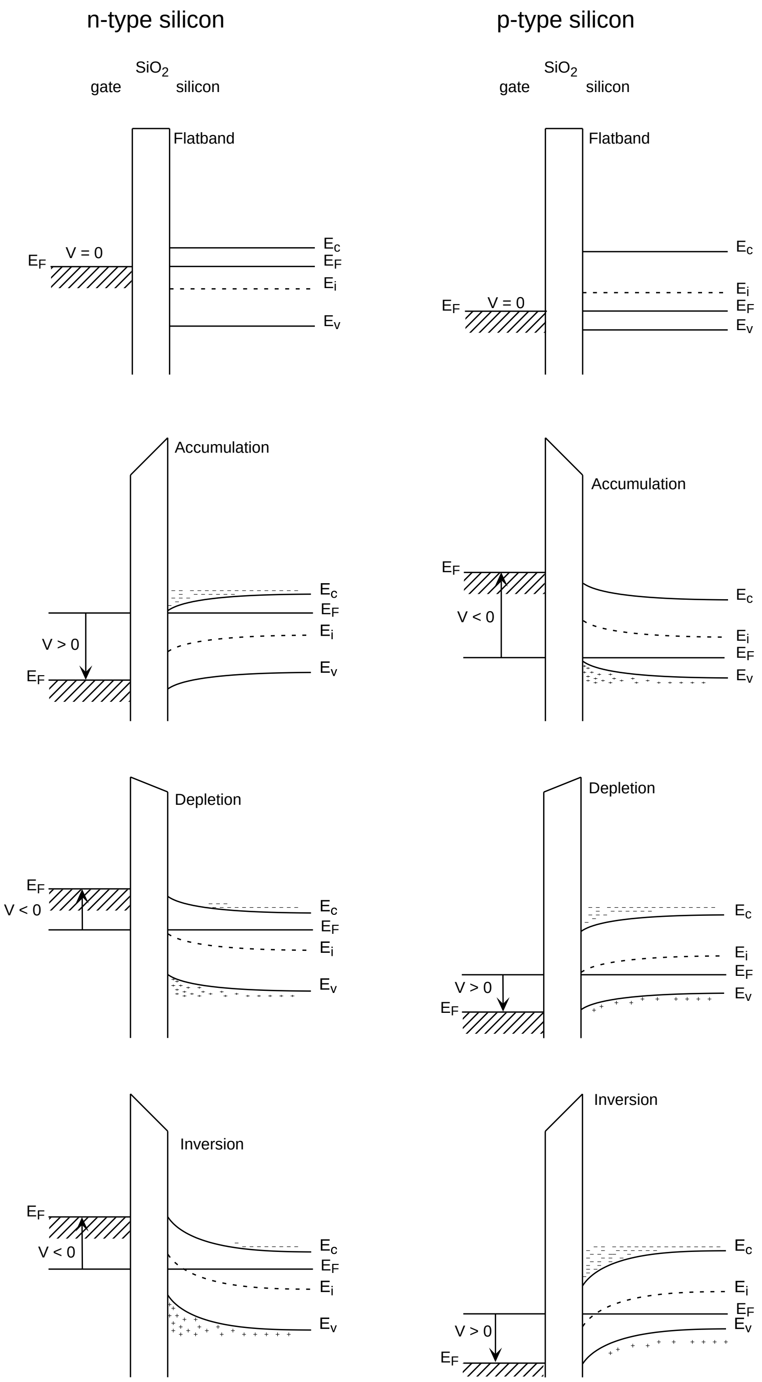

Figure D.2: *Energy band diagrams of an ideal MOS capacitor under flat-band, accumulation, depletion and inversion conditions;* E_F*: Fermi energy,* E_i*: intrinsic Fermi energy,* E_c*: conduction band edge,* E_v*: valence band edge.*

the effective Debye length and a consequent increase of the capacitance C_s. Thus, the ratio C/C_{ox} starts to increase for positive values of V_g until a large number of excess electrons are pulled close to the oxide. As a result C_s becomes large and C/C_{ox} approaches unity (i. e., $C = C_{ox}$).

For a negative value of the gate voltage V_g electrons are pushed away from the interface creating a depletion region in the semiconductor (depletion regime). The depletion region capacitance, in series with the oxide capacitance, reduces the total capacitance well below C_{ox}. For more and more negative values of V_g, the depletion region continues to grow until V_g becomes sufficient to create strong inversion[5] at the surface (inverstion regime, see figure D.2).

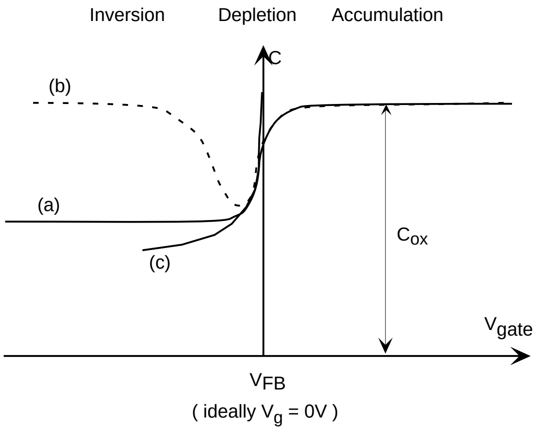

Figure D.3: *Ideal MOS capacitance-voltage curves: (a) high frequency, (b) low frequency, (c) depletion approximation.*

Theoretically, the potential distribution ϕ in the surface region could be obtained from the solution of the one-dimensional Poisson equation

$$\frac{d^2\phi}{dx^2} = -\frac{\rho_q}{\varepsilon_{si}\varepsilon_o} \quad \text{with} \quad \rho_q = q\,(N_D - N_A + p_0 - n_0) \tag{D.7}$$

and C_s could be calculated as a function of V_g. However, since $C = C_{ox}$ in the accumulation case anyway, C_s has only to be calculated for depletion and inversion. And this can be done with the depletion approximation. Accordingly, the depletion region is regarded as completely free of mobile carriers, so that $n_0 = p_0 = 0$. For a n-type substrate this simplifies the Poisson equation to

$$\frac{d^2\phi}{dx^2} = -\frac{N_D}{\varepsilon_{si}\varepsilon_o} \quad . \tag{D.8}$$

Solving this equation with the boundary conditions $d\phi/dx = 0$ and $\phi = 0$

---

[5] Strong inversion is said to occur if the the minority charge carrier concentration exceeds the majority carrier concentration. This condition corresponds to the threshold voltage in MOS transistors.

at $x = x_n$ leads to

$$\phi(x) = \phi_s \left(1 - \frac{x}{x_n}\right)^2 \quad \text{with} \quad \phi_s = \frac{qN_D x_n^2}{2\varepsilon_{si}\varepsilon_o} \quad . \tag{D.9}$$

With the definitions of ϕ_s, C_s and equation (D.1) the ratio C/C_{ox} can be written as

$$\frac{C}{C_{ox}} = \frac{1}{\sqrt{1 + \frac{2V_g}{q\varepsilon_{si}\varepsilon_o N_D} C_{ox}^2}} \quad . \tag{D.10}$$

Calculations made using the depletion approximation and equation (D.10) are shown by the curve (c) in figure D.3. The curves (a) and (b) are explained in the next paragraphs.

As mentioned above the MOS capacitance C is measured by superimposing a small AC signal (about 5 mV) on the DC gate voltage. In the accumulation and depletion regime the change of the charge in the semiconductor in response to the applied signal requires the flow of majority carriers (i. e., electrons in a n-type bulk). They either move in or out of the depletion region. The time constant associated with this charge transport is the scattering relaxation time τ_s, which is in the order of 10^{-12} s. For signal frequencies ω, for which $\omega\tau_s \ll 1$, the C-V curves for the accumulation and depletion regimes is independent of the frequency. But in the inversion regime the charge flow in response to the AC signal also includes movements of minority carriers (i. e., holes) between the inversion layer and the neutral silicon bulk. Here, the MOS system shows a strong frequency dependence.

At high frequencies and in the inversion regime the response to the AC signal is mainly that majority carriers (electrons) move in and out of the depletion region edge at $x = x_n$. The measured capacitance in this situation is the oxide capacitance C_{ox} in series with the depletion region capacitance C_s. The capacitance C reaches a minimum when strong inversion occurs at the semiconductor surface. Then, the inversion layer concentration shields the depletion region from a further increase. This corresponds to the curve (a) in figure D.3.

But if the frequency is so low that electron-hole pairs can be generated before the AC signal changes its sign the generated holes move to the inversion layer while the electrons replace the electrons that had moved out of the depletion region edge. In this case the inversion layer fully responds to the AC signal and the measured capacitance C is the oxide capacitance alone. Thus, C/C_{ox} rises again towards unity in the inversion regime (dashed curve (b) in figure D.3.

Common frequencies for the high frequency curves are 10 kHz or higher. Theoretically, the low frequency behaviour should be observable below about 100 Hz. But in reality so called quasi-static techniques with frequencies of 1 Hz or below have to be applied. (see e. g., [19])

D.5.2 Real MOS Capacitors

In the discussion of the ideal MOS capacitor we have assumed that there is no band bending in the semiconductor for $V_g = 0\,\mathrm{V}$. This condition is not realised in practise. The following factors lead to a non-ideal behaviour of the MOS capacitor: (1) metal-semiconductor work function differences, (2) immobile oxide charges, (3) mobile ions in the oxide and finally (4) interface traps.

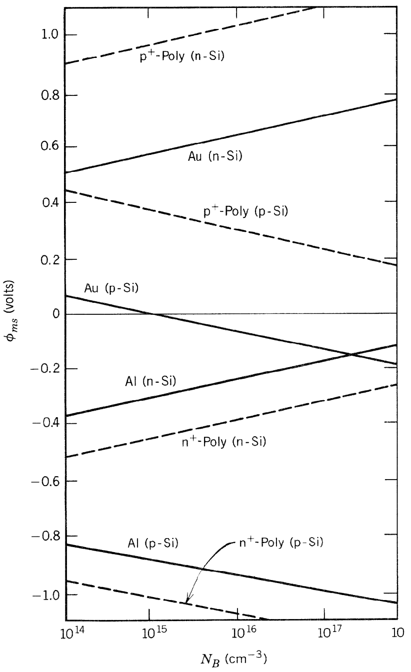

Figure D.4: *The metal-silicon workfunction differences ϕ_{ms} plotted as a function of silicon doping for Al, Au and polysilicon gates (from [11]).*

Workfunction differences ϕ_{ms}: Analogous to the built in potential of a p-n junction, the work function difference between the gate metal and the semiconductor causes a band bending at the semiconductor surface. In order to achieve the flat band condition, a gate voltage equal to the work function difference ϕ_{ms} must be applied. The work function differences for several materials are plotted in figure D.4. For our doping concentrations of $2-3\cdot 10^{12}\,\mathrm{cm}^{-3}$ in n-type silicon (see section 3.3) $\phi_{ms}\approx -0.5\,\mathrm{V}$, which simply causes a parallel shift in V_{FB}: $\Delta V_{FB}^{\phi_{ms}} = -0.5\,\mathrm{V}$.

Immobile oxide charges $\mathbf{Q}_{ox}$: These charges consist of two different contributions, namely fixed and trapped charges (see figure D.5). Both are normally positive. The first category originates in the oxidation process and is not influenced by irradiation, whereas the latter one increases even for low doses until it saturates at about $3\cdot 10^{12}\,\mathrm{cm}^{-2}$ [19]. It has been determined experimentally that most of the immobile oxide charge tends to reside very close to the Si-SiO$_2$ interface. Therefore it is a common practice to assume a sheet charge Q_{ox} right at the interface, which causes a parallel flat band voltage[6] shift of

$$\Delta V_{FB}^{Q_{ox}} = -\frac{Q_{ox}}{C_{ox}} \quad . \tag{D.11}$$

These oxide charges are also responsible for the electron accumulation layer at the semiconductor surface. The positive net-charge of the oxide charges cause a negative "mirror-charge" in the silicon, which is known as the electron accumulation layer. For more details it is referred to [19] and [71].

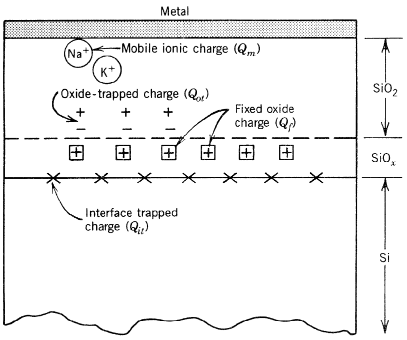

Figure D.5: *Classification of charges in thermally grown oxide (from [71]).*

Mobile oxide charges: They are primary due to alkali ions like Na$^+$, K$^+$ and Li$^+$, which are present in the cleaning solutions that are used during the production process. But the concentration is fairly low and therefore they are not taken into account in the further analysis.

Trapped interface charges $\mathbf{Q}_{it}$: They are mainly due to the breaking of covalent bonds at the Si-SiO$_2$ interface, created by structural defects or radiation. Unlike the other imperfections discussed so far, which all cause a parallel shift of the C-V curve along the voltage axis, the interface traps cause an uneven shift at different surface potentials. This is because the amount of charge trapped at the interface depends on the surface band bending. The amount of (positive) interface trapped charge in donor like traps[7] in a n-type bulk is smallest in accumulation and highest in inversion. The reversed order applies to acceptor like traps[8] (with negative charges). As a result the C-V curves are stretched out along the voltage axis. This stretch-out can be written

---

[6] The flat band condition means that the energy bands of the semiconductor are not bent at the surface, i. e., that no charge is induced in the semiconductor.

[7] A trap that is neutral when it is filled with an electron and positively charged when it is empty.

[8] Traps which are negatively charged when filled with an electron and neutral when empty.

as

$$C_{ox}\, dV_g = [C_{ox} + C_{it}(\phi_s) + C_s(\phi_s)]\, d\phi_s \tag{D.12}$$

with $C_{it}(\phi_s) \equiv -dQ_{it}/d\phi_s$ being the interface trap capacitance per unit area. For frequencies high enough that the interface trapped charges do not respond to the AC signal (about 1 MHz or higher) the C-V curve is only stretched (due to changes in C_s), but V_{FB} is not shifted (i. e., $C_{it} = 0$). The oxygen- and the depletion-capacitances are simply in series:

$$C_{HF} = \frac{C_s C_{ox}}{C_s + C_{ox}} \quad . \tag{D.13}$$

For very low frequencies all interface traps respond to the AC signal and C_{it} is maximal. The traps act like a capacitance C_{it} in parallel with C_s. Therefore,

$$C_{LF} = \frac{C_{ox}(C_s + C_{it})}{C_{ox} + C_s + C_{it}} \tag{D.14}$$

and

$$C_{it}(\phi_s) = q \left[D^a_{it}(\phi_s) + D^d_{it}(\phi_s) \right] \equiv q D_{it}(\phi_s) \quad , \tag{D.15}$$

with $D^a_{it}(\phi_s)$ $[D^d_{it}(\phi_s)]$ being the acceptor [donor] like interface trap density, respectively.

Thus, for high frequencies, the whole CV-curve is shifted along the V_g axis by work function differences and oxide charges with

$$\Delta V_{FB}(HF) = \phi_{ms} - \frac{Q_{ox}}{C_{ox}} \tag{D.16}$$

and stretched out by interface trapped charges, according to equation (D.12) with $C_{it} = 0$. For low frequencies, the same stretch-out function applies (with $C_{it} \neq 0$), but the interface trapped charge also contributes to the flat band voltage shift:

$$\Delta V_{FB}(LF) = \phi_{ms} - \frac{Q_{ox}}{C_{ox}} + \frac{q}{C_{ox}} \int D_{it}(E)dE \quad , \tag{D.17}$$

where D_{it} is integrated over the band-gap.

For the experimental determination of D_{it} equations (D.13) to (D.15) are used. Equation (D.13) is solved for C_s:

$$C_s = \left(\frac{1}{C_{HF}} - \frac{1}{C_{ox}} \right)^{-1} \tag{D.18}$$

and equation (D.14) for C_{it}:

$$C_{it} = \left(\frac{1}{C_{LF}} - \frac{1}{C_{ox}} \right)^{-1} - C_s \quad . \tag{D.19}$$

With equations (D.18) and (D.19) the interface trap capacitance C_{it} can be expressed as

$$C_{it} = (C_{LF} - C_{HF}) \left(1 - \frac{C_{LF}}{C_{ox}} \right)^{-1} \left(1 - \frac{C_{HF}}{C_{ox}} \right)^{-1} \quad , \tag{D.20}$$

which can be translated into an interface state density (D_{it})[9] with equation (D.15):

$$D_{it} = \frac{C_{it}}{q} \quad . \tag{D.21}$$

---

[9] According to equation (D.21) the units of D_{it} should be [C cm^{-2} eV^{-1}]. But since the interface traps do have charged and uncharged states, it is a common practice to give the interface trap density in [cm^{-2} eV^{-1}].

APPENDIX E: BIBLIOGRAPHY

[1] **P. Higgs:** *Phys. Lett. 12(1964)132*
G. Guralnik et al.: *Phys. Rev. Lett. 13(1964)585*
F. Englest et al.: *Phys. Rev. 13(1964)321*

[2] **The Particle Data Group:** Review of Particle Physics, *Europ. Phys. J. C 15(2000)1*

[3] **R. Barate et al. (ALEPH Collaboration):** Observation of an Excess in the Search for the Standard Model Higgs Boson at ALEPH, *Phys. Lett. B 495(2000)1*
M. Acciarri et al. (L3 Collaboration): Higgs Candidates in e^+e^- Interactions at $\sqrt{s} = 206.6\,\mathrm{GeV}$, *Phys. Lett. B 495(2000)18*
P. Abreu et al. (DELPHI Collaboration): Search for the Standard Model Higgs Boson at LEP in the Year 2000, *Phys. Lett. B 499(2001)23*
G. Abbiendi et al. (OPAL Collaboration): Search for the Standard Model Higgs Boson in e^+e^- Collisions at $\sqrt{s} \approx 192 - 209\,\mathrm{GeV}$, *Phys. Lett. B 499(2001)38*

[4] **CMS, the Tracker Project:** Technical Design Report, *CERN/LHCC 98-6, 1998*

[5] **CMS, the Tracker Project:** Addendum to the CMS Tracker Technical Design Report, *CERN/LHCC 2000-016, 2000*

[6] **G. Wrochna:** Challenges of CMS - a Popular Talk, *Available from the CMS homepage http://cmsinfo.cern.ch*

[7] **B. Henrich:** Test and Evaluation of Silicon as Sensor Material for the CMS Pixel Detector, *PhD Thesis, Institut für Physik der Universität Basel, Switzerland, June 1999*

[8] **C. Rott:** private communication (*Purdue University, Indiana, USA*)

[9] **R. Kaufmann:** Performance of a Silicon Pixel Detector in a Magnetic Field, *Diploma Thesis, Physik-Institut der Universität Zürich, Switzerland, 1997*

[10] **A. S. Grove:** Physics and Technology of Semiconductor Devices, *John Wiley & Sons, New York, 1967*[1]

[11] **M. S. Tyagi:** Introduction to Semiconductor Materials and Devices, *John Wiley & Sons, New York, 1991*[3]

[12] **K. Seeger:** Semiconductor Physics; *Springer, Wien, 1973*[1]

[13] **S. M. Sze:** Semiconductor Devices, Physics and Technology, *John Wiley & Sons, New York, 1985*[1]

[14] **G. Lutz:** Semiconductor Radiation Detectors Device Physics, *Springer, Berlin, 1999*[1]

[15] **S. M. Sze (Ed), H. Baltes:** Semiconductor Sensors, Magnetic Sensors. *John Wiley & Sons, New York, 1994*[1]

[16] **ISE - TCAD:** A Complete Semiconductor Simulation Package, *Integrated Systems Engineering AG, Zürich, Switzerland, http://www.ise.ch*

[17] **R. Della Marina:** The Silicon Strip Tracker for the CMS Experiment at LHC, *PhD Thesis, Eidgenössische Technische Hochschule Zürich, Switzerland, 2000, Diss ETH No. 13585*

[18] **Trim:** The Stopping and Range of Ions in Matter, simulation program, *available at http://www.research.ibm.com/ionbeams*

[19] **T. P. Ma, P. V. Dressendorfer:** Ionising Radiation Effects in MOS Devices and Circuits, *John Wiley & Sons, New York, 1989*[1]

[20] **CERN-RD48 (ROSE) collaboration:** 3^{rd} Status Report, *CERN/LHCC 2000-009, available at http://www.cern.ch/rd48*

[21] **T. Angelescu, A. Vasilescu:** Comparison of Radiation Hardness Results obtained from various Neutron Sources and the NIEL Problem, *Nucl. Instr. Meth. in Phys. Res. A 374(1996)85*

[22] **A. Vasilescu, G. Lindström:** Notes on the Fluence Normalisation based on the NIEL scaling Hypothesis, *ROSE TN 2000-02, 2000, available at http://www.cern.ch/rd48*

[23] **P. Riedler:** Radiation Damage Effects and Performance of Silicon Strip Detectors using LHC Readout Electronics, *PhD Thesis, Universität Wien, Austria, 1998*

[24] **G. Lindström et al.:** Radiation Hardness of Silicon Detectors - a Challenge from High-Energy Physics, *Nucl. Instr. Meth. in Phys. Res. A 426(1999)1*

[25] **R. Wunstorf:** Radiation Hardness of Silicon Detectors, Current Status, *IEEE Trans. Nucl. Sci. 44(1997)806*

[26] **F. Lemeilleur:** private communication (*CERN, Switzerland*)

[27] **G. Lutz:** Effects of Deep Level Defects in Semiconductor Detectors, *Nucl. Instr. Meth. in Phys. Res. A 377(1996)234*

[28] **S. J. Watts:** Overview of Radiation Damage in Silicon Detectors - Models and Defect Engineering, *Nucl. Instr. Meth. in Phys. Res. A 386(1997)149*

[29] **KICBox:** A Graphics Editor for Layouts of Mask Sets, *Technische Universität Braunschweig (Germany), Abteilung Entwurf integrierter Schaltungen, 1995*

[30] **Cadence:** The Cadence Analog Design Environment, *Cadence Design Systems Inc., San Jose, California, USA, http://www.cadence.com*

[31] **ATLAS, the Tracker Project:** The ATLAS Inner Detector Technical Design Report, *CERN/LHCC 97-17*

[32] **M. DaRold:** High Voltage devices for Silicon Detector Operation in Future High Energy Physics Experiments, *PhD Thesis, Università Degli Studi di Padova, Italy, 1998*

[33] **C. Becker et al.:** Gate Controlled Diodes for Characterisation of the Si-SiO$_2$ Interface with Respect to Surface Effects of Silicon Detectors, *ROSE TN 996, 1999, available at http://www.cern.ch/RD48*

[34] **W. Shockley, W. T. Read:** Statistics of the Recombination of Holes and Electrons, *Phys. Rev. 87(1952)835*
R. N. Hall: Electron Hole Recombination in Germanium, *Phys. Rev. 87(1952)387*

[35] **L. J. van der Pauw:** A Method of Measuring Specific Resistivity and Hall Effect of Discs of Arbitrary Shape, *Philips Res. Rep. Vol. 13, No. 1(1958)1*

[36] **D. Pitzl et al.:** Evaluation of Double Sided, AC-Coupled, Double Metal Silicon Strip Detectors for H1 at HERA, *Nucl. Instr. Meth. in Phys. Res. A 348(1994)454*

[37] **H. Spieler:** Lectures on Detector Techniques, Semiconductor Detectors, *Lawrence Berkely National Laboratory, USA, http://www-physics.lbl.gov/~spieler*

[38] **Spice:** A general purpose circuit simulation program, *distributed (among others) by Berkeley University http://www-cad.eecs.berkeley.edu*

[39] **M. Glaser:** private communication *(CERN, Switzerland)*

[40] **Schweizerische Strahlenschutzverordnung:** Anhang 3: Daten für den operationellen Strahlenschutz, *SR 814.501, available at http://www.admin.ch*

[41] **M. Huhtinen, P. A. Aarino:** Estimation of Pion Induced Displacement Damage in Silicon, *Nucl. Instr. Meth. in Phys. Res. A 335(1993)580*

[42] **Fluka:** A Fully Integrated Particle Physics Simulation Package, *available at: http://fluka.web.cern.ch/fluka*

[43] **K. F. Galloway et al.:** A Simple Model for Separating Interface and Oxide Charge Effects in MOS Device Charactersitcs, *IEEE Trans. Nucl. Sci. Vol. NS31, No. 6, 1984, p. 1497*

[44] **A. Roy:** private communication, *(Purdue University, Indiana, USA)*

[45] **A. S. Grove, D. J. Fitzgerald:** Surface Effects on p-n Junctions: Characteristics of Surface Space Charge Regions Under Non-Equilibrium Conditions, *Solid State Elec. 9(1966)783*

[46] **O. Leistiko, A. S. Grove:** Breakdown Voltage of Planar Silicon Junctions, *Solid State Elec. 9(1966)847*

[47] **E. H. Nicollian, J. R. Brews:** MOS (Metal Oxide Semiconductor) Physics and Technology, *John Wiley & Sons, New York, 1982*[1]

[48] **K. W. Böer:** Survey of Semiconductor Physics, *Van Nostrand Reinhold, New York, 1990*[1]

[49] **M. Lechner:** Development of a Radiation Hard Pixel Analogue Block for the CMS Vertex Detector, *PhD Thesis, Eidgenössische Technische Hochschule, Zürich, Switzerland, 1998; Diss ETH No. 12866*

[50] **I. Ropotar:** An investigation of Silicon Pixel Tracking Detectors and their Applications in a Prototype Vertex Telescope in the CERN NA50 Heavy Ion Experiment, *PhD Thesis, Bergische Universität Gesamthochschule Wuppertal, Germany, 2000, WUB-DISS 99-20*

[51] **S. Kavadias et al.:** Calculation of Pixel Detector Capacitances through Three Dimensional Numerical Solutions of the Laplace Equation, *IEEE Trans. Nucl. Sci. 41(1994)397*

[52] **A. Cerdeira, M. Estrada:** Analytical Expression for the Calculation of Pixel Detector Capacitances, *IEEE Trans. Nucl. Sci. 44(1997)63*

[53] **C. Amsler et al.:** A High Resolution Silicon Beam Telescope, *Nucl. Instr. Meth. in Phys. Res. A(in print).*

[54] **V. Dubacher:** Test of a Silicon Pixel Detector with 50 GeV/c pions, *Diploma Thesis, Physik-Institut der Universität Zürich, Switzerland, 1996*

[55] **R. Kaufmann, B. Henrich:** Lorentz-Angle in Irradiated Silicon, *Nucl. Instr. Meth. in Phys. Res. A(in print)*

[56] **M. Glättli:** Untersuchung von Silizium-Pixeldetektoren mit einem Silizium-Mikrostreifen Strahlteleskop, *Diploma Thesis, Physik-Institut der Universität Zürich, Switzerland, 1998*

[57] **M. Pernicka et al.:** A VME-Based Read-Out System for the PSI30 Chip, *Institut für Hochenergiephysik der Östereichischen Akademie der Wissenschaften, Vienna, Austria, 1999*

[58] **W. C. Dash, R. Newman:** Intrinsic Optical Absorption in Single-Crystal Germanium and Silicon at 77 K and 300 K, *Phys. Rev. 99(1955)1151*

[59] **Landolt-Börnstein:** Numerical Data and Functional Relationships in Science and Technology, *Group III Vol. 17a, Springer, Berlin, 1982*

[60] **D. M. Caughey et al.:** Carrier Mobilities in Silicon Empirically Related to Doping and Field, *Proc. IEEE 55(1967)2192*

[61] **M. Kriechbaum et al.:** Hall Effect of Hot Electrons in Silicon, *J. Phys. Chem. Solids, 33(1972)829*

[62] **B. Henrich et al.:** Depth Profile of Signal Charge Collected in Heavily Irradiated Silicon Pixels, *CMS-NOTE/1997-021*

[63] **R. Horisberger, D. Pitzl:** A Novel Read-Out Chip For Silicon Strip Detectors with Analogue Pipeline and Digitally Controlled Analogue Signal Processing, *Nucl. Instr. Meth. in Phys. Res. A 326(1993)92*

[64] **R. Kaufmann, B. Henrich:** Charge Drift in Silicon, *CMS Pixel Internal Note 1998/3, available at http://cms.web.psi.ch/cms.html*

[65] **W. Paul (Ed.):** Handbook on Semiconductors, Volume 1, Band Theory and Transport Properties, *North-Holland, Amsterdam, 1982*[1]

- ➢ L. M. Roth: Dynamics of Electrons in Semiconductors in Electric and Magnetic Fields
- ➢ E. Conwell: Transport: The Boltzmann Equation
- ➢ A. C. Smith: Transport Using the Particle Kinetic Model
- ➢ D. K. Ferry: Fundamental Aspects of Hot Electron Phenomena

[66] **A. Castoldi et al.:** Performance of Silicon Drift Detectors in a Magnetic Field, *Nucl. Instr. Meth. in Phys. Res. A 399(1997)227*

[67] **R. E. Robson et al.:** Electron Transport Theory in Gases: Must it be so Difficult?, *Nucl. Instr. Meth. in Phys. Res. A 394(1997)74*

[68] **M. Levinshtein et al. (Ed.):** Handbook Series on Semiconductor Parameters, Volume 1, *World Scientific, Singapore, 1996*[1]

[69] **C. Canali et al.:** Electron Drift Velocity in Silicon, *Phys. Rev. B 12(1974)2265*
G. Ottaviani et al.: Hole Drift Velocity in Silicon, *Phys. Rev. B 12(1974)3317*

[70] **G. Dresselhaus et. al:** Cyclotron Resonance of Electrons and Holes in Silicon and Germanium Crystals, *Phys. Rev. 98(1955)368*

[71] **B. E. Deal:** Standardised Terminology for Oxide Charges Associated with Thermally Oxidised Silicon, *IEEE Trans. Elec. Dev. ED-27(1980)606*

ACKNOWLEDGEMENTS

Throughout the four years of my PhD time I met many people to whom I am very grateful for their help, encouragement and sympathy. I enjoyed many interesting and cheerful hours with them.

First of all I would like to thank Claude Amsler for giving me the opportunity to make a PhD in the CMS pixel collaboration. I am also very grateful to Roland Horisberger who introduced me to the art of silicon sensors. I very much appreciated the instructive discussions we had.

In addition, I am very indebted to Henk Pruys whose sound arguments helped me to clarify many questions. I also thank him for his help during the beam-tests and for carefully reading the manuscript.

Moreover, I am very obliged to Maurice Glaser for his kind help during the irradiations at CERN.

A special thank-you goes to the whole CMS pixel crew at PSI: To Beat Henrich (for the good time we had at PSI and at CERN), to Kurt Gabathuler (the calm and steady rock in the busy waters of our experiment), to Silvan Streuli and Jan Rothe (who knew a solution to all my mechanical problems), to Marlon Barbero and Danek Kotlinski (who shared the demanding time of a beam test with me), to Beat Meier and Raphael Baldinger (who always had an answer to my electronics questions) and of course to all those who shared their successes with us at the famous PSI champagne-celebrations.

I also like to express my appreciation to the University of Zürich group at CERN, namely to Petra Riedler (for her cordiality, the interesting scientific conversations and for carefully reading a part of this manuscript) and to Christian Regenfus, Michel Glättli and Stefan Spanier (for their help during the beam-tests), but of course also to the rest of the group for the pleasant hours I had when I was at CERN.

Last, but not least, I thank all my friends and my parents for their great support and empathy. Not forgotten are also all the people at the University of Zurich and at PSI who contributed to the friendly atmosphere which made it a pleasure to work there.

This thesis was supported by the Swiss National Science Foundation.

CURRICULUM VITAE

Rolf Anton Kaufmann
Born 8. January 1970 in Lucerne
Citizen of Knutwil, Switzerland

Education

1977 - 1983	Primary school Knutwil
1983 - 1990	Gymnasium Kantonsschule Sursee
1991 - 1997	University of Zürich, studies of physics (principal subject), mathematics and political science (subsidiary subjects)
1996 - 1997	Diploma work at the European Organisation for Nuclear Research (CERN) in Geneva
1997 - 2001	Scientific assistant and PhD student at the University of Zürich and at the Paul Scherrer Institut in Villigen

Qualifications

1990	Matura typus C (A-levels)
1997	Diploma in physics (master degree)